

UNIVERSITY of CALIFORNIA
Santa Barbara

**Growth and Electronic Structure of Heusler Compounds for Use in
Electron Spin Based Devices**

A Dissertation submitted in partial satisfaction of the
requirements for the degree

Doctor of Philosophy

in

Materials

by

Sahil Jaykumar Patel

Committee in charge:

Professor Christopher Palmstrøm, Chair

Professor Arthur Gossard

Professor Ram Seshadri

Professor James Allen

June 2015

The dissertation of Sahil Jaykumar Patel is approved.

Arthur Gossard

Ram Seshadri

James Allen

Christopher Palmstrøm, Chair

May 2015

Growth and Electronic Structure of Heusler Compounds for Use in Electron
Spin Based Devices

Copyright © 2015

by

Sahil Jaykumar Patel

Acknowledgements

There are many who have contributed to the research presented in this thesis, and unfortunately, I cannot acknowledge all of them. To the people I have not mentioned, but have contributed greatly to this work: thank you. From that group there are a number of people who have had a significant impact on the work and the five years I have spent at UC-Santa Barbara:

First, I would like to thank my committee, Art Gossard, Ram Seshadri, Jim Allen, and Chris Palmstrøm, for all of the helpful advice and ideas you have come up with that have helped me to complete experiments and formulate new ones. In particular, I thank my advisor, Chris, for deciding to fund me, and providing an infinite amount of ideas for me to filter through and decide what to do next.

Over the last few years the Palmstrøm research group has unfortunately had to deal excessively with the wrath of the UHV gods, and without the rest of the group's support I would not complete this dissertation. In particular, I have gained a lot of experience both scientifically and mechanically through work with Bo, Jason, Anthony, and Nate. Other members of the group have suffered through my gripes, and I'm thankful that they can put up with it and have provided such great company: Jay, Sean, Mihir, Tony, Dan, Tobias, Alan, Big Tony, Ken, Trevor, Qi, Luca, Linda, Ryan, Mitchell, Alex, Rachel, and Anisa. I also want to thank the previous lab members and postdocs who spent

MANY hours, day and night, in setting up the lab at UCSB and starting research projects here, including Qi, Alex K., Jörg, Ludwig, and Shinobu.

Much of the work in this thesis has been accomplished through tremendous collaborations with Paul Crowell's group at University of Minnesota (Chad, Kevin, Lee, Tim, Gordon, Changjiang) as well as Anders Mikkelsen's group at Lund University (Martin and Rainer) and beamline staff at MAX-lab in Lund (Balu, Craig, and Johan). I am very grateful for the fruitful collaborations we have had.

Keeping sane while at work is important, and there are a number of people in the MBE lab who I enjoyed working with outside of our group who have made my stay at UCSB quite enjoyable. Also John English has been quite fun to work with, both in the lab, and in his office, or over a beer (or two).

I'd like to thank Brian Schultz, who luckily took me under his wing to teach me the inner workings of MBE chambers and STMs, as well as all sorts of tricks and methods to deal with plumbing, electronics, mechanical designs, MBE growth, surface science, and millions of other things. Without Brian in our group, I am sure I would not have completed this dissertation.

Outside of work, there are quite a large number of people who I've had close friendships with over the past five years, and when work wasn't going well, these were the people who kept me sane and let me think about something else for a change, like teaching me how to ski: Jason S., Evelyn, Alex S., Erin, Bo, Jack,

Nate, Anne, Titus, Alex H. the list continues forever. I've had a great time at UCSB.

Finally I'd like to thank my family for all of their support including my soon to be wife, Stephanie, and my goofy dog who sat by my side and whined at me through every page of writing, Ella.

Curriculum Vitæ

Sahil Jaykumar Patel

EDUCATION

Doctor of Philosophy in Materials Science, 2015
University of California, Santa Barbara
Advisor: Christopher J. Palmstrøm

Bachelor of Science in Materials Science and Engineering, 2008
Cornell University, School of Engineering
Minor in Mechanical Engineering

WORK EXPERIENCE

Graduate Student Researcher
University of California, Santa Barbara (UCSB), 2010- 2015
Advisor: Professor Christopher J. Palmstrøm

Engineering Intern
Porous Materials, Inc.

AWARDS

Best Student Oral Presentation
International Conference on Molecular Beam Epitaxy (ICMBE)
Spin transport in $\text{Co}_2\text{MnSi}/\text{GaAs}$ (001) heterostructures: the role of nucleation on interface formation

TEACHING EXPERIENCE

Graduate student mentor for Tyler Rhodes and Thomas Neulinger through the Center for Energy Efficient Materials Internship Program, 2012-2013

Teaching assistant for Semiconductor Device Processing (Matrl/ECE 215A/220A) with Professor Christopher J. Palmstrøm at University of California, Fall 2011

PUBLICATIONS

“Surface and electronic structure of PtLuSb (001) thin films” **Sahil Patel**,

J. Kawasaki, J. Logan, B. Schultz, J. Adell, B. Thiagarajan, A. Mikkelsen, and C. Palmstrøm. *Applied Physics Letters* **104**, 201603 (2014).

“Electrical detection of ferromagnetic resonance in ferromagnet/n-GaAs heterostructures by tunneling anisotropic magnetoresistance” C. Liu, Y. Boyko, C. Geppert, K. Christie, G. Stecklein, **Sahil Patel**, C. Palmstrøm, and P. Crowell. *Applied Physics Letters* **105**, 212401 (2014).

“Knight shift and hyperfine leakage factor in Fe/n-GaAs heterostructures” K. Christie, C. Geppert, **Sahil Patel**, C. Palmstrøm, and P. Crowell. *Physical Review B Under Review* (2014).

“Electromotive Force Generated by Spin Accumulation in FM/n-GaAs Heterostructures” C. Geppert, L. Wienkes, K. Christie, **Sahil Patel**, C. Palmstrøm, and P. Crowell. *Physical Review Letters Under Review* (2014).

“Manipulating Spin Injection in Heusler/GaAs (001) heterostructures” **Sahil Patel**, C. Geppert, K. Christie, G. Stecklein, T. Peterson, A. Rath, F. Shi, C. Sivakumar, P. Voyles, B. Butler, P. Crowell, and C. Palmstrøm. *In preparation*.

“Electronic structure of PtLuBi (001) thin films” **Sahil Patel**, B. Schultz, A. Janotti, C. Palmstrøm. *In preparation*.

“Epitaxial PtLuSb (001) Thin Films: Surface Reconstructions and Transport” **Sahil Patel**, J. Logan, S. Harrington, B. Schultz, C. Palmstrøm. *In preparation*.

Abstract

Growth and Electronic Structure of Heusler Compounds for Use in Electron Spin Based Devices

by

Sahil Jaykumar Patel

Spintronic devices, where information is carried by the quantum spin state of the electron instead of purely its charge, have gained considerable interest for their use in future computing technologies. For optimal performance, a pure spin current, where all electrons have aligned spins, must be generated and transmitted across many interfaces and through many types of materials. While conventional spin sources have historically been elemental ferromagnets, like Fe or Co, these materials produce only partially spin polarized currents. To increase the spin polarization of the current, materials like half-metallic ferromagnets, where there is a gap in the minority spin density of states around the Fermi level, or topological insulators, where the current transport is dominated by spin-locked surface states, show promise. A class of materials called Heusler compounds, with electronic structures that range from normal metals, to half-metallic ferromagnets, semiconductors, superconductors and even topological

insulators, interfaces well with existing device technologies, and through the use of molecular beam epitaxy (MBE) high quality heterostructures and films can be grown. This dissertation examines the electronic structure of surfaces and interfaces of both topological insulator (PtLuSb- and PtLuBi-) and half-metallic ferromagnet (Co₂MnSi- and Co₂FeSi-) III-V semiconductor heterostructures.

PtLuSb and PtLuBi growth by MBE was demonstrated on Al_xIn_{1-x}Sb (001) ternaries. PtLuSb (001) surfaces were observed to reconstruct with either (1x3) or c(2x2) unit cells depending on Sb overpressure and substrate temperature. The electronic structure of these films was studied by scanning tunneling microscopy/spectroscopy (STM/STS) and photoemission spectroscopy. STS measurements as well as angle resolved photoemission spectroscopy (ARPES) suggest that PtLuSb has a zero-gap or semimetallic band structure. Additionally, the observation of linearly dispersing surface states, with an approximate crossing point 240meV above the Fermi level, suggests that PtLuSb (001) films are topologically non-trivial. PtLuBi films also display a Fermi level position approximately 500meV below the valence band maximum.

Co₂MnSi and Co₂FeSi were also grown by MBE on GaAs (001) for use as spin injectors into GaAs lateral spin valve devices. By the growth of the quaternary alloy Co₂Fe_xMn_{1-x}Si and varying x , electron doping of the full Heusler compound was demonstrated by observation of a crossover from a majority spin polarization of Co₂MnSi to a minority spin polarization in Co₂FeSi. Co₂MnSi

films were studied as a function of the nucleation sequence, using either Co- or MnSi- initiated films on c(4x4) GaAs. Studies using x-ray photoemission spectroscopy (XPS), STM/STS, and transmission electron microscopy (TEM) suggest that the bulk of the Co₂MnSi films and the interfacial structure between Co₂MnSi and GaAs is not modified by the nucleation sequence, but a change in spin transport characteristics suggests a modification of semiconductor band structure at the Co₂MnSi/GaAs interface due to diffusion of Mn leading to compensation of the Schottky barrier contact. Diffusion of Mn into the GaAs was confirmed by secondary ion mass spectrometry (SIMS) measurements. The proposed mechanism for the modified spin transport characteristics for MnSi initiated films is that additional diffusion of Mn into the GaAs, widens the Schottky barrier contact region. These studies suggest that the ideal initiation sequence for Co₂MnSi/GaAs (001) lateral spin valve devices is achieved by deposition of Co first.

Contents

Contents	xii
1 Heusler Compounds for Spintronic Devices	1
1.1 Introduction	1
1.2 Heusler Compounds	2
1.2.1 Electronic structure of Heusler compounds	6
1.3 Topological Insulators	7
1.3.1 Half-Heusler topological insulators	10
1.4 Spintronics	13
1.4.1 Spin Source	14
1.4.2 Role of the interface on spintronic devices	16
1.4.3 Semiconductor spintronics: the role of band structure near the spin injection contact	17
2 Heusler Heterostructure Growth and Characterization Tech- niques	19
2.1 Molecular Beam Epitaxy	19
2.2 More specifics on Heusler growth: flux control and calibration	22
2.3 <i>In-situ</i> growth and surface characterization setup	27
2.4 Scanning tunneling microscopy and scanning tunneling spectroscopy (STM/STS)	29
2.5 Photoemission spectroscopy	32
2.5.1 ARPES measurement instrumentation	35

2.6	Measurements of spin injection in lateral spin valve heterostructures	37
2.6.1	Biased detector non-local spin valve measurements	43
2.6.2	Determining the sign of spin accumulations in Co ₂ MnSi/GaAs (001) lateral spin valve devices	46
3	Half-Heusler topological insulators: PtLuSb (001) and PtLuBi (001) thin films	48
3.1	PtLuSb Growth and Electronic Structure	50
3.1.1	Sb capping and decapping	54
3.1.2	Surface reconstructions of PtLuSb (001)	57
3.2	Electronic Structure of PtLuSb (001) thin films	62
3.2.1	Measurement of the electronic quality of PtLuSb (001) films	62
3.2.2	Improving the electronic quality of PtLuSb (001) films . .	64
3.2.3	Temperature dependent Hall measurements of PtLuSb (001)	67
3.2.4	Scanning tunneling spectroscopy (STS) and ultra-violet photoemission spectroscopy (UPS) of PtLuSb (001)	69
3.2.5	Angle resolved photoemission spectroscopy (ARPES) of PtLuSb (001) surfaces	72
3.2.6	Normal Emission	73
3.2.7	k_{\parallel} dispersions as a function of incident photon energy . . .	74
3.2.8	spin-ARPES of linearly dispersing surface states	79
3.2.9	Summary	80
3.3	PtLuBi (001) Thin Films	82
3.3.1	STM PtLuBi (001) surfaces	84
3.3.2	Summary	91
3.4	Outlook for topological half-Heusler thin films	92
4	Full-Heusler/GaAs Heterostructures for Spin Injection	94
4.1	Introduction	94
4.2	Growth of full Heusler compound Co ₂ MnSi and Co ₂ FeSi thin films by molecular beam epitaxy (MBE)	96

4.2.1	Growth of Heusler/GaAs (001) layers for lateral spin valve heterostructures	103
4.3	Co ₂ Fe _x Mn _{1-x} Si alloys: Controlling the bulk spin polarization . . .	108
4.3.1	Growth of Co ₂ Fe _x Mn _{1-x} Si alloys	110
4.3.2	Biased detector spin signal measurements of Co ₂ Fe _x Mn _{1-x} Si/GaAs (001) spin valves	110
4.4	Understanding the effect of the Co ₂ MnSi/GaAs (001) interface on spin injection	115
4.4.1	Co- and MnSi- Initiated Co ₂ MnSi/GaAs (001) Lateral Spin Valve Heterostructures	115
4.4.2	Spin signals of Co- and MnSi- initiated Co ₂ MnSi/GaAs (001) non-local spin valves	119
4.4.3	<i>In-situ</i> STM and STS of Co ₂ MnSi growth on c(4x4) GaAs (001) surfaces	120
4.4.4	<i>In-situ</i> XPS measurements of core-level emission intensity during Co ₂ MnSi nucleation on c(4x4) GaAs (001) surfaces	132
4.4.5	Investigation of the Co ₂ MnSi/GaAs (001) interface by HAADF-STEM imaging	137
4.5	Effects of Co ₂ MnSi growth conditions on the GaAs band structure near the interface	139
4.5.1	I-V measurements of Co ₂ MnSi/GaAs Schottky contacts . .	142
4.5.2	Effect of modification of band structure on spin injection properties	144
4.6	Outlook for Heusler compound spin injectors into III-V materials	146
5	Outlook of Heusler compounds for future research	148
A	<i>In-situ</i> Point-contact Andreev reflection spectroscopy (PCAR)	152
A.1	Measurements of spin-polarization in ferromagnets: PCAR	152
A.2	Traditional PCAR measurements and the advantages of <i>in-situ</i> growth and measurement	156
A.3	PCAR measurements: Measurement design and results	157

Chapter 1

Heusler Compounds for Spintronic Devices

1.1 Introduction

Traditional computing architectures have been built upon complementary metal-oxide semiconductor (CMOS) architectures which use simple on and off devices for computation. However, to increase computing power, more of these on/off devices, or transistors, need to be packed onto ever shrinking areas, and at some point a size limit will be reached where these transistors no longer work due to quantum mechanical effects. Additionally, as the transistor shrinks, its leakage current increases, increasing the overall power consumption of the device. To move past these obstacles, new computation technologies must be researched. A promising new field that may realize a new type of computation is the field

of spintronics. Spintronic devices utilize the fundamental, quantum mechanical quantity of electron spin to store, read, and transmit data. New materials must be developed which have ability to store, create, and transmit spin based data. To create devices, these materials must be integrated into heterostructures, and the properties of these heterostructures must be characterized. A class of materials called Heusler compounds has a strong potential for use in spintronic devices, as they can be integrated into heterostructures with many other electronic materials, and have the ability to store, create, and transmit data through electron spins.

1.2 Heusler Compounds

Heusler compounds are a class of ternary intermetallics that crystalize in two major crystal structures: $L2_1$ Full Heuslers with the chemical formula X_2YZ and $C1_b$ Half-Heuslers with the chemical formula XYZ . The full- and half-Heusler crystal structures are shown in 1.1. These compounds can be thought of as 4 interpenetrating face-centered cubic lattices with the element Z at Wyckoff position 4a (0,0,0), element Y at Wyckoff position 4b ($\frac{1}{2},0,0$). In full Heusler compounds, both Wyckoff positions 4c ($\frac{1}{4},\frac{1}{4},\frac{1}{4}$) and 4d ($\frac{3}{4},\frac{1}{4},\frac{1}{4}$) are occupied by element X, while in half Heusler compounds, the Wyckoff position 4c is occupied, and the position 4d remains unoccupied. The resulting crystal structures are similar for full and half-Heuslers, but an important consequence of the empty

4d position in half Heuslers is a loss of symmetry. This makes half-Heusler compounds have 2-fold symmetric surfaces, while full Heuslers have 4-fold symmetric surface, as will be further discussed in this dissertation.

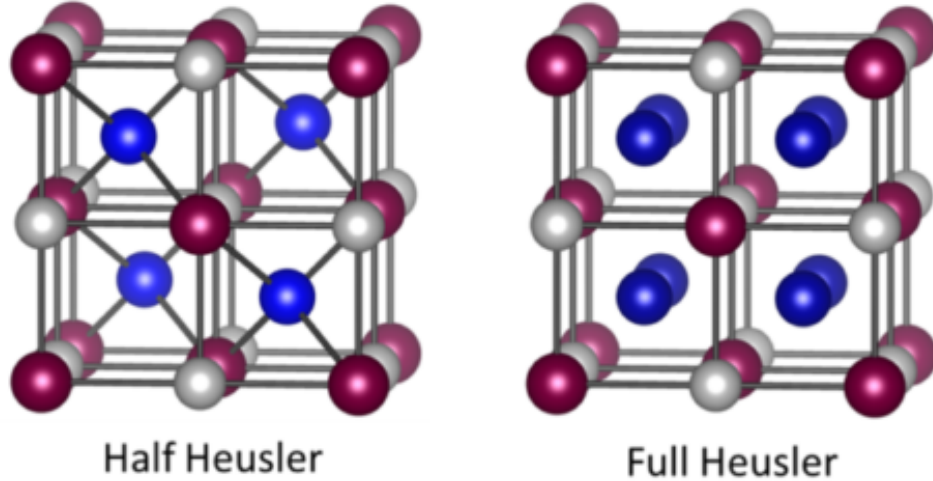


Figure 1.1. Crystal structure of Heusler compounds. Both the half- (left) and the full- (right) Heusler crystal structures are shown. The half-Heusler structure can be thought of as 3 interpenetrating FCC sublattices, while the full Heusler has 4 interpenetrating FCC sublattices.

The cubic Heusler crystal structure, consisting of interpenetrating FCC lattices, is very similar to the zinc-blende and diamond crystal structures of III-V and elemental semiconductors, respectively. Additionally, as shown in figure 1.2 Heuslers have similar lattice parameters to the III-V compounds semiconductors. Both a good lattice match, as well as a continuous FCC sublattice from III-V semiconductors into Heusler compounds, promotes epitaxial growth as well as the formation of atomically abrupt interfaces, allowing for the growth of complex Heusler/III-V thin film heterostructures and subsequent fabrication of devices that utilize Heusler/III-V structures.

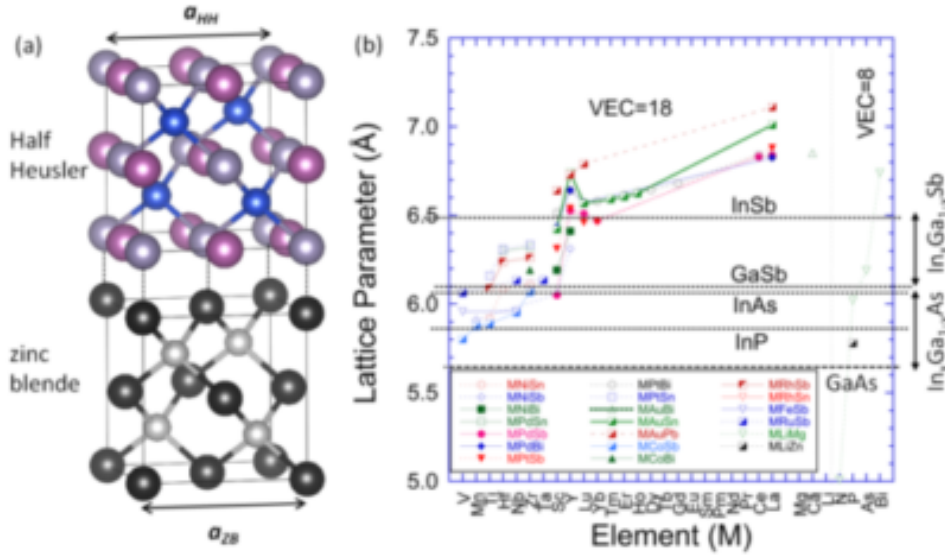


Figure 1.2. The lattice parameter of select Heusler compounds plotted against the lattice parameter of common III-V semiconductors, demonstrating their good lattice match and potential for incorporation into III-V devices [1]

This class of materials contains over 1000 compounds, with a wide range of electronic properties including ferromagnets, half-metallic ferromagnets, semiconductors, superconductors, and topological insulators. The ability to tune electronic structure while retaining the same basic crystal structure and lattice constant, makes Heusler compounds analogous to complex perovskite oxides. In thin film form, this gives Heusler compounds the ability to be grown into complex heterostructures for a variety of interesting devices. Figure 1.3 shows the vast number of elements that can be incorporated into the Heusler crystal structure.

Traditionally, research in the field of Heuslers has focused on full-Heuslers for their interesting magnetic properties [3, 4], but more recently, research has

X₂YZ Heusler compounds

H 2.20																	He	
Li 0.98	Be 1.57											B 2.04	C 2.55	N 3.04	O 3.44	F 3.98	Ne	
Na 0.93	Mg 1.31											Al 1.61	Si 1.90	P 2.19	S 2.58	Cl 3.16	Ar	
K 0.82	Ca 1.00	Sc 1.36	Ti 1.54	V 1.63	Cr 1.66	Mn 1.55	Fe 1.83	Co 1.88	Ni 1.91	Cu 1.90	Zn 1.65	Ga 1.81	Ge 2.01	As 2.18	Se 2.55	Br 2.96	Kr 3.00	
Rb 0.82	Sr 0.95	Y 1.22	Zr 1.33	Nb 1.60	Mo 2.16	Tc 1.90	Ru 2.20	Rh 2.28	Pd 2.20	Ag 1.93	Cd 1.69	In 1.78	Sn 1.96	Sb 2.05	Te 2.10	I 2.66	Xe 2.60	
Cs 0.79	Ba 0.89	Hf 1.30	Ta 1.50	W 1.70	Re 1.90	Os 2.20	Ir 2.20	Pt 2.20	Au 2.40	Hg 1.90	Tl 1.80	Pb 1.80	Bi 1.90	Po 2.00	At 2.20	Rn		
Fr 0.70	Ra 0.90																	
		La 1.10	Ce 1.12	Pr 1.13	Nd 1.14	Pm 1.13	Sm 1.17	Eu 1.20	Gd 1.20	Tb 1.10	Dy 1.22	Ho 1.23	Er 1.24	Tm 1.25	Yb 1.10	Lu 1.27		
		Ac 1.10	Th 1.30	Pa 1.50	U 1.70	Np 1.30	Pu 1.28	Am 1.13	Cm 1.28	Bk 1.30	Cf 1.30	Es 1.30	Fm 1.30	Md 1.30	No 1.30	Lr 1.30		

Figure 1.3. Periodic table depicting the vast number of elements that can be incorporated into Heusler compounds to tune electronic properties, all while retaining the same cubic crystal structure. Red elements can sit in the X site, purple elements sit on the Y site, and green elements sit on the Z site [2].

picked up in the field of semiconductors [5], topological insulators [6–8], and superconductors [9–11]. Semiconducting Heusler compounds have recently gained interest for their use as potential thermoelectric materials [5, 12–14].

These compounds are mostly variants on semiconducting Heusler compounds, with doping to increase carrier concentration and to reduce lattice thermal conductivity. Even more recently, the prediction of topological insulators, and even topological superconductors has sparked a new interest in the synthesis of half-Heusler compounds with large average atomic number (Z), and large spin-orbit coupling [6–8].

1.2.1 Electronic structure of Heusler compounds

Figure 1.4 shows possible electronic structures that Heusler compounds can possess.

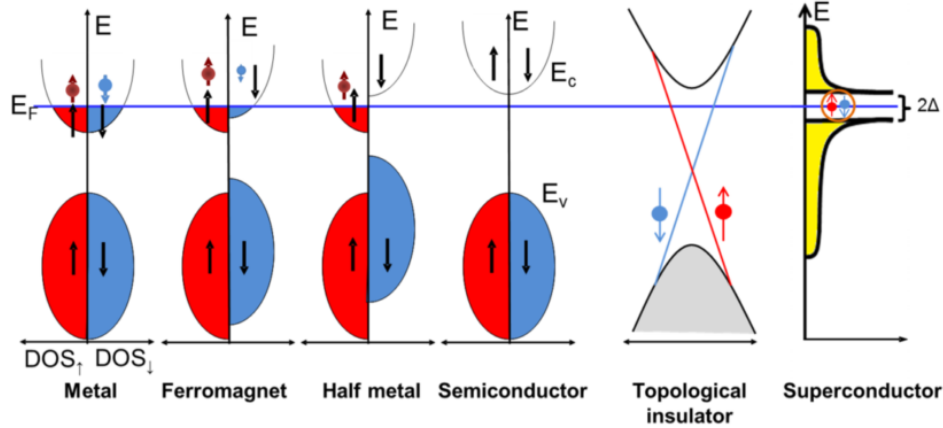


Figure 1.4. Possible electronic structures of Heusler compounds. By tuning the number of valence electrons per formula unit, the Fermi level position may be adjusted and the electronic structure of the resulting compound can be tuned.

The electronic properties of Heusler compounds can be fairly reliably predicted by counting the total number of valence electrons per formula unit [2]. Due to d-orbital crystal field splitting, which is based on the crystal structure and d-orbital overlap of neighboring atoms, Heusler compounds tend to have gaps in their band structures [2, 15]. For half-Heusler compounds, a valence electron count of 18 e- results in a compound with filled electronic states below this gap, and empty states above the gap, therefore leading to a semiconducting crystal. For full Heusler compounds, a filling of 24 valence electrons creates a similar semiconducting electronic structure, although in full Heusler compounds, these gaps tend to be much smaller. For both crystal structures, a valence electron

count above or below these numbers results in metallic electronic structures. In full Heusler compounds, these metallic structures have a tendency to become ferromagnetic [2]. Additionally, ferromagnetism can be stable with the d-orbital gap present in the minority spin channel, leading to half-metallic ferromagnetism and the potential for a 100% spin polarized source for spintronic devices.

1.3 Topological Insulators

Electronic materials can be divided into two simple groups: insulators and metals. In a simple picture, insulating materials are characterized by large band gaps and cannot transport electrons or holes, while metals have no band gaps, and can conduct electrons and holes easily. The term topological insulator bridges the gap between an insulator and a metal: the bulk of the material is insulating, and cannot pass current, while all surfaces of the material remain conductive and can pass current. In a topological insulator, not only are the surfaces conductive, but in these surface states, the momentum and spin are locked. This means that the spin of electrons traveling in these surface states is locked to the direction that they travel. The ultimate consequence of spin locking, is that current traveling across a topologically insulating surface is 100% spin polarized, with the potential for use in novel spintronic devices.

The E vs k dispersion of these states is linear with a helical spin texture [16]. A consequence of spin orbit coupling, the helical spin texture surface state pos-

esses time reversal symmetry, that is, if the electron momentum is reversed, it must be accompanied by a reversal in spin. These states are said to be topologically protected, and robust against disorder, as they are caused by a crossing of bulk bands at the interface between the bulk material and vacuum [16]. An example of this surface state is shown in figure 1.5 in the predicted band structure of the topological insulator Bi_2Se_3 as projected into the surface Brillouin zone. The band structure is calculated with and without the influence of spin orbit coupling. The incorporation of spin orbit coupling into the calculations results in the formation of a Dirac cone, or topologically protected state, in red [17]. This state has been experimentally verified in Bi_2Se_3 as well as many other 3D topological insulators using angle resolved photoemission spectroscopy (ARPES) which will be further discussed in section 2.5.

While current passed across the surface a topological insulator should theoretically come out 100% spin polarized, there are many experimental challenges that need to be addressed to synthesize these materials. More specifically, even if the electronic band structure theoretically predicts a bulk bandgap around the Fermi level, crystal defects can lead to a change in gap size or change in Fermi level position, leading to bulk conduction. Since the bulk bandstructure is not spin polarized, this leads to the reduction of the spin polarization of the total current.

The first demonstration of a topological state in a three-dimensional topo-

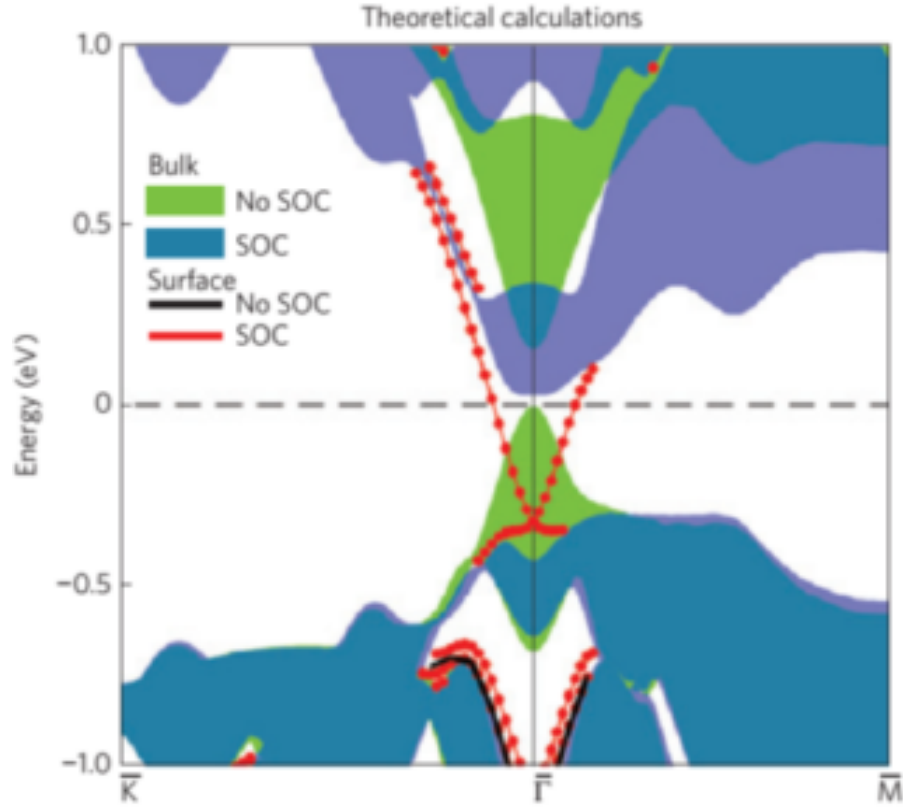


Figure 1.5. Bandstructure of Bi_2Se_3 projected onto the surface Brillouin zone. The simple bandstructure is shown calculated with (purple) and without (blue-green) spin-orbit coupling. The inclusion of spin orbit coupling leads to the topological bulk band inversion leading to the formation of a helical Dirac cone, shown in red [17].

logical insulator was in $\text{Bi}_{0.9}\text{Sb}_{0.1}$ [18]. While the topological state was verified by ARPES, the Fermi level was not located in a bulk band gap and therefore topological state could not be measured. Since then, other materials possessing topological surface states have been discovered and heavily studied. [16]. Even with these gapped electronic structures, though, it has been difficult to synthesize materials with the Fermi level within the bulk bandgap.

1.3.1 Half-Heusler topological insulators

Half Heusler topological insulators were first predicted in 2010 at the same time by Chadov, Lin, and Al-Sawai in three separate papers [6–8]. The topological state was predicted to arise due to an inversion of bulk bands in strongly spin orbit coupled materials. This inversion occurs when bands with s-like character, which are normally situated in the conduction band in trivial insulators, above the gap, are pushed lower in energy than the four-fold degenerate p-like bands at the Γ point of the Brillouin zone. This inversion leads to a topologically non-trivial state at the surface of the material, as these bands are part of a continuum, and must revert back to the trivial s above p state in vacuum. Since the bands are inverted in the crystal, and not inverted outside of the crystal, they must cross at the surface, leading to the formation of the topological state.

In the case of half-Heusler compounds, it was found that a general trend of increasing strength of the band inversion, which is calculated by subtracting the energy of the p-like bands from the s-like bands, is observed with increasing average atomic number (Figure 1.6). This is a direct consequence of increasing of the spin-orbit coupling by increasing the charge of the positive nucleus [7].

An additional consequence, however, of the band inversion is the closing of the bulk band gap. Many of the predicted topological half-Heuslers are zero-gap or semi-metallic materials, making it difficult to remove bulk conduction paths. However, alternatives have been proposed to open up a bulk bandgap,

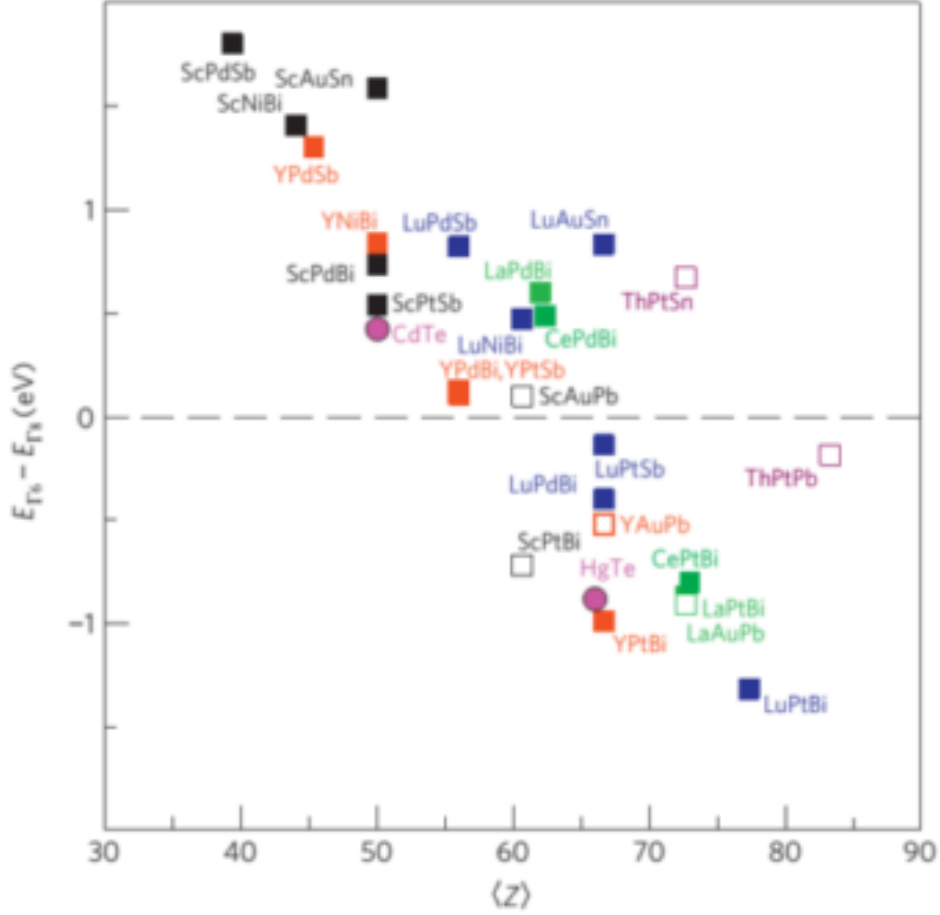


Figure 1.6. Calculated band inversion strength of half-Heusler compounds with a valence electron count of $18e^-$. A general trend of increasing band inversion strength (larger negative numbers) is observed for an increase of average atomic number Z . PtLuSb is on the border of this topologically trivial and non-trivial band inversion and PtLuBi displays the strongest band inversion [7].

particularly in zero-gap PtLuSb. Since the bulk band structure has conduction and valence bands that only touch, and do not overlap, the addition of tensile strain can open up a bulk bandgap [6, 7]. Since the application of tensile strain in three dimensions is not practical, one way to possibly strain the material is through thin film growth on lattice-mismatched substrates and apply biaxial tensile strain, which is also predicted to open a bulk bandgap while retaining

the topological band inversion, as illustrated in figure 1.7a. Also illustrated in figure 1.7b is the band structure calculation under 3% hydrostatic compressive strain. In this case, although a larger bandgap is opened, the topological band inversion is not preserved, resulting in a trivially insulating phase. Therefore, in designing thin film heterostructures to create a truly topologically insulating phase, only positive lattice mismatches can be considered, resulting in a tensile strain of the half-Heusler film.

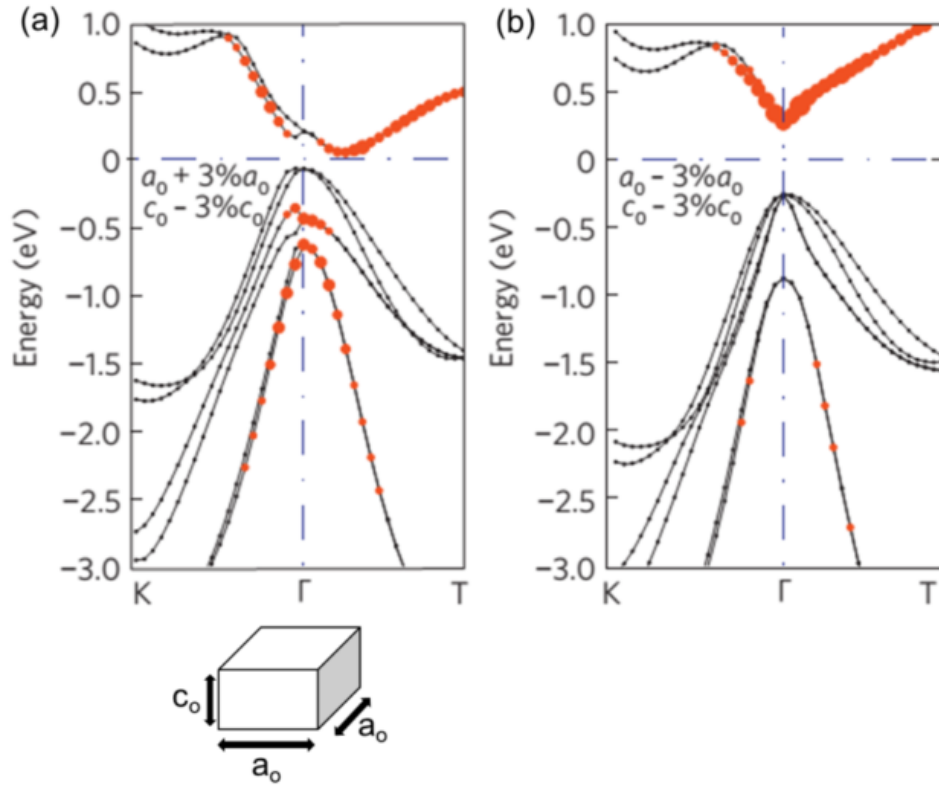


Figure 1.7. (a) PtLuSb band structure under application of 3% biaxial tensile strain opening a bulk bandgap and preserving the topological band inversion, as denoted by the presence of s-like states (orange dots) in the valence band. (b) PtLuSb band structure under application of 3% biaxial compressive strain opening a bulk bandgap and destroying the topological band inversion, as denoted by the absence of s-like states (orange dots) in the valence band. [6].

1.4 Spintronics

Spintronics is a very general term which refers to devices that use the fundamental quantum mechanical quantity of spin of electrons to operate. In general, spintronic devices can be split into two broad categories: metal based spintronics and semiconductor based spintronics. The category of metal based spintronics encompasses giant magnetoresistive (GMR) [19, 20], tunneling magnetoresistive devices (TMR) [21, 22], and other types of magnetoresistive (MR) devices, as well as metallic spin valves in either the lateral or vertical current transport direction and more recently, spin torque transfer memories (STTM). Semiconductor based spintronics attempt to modify the electron spin, or to convert it into another form, such as light. These devices include the proposed spin-FET, lateral spin valves using semiconductor transport channels, and spin-LEDs [23–25]. Regardless of the device structure or concept, all devices require a spin source, spin transport material, and spin detector. This dissertation will focus on semiconductor based spintronics, as work towards the realization of the Datta-Das spin-FET [23], but draws on concepts developed in the study of metal based spintronics that have been well studied and can be used to explain characteristics of semiconductor devices.

1.4.1 Spin Source

The most important aspect of spintronic device design is a spin source. The most reliable spin source has traditionally been a ferromagnet. Ferromagnetic materials are characterized by unpaired electrons that have a natural tendency to align spins. When placed in a magnetic field, these spins can align as an ensemble with that field, but when the field is removed, they retain that same spin direction, generating an internal magnetic field. When talking about ferromagnets, the terms majority and minority spins can be defined. In itinerant, or delocalized ferromagnets, the majority spin can be defined as the spin direction which has a larger number of filled states, while the minority spin has a smaller number of filled states. The net imbalance in spins results in a magnetization of the sample (Figure 1.8).

Taking a closer look at the details of the density of states for each spin, we can define the term spin polarization, which is related to imbalance in spin density of states at the Fermi level. Equation 1.1 shows the traditional definition of spin polarization, which is the net spin present at the Fermi level described as a percentage:

$$P = \frac{\rho_{\uparrow}(E_F) - \rho_{\downarrow}(E_F)}{\rho_{\uparrow}(E_F) + \rho_{\downarrow}(E_F)} \times 100 \quad (1.1)$$

The spin polarization at the Fermi level is of considerable importance in a spintronic device. In metals, current transport is dominated by electronic

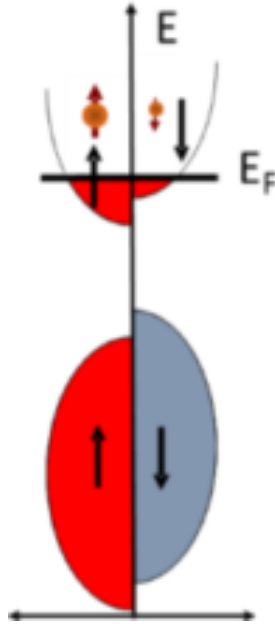


Figure 1.8. Cartoon schematic of the density of states of a ferromagnet. A net imbalance in majority (red) and minority (blue) spins is characteristic of a ferromagnet. At the Fermi level, denoted by E_F , there is also an imbalance in number of states. This imbalance leads to the net polarization of spins in a current flowing through a ferromagnetic material.

states at or near the Fermi level. Since the ferromagnetic density of states is spin polarized at the Fermi level, this means that the current flowing through and out of a ferromagnet becomes spin polarized, which allows it to serve as a source of spins. Ferromagnets with larger spin polarizations are, in general, of interest for researchers as they provide a source of current that has a larger spin polarization. Taken to the extreme, some materials have the potential to be 100% spin polarized, that is, they have no minority states at or near the Fermi level. These materials are called half-metallic ferromagnets. One promising way to measure the bulk spin polarization of a material is through a technique called point contact Andreev reflection (PCAR) spectroscopy where a superconducting

point contact is made to the material of interest, and spectroscopy within the superconducting gap can provide information about spin transport across the junction [26]. A more detailed discussion of this technique can be found in appendix A.

1.4.2 Role of the interface on spintronic devices

High bulk spin polarization, however, is not the only criteria for a good spin source. The interface between the spin source and the rest of the device is crucial, as the change in periodicity due to the interface causes the formation of interfacial states, which can have different band structure than the bulk, leading to either an enhancement or reduction in spin polarization of the flowing current. Interfacial states have been theorized to be the driving force in the reduction of spin polarization of the tunneling current in $\text{Co}_2\text{MnSi}/\text{MgO}/\text{Co}_2\text{MnSi}$ magnetic tunnel junctions [27]. This work suggests that a purely Mn-O interfacial bonding configuration at the $\text{Co}_2\text{MnSi}/\text{MgO}$ interface is the only interface that is stable and predicted to retain half-metallicity. This theoretical work has been substantiated by the observation of increasing tunneling magnetoresistance ratio (TMR) in tunnel junctions composed of $\text{Co}_{2-x}\text{Mn}_{1+x}\text{Si}$ electrodes, with x as large as 0.3 [28]. In these samples, the percentage of MnMn/O type interface increased with increasing x , presumably leading to an increase in half-metallicity at the interface, and an increase in spin polarization of the tunneling current

[29]. This theoretical work and experimental observation show the importance of the interface between the spin source and the spin channel material.

1.4.3 Semiconductor spintronics: the role of band structure near the spin injection contact

While the Datta-Das spin-FET transistor is regarded as the holy grail of semiconductor spintronics, the process of actually transporting the electron from the ferromagnet into the semiconductor has proven to be difficult [23]. Initially, researchers attempted to make ohmic contacts to semiconductors using ferromagnets, but these contacts failed to inject spins into the semiconductor. The reason for this difficulty was described in 2000 and is due to the impedance mismatch at the ferromagnet semiconductor interface [30, 31]. A simple description of this problem as it follows, and is adapted from the thesis of Xiaohua Lou [32]. When electrons or holes are traveling from a ferromagnet, which is a metal, into a semiconductor, which is much more resistive than a metal, the effective resistance of spin-flipping in the metal at the semiconductor interface must also be considered. In an ohmic contact, majority electrons reach the semiconductor interface, and the resistance to get into the semiconductor is much higher than the effective resistance of the spin-flip at the interface, which causes majority electrons to flip. This results in the flow of a net unpolarized current into the semiconductor, even though the transport in the bulk of the ferromagnet is spin

polarized [30, 31]. To overcome this obstacle, a tunneling type contact is required where the tunneling process is only dominated by the density of states of the ferromagnet and semiconductor, and is not affected by spin flips present in diffusive transport [31]. The Schottky barrier which naturally forms at a metal-GaAs interface, due to Fermi-level pinning [33, 34], is an ideal and simple tunnel barrier for spin injection into GaAs, and has been widely used in semiconductor spintronics [35–37]. Since the first demonstrations of spin injection to GaAs, a considerable amount of work has gone into engineering of the Schottky barrier to optimize spin injection efficiency and transport into semiconductor layers and heterostructures deep in the semiconductor. Although a Schottky barrier is naturally formed when GaAs is contacted by a metal, the details of its shape can vary greatly depending on the metal (or in this case, the ferromagnet) and the doping in the Schottky barrier region (due to the modification of the space-charge region charge density) [33, 34]. Luckily, the GaAs Schottky barrier is fairly robust, and the interfacial Fermi level pinning does not vary greatly between different ferromagnets, so techniques developed for Fe/GaAs spin injection can be used for a variety of different ferromagnets. The assumption of a near mid-gap Fermi level pinning was used for the growth of Heusler compounds on GaAs, and was verified by the observation of similar current voltage (IV) characteristics in Heusler devices as are observed in Fe/GaAs (001) devices. Those details will not be presented in this dissertation.

Chapter 2

Heusler Heterostructure Growth and Characterization Techniques

2.1 Molecular Beam Epitaxy

For devices to utilize either half-metallic ferromagnetic full Heuslers or predicted topologically insulating half Heuslers, they first must be heteroepitaxially grown in thin film form. While much of the research in Heusler compound thin films has centered around sputtering [38–41], many of the highest quality Heusler films have been grown by molecular beam epitaxy [1, 42–45]. MBE is also the best method for the growth of ultra-high purity semiconductor heterostructures, and its control over doping is critical for the growth of lateral spin valve transport devices [46]. Sub-monolayer level deposition control also allows films to be grown with specific interfacial terminations and control over surface reconstruc-

tions. Therefore MBE was the chosen growth method for all samples in this dissertation.

The MBE chamber, in its simplest form, consists of elemental source materials and a sample substrate heater, as well as vacuum pumps, which allow the chamber to operate in the regime of ultra-high vacuum (UHV) ($P < 10^{-8}$ mbar). The ultra-high vacuum environment allows molecular species to travel for mean free paths on the order of meters before colliding with another molecule which is crucial to allowing species to arrive on the sample surface without interacting with other molecules [46]. The UHV environment also drastically reduces the concentration of unwanted elemental contaminants in the growing film. For example, carbon incorporated in the growth of GaAs is a strong p-type dopant.

A figure of a typical MBE is shown in figure 2.1. As an example, Pt, Lu, and Sb sources are shown, but in practice, these sources could be any elemental source. Conventionally, source materials are placed inside crucibles that are heated by resistive heating filaments to temperatures where the elemental source begins to either evaporate or sublimate. A typical source temperature, for example, of Ga is held between 800°C-1000°C for evaporation, while for Fe, the typical source temperature is around 1250°C-1300°C for sublimation. The atomic flux coming off of a source is governed by its vapor pressure, which follows Arrhenius behavior as shown in equation 2.1 where k_B is the Boltzmann constant, T is the source temperature, E_A is the activation energy for sublimation or evaporation,

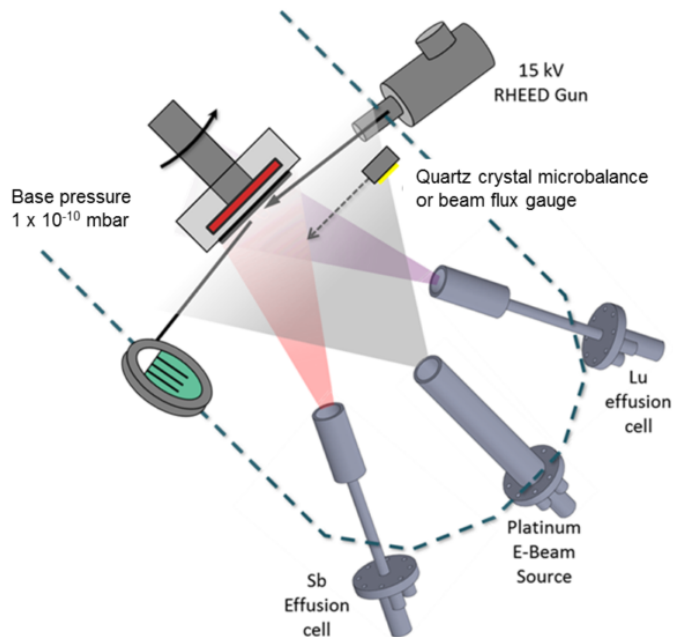


Figure 2.1. A schematic diagram of a molecular beam epitaxy growth chamber.

and A is a prefactor that includes geometry and other factors.

$$P(T) = A \times e^{-\frac{E_A}{k_B T}} \quad (2.1)$$

The determination of E_A and A as well as methods used for flux control will be further discussed in the next section. For materials that have a very low vapor pressure, an electron beam evaporator can be used to provide localized heating in a small area resulting in increased temperature to a point that resistive heating cannot reach, thus allowing for evaporation of the source. The MBE chamber also contains a reflection high energy electron diffraction (RHEED) system which

allows for the monitoring of the crystal during growth.

2.2 More specifics on Heusler growth: flux control and calibration

In typical III-As or III-Sb growth by molecular beam epitaxy, growth rate is controlled by arrival of group III species while a group V overpressure is supplied to the growing surface. The substrate temperature is typically kept at a temperature at which a group V species will only incorporate into the crystal if a group III species is present, otherwise, the group V species will re-evaporate off of the surface. This ensures the growth of stoichiometric crystals in a group III limiting growth regime. Many of the Heusler compounds, however, are made of elements (like many transition metals) which have a sticking coefficient at attainable growth temperatures of 1 or close to 1. This means that precise control of each elemental flux must be obtained to deposit a stoichiometric film.

Calibration of atomic fluxes is carried out by correlation of beam flux measurements from an ion flux gauge to Rutherford backscattering spectrometry (RBS) measurements of elemental films grown at constant flux. The ion flux gauge operates by accelerating electrons emitted from a hot filament towards a positively biased grid. When these electrons collide with the atoms present in the vacuum chamber or molecular beam, they ionize the atoms and molecules.

These ionized particles are collected on a thin wire located in the middle of the grid cage which is held at ground potential. The resulting current measured from this wire to ground is proportional to the number of ions collected and therefore the chamber pressure or molecular beams atomic flux. A picture of a commercially available ion gauge is shown in figure 2.2.

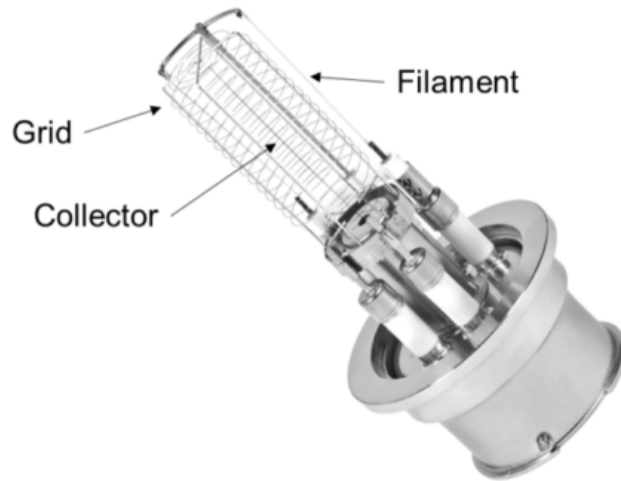


Figure 2.2. A picture of an ion gauge showing the filament, grid, and collector. A similar ion gauge is installed in each MBE chamber for beam flux measurements prior to each growth.

In standard operation, the ion flux gauge is connected to a flux gauge controller, which converts the current into a pressure value. This measurement of beam flux pressure is common in III-V growth by MBE. In our setup, a beam flux gauge controller was originally used to set emission current and grid bias, but the collector was connected to a separate electrometer, which was used to measure the ion current. This allows for the measurement of the ion current with a higher precision, without the influence of any conversions from current to pressure.

To obtain complete control over the ion gauge, since it is crucial for it to operate identically from measurement to measurement, we removed the ion gauge controller completely, and the grid bias and filament current were externally controlled by a current source for the filament and a high voltage source for the grid. This setup currently allows for complete control over emission current and grid bias, and has produced highly reproducible ion-current readings.

To calibrate atomic fluxes for a typical effusion cell, for example, Mn, the cell is ramped up to a set temperature and allowed to stabilize for more than 15 minutes. After the cell temperature has stabilized, an ion flux gauge is positioned in the molecular beam right where the substrate would be located. In the Heusler Gen II system, the sample and ion flux gauge are located on opposite sides of the sample manipulator, so fluxes can be measured while a sample is in the chamber, as it points away from the source flange when the ion gauge is facing the sources. The Mn shutter is then opened, and is left open until the ion current is stable for 30 seconds. This ensures that flux transients from the loss of reflected heat off of the back of the shutter can be eliminated and that the cell has reached steady state before the measurement. In order to subtract out the background chamber pressure from the reading, the shutter is quickly closed, and the ion current is recorded immediately after the shutter closes. After repeating this process to verify that the measurement is precise, the Mn shutter is closed and the sample is then rotated to the growth position. The Mn shutter is then opened and

an elemental, polycrystalline Mn film is grown on a silicon substrate for a set amount of time, which is recorded, to obtain a film that is approximately 10nm thick.

This whole calibration process is repeated at least three times for three different cell temperatures to produce three samples per source. These samples are then sent off for Rutherford backscattering spectroscopy (RBS) analysis to determine the areal atomic density. After determination of the areal atomic density, dividing by the growth time gives an atomic flux for each specific cell temperature and ion current reading. Plotting the natural log of the atomic flux against $1/T$ gives a straight line [Fig. 2.3A], which can then be used to calibrate atomic fluxes for each cell temperature. However, in our experience, atomic flux from a cell at a given temperature can vary greatly over long periods of time, and after cell cool down and warmup. This can be due to effects such as material depletion, oxidation, or redistribution of source material in the crucible. By plotting the atomic flux against the measured ion current [Fig. 2.3B], we also obtain a straight line, which can be used to fine tune the source temperature prior to each growth to obtain the desired flux. This technique is insensitive to effects like depletion, oxidation, and redistribution of source material, because the ion gauge measures the arriving atomic flux at the sample. As long as the overall geometry (i.e. crucible shape, cell position, ion gauge position) does not change, this measurement is fairly precise. Care also must be taken to ensure

that the gauge is operating at a set emission current, with a set bias on the grid and filament to ground (in our case, the grid is biased at +180V and the filament at +24V to ground).

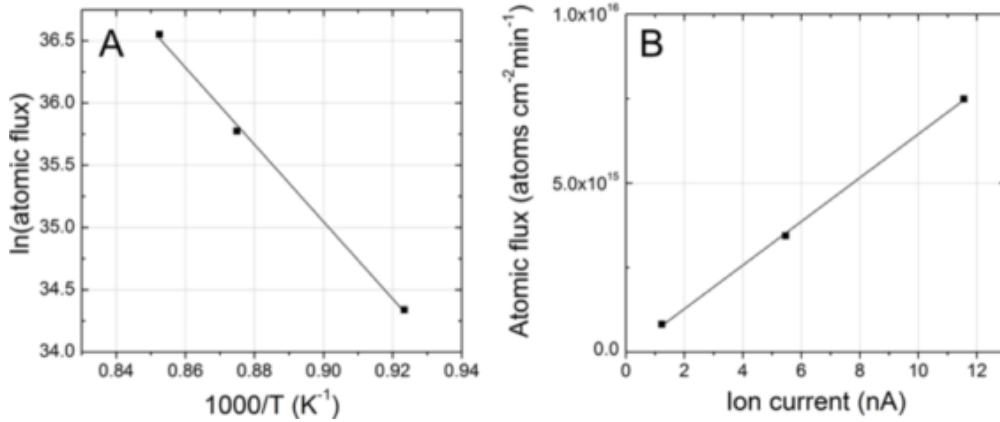


Figure 2.3. (A) Assuming Arrhenius behavior of the thermal evaporation source, the natural logarithm of the atomic flux of Mn, as determined by the growth of elemental Mn films on Si and analysis by Rutherford backscattering spectrometry (RBS), can be plotted against $1/T$ and fit to a straight line to calibrate fluxes. Slight deviations can be seen for this calibration series for the Mn cell. (B) Combining the RBS measurement results with readings of ion current prior to each sample growth, a linear fit between ion current at atomic flux can be obtained, with very little deviation from the fit, and better agreement than using Arrhenius fitting. Since atomic fluxes drift from day to day when sources are held at constant temperature, checking the beam flux gauge pressure prior to each growth is crucial.

For silicon, the same series of RBS calibration samples is grown, but the silicon source is a strip heater, and its flux is controlled by controlling the current through a silicon strip. The flux off of the silicon strip heater must be checked prior to each growth using an ion flux gauge, as the filament thins over time, changing power dissipation and atomic flux. To control the silicon filament, a Labview routine was written to provide controlled current ramps and monitor the output power of the silicon source. These improvements have led to better

control over the silicon flux, as well as an increase in the lifetime of each silicon filament.

For platinum evaporation, an electron beam physical vapor deposition (EBPVD) system is used, and a quartz crystal microbalance (QCM) is used to calibrate flux, as the secondary electrons generated by the source and evaporator affect collector ion currents. The QCM is installed on a linear drive-bellows which allows the crystal to extend next to the sample manipulator for flux calibration, and then be retracted during growths. Since the quartz crystal cannot be positioned directly in front of the sample manipulator, the ratio of the flux that is seen on the QCM to the flux that hits the substrate was calculated by growth of an elemental film on the QCM and the substrate at the same time, and comparing the ending thickness as measured both by the QCM and RBS measurements of the calibration sample.

2.3 *In-situ* growth and surface characterization setup

The samples studied in this dissertation were grown and partially characterized in the *in-situ* growth and characterization setup in Chris Palmstrøms Lab at University of California, Santa Barbara. This system, shown as a schematic diagram in figure 2.4, connects six MBE growth chambers to three scanning

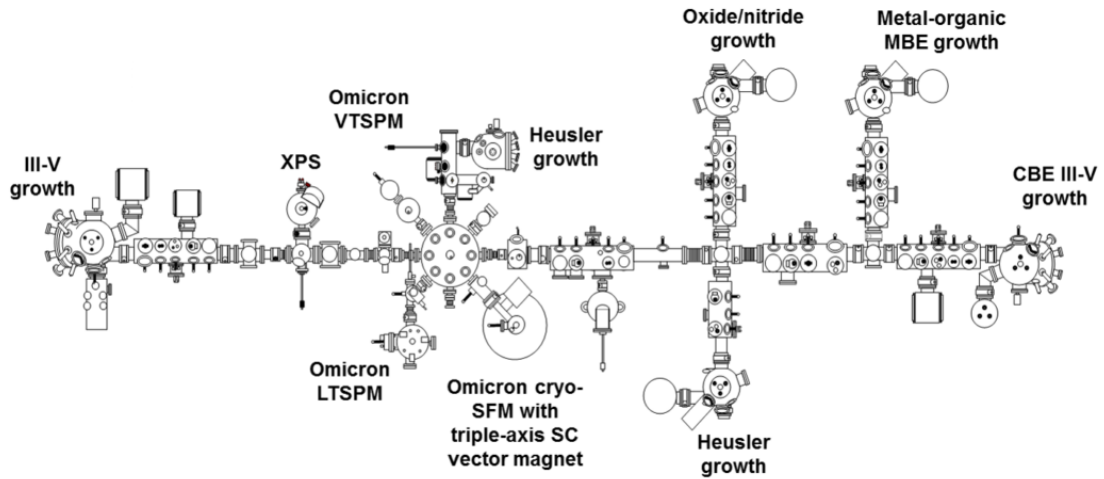


Figure 2.4. A schematic diagram of the Palmstrøm lab *in-situ* growth and characterization setup, with 6 MBE growth chambers, 3 scanning probe microscopes, an x-ray photoemission spectroscopy analysis chamber, and multiple RHEED and LEED diffraction systems. The majority of the sample growth done for this dissertation was on the III-V VG-V80H and the Heusler MOD Gen II EMOF growth chambers, and samples were characterized by XPS and in the Omicron LTSPM.

tunneling microscopes (STM) and an x-ray photoemission spectroscopy (XPS) system for surface characterization. The setup allows for the study of growing surfaces and films without contamination from exposure to air in the transfer process. A few of the chambers were heavily used for this dissertation, including the VG Semicon V80H III-V MBE chamber, the Heusler Veeco MOD Gen II EMOF MBE chamber, the VG Scienta XPS analysis chamber, and the Omicron Low-Temperature Scanning Probe Microscope (LTSPM). In addition to the *in-situ* characterization setup, samples were also studied by angle-resolved photoemission spectroscopy (ARPES) at the beamlines i3 and i4 of MAX-lab in Lund University, SE as well as x-ray diffraction and SQUID magnetometry using a Quantum Design Magnetic Property Measurement System (MPMS) XL

in shared facilities run by the Materials Research Lab at UC-Santa Barbara.

The following sections briefly describe the techniques of scanning tunneling microscopy and spectroscopy (STM/STS) as well as photoemission spectroscopy. A more detailed description and review of these techniques can be found in the dissertation of Jason Kawasaki [1].

2.4 Scanning tunneling microscopy and scanning tunneling spectroscopy (STM/STS)

Scanning tunneling microscopy (STM) and scanning tunneling spectroscopy (STS) are powerful tools that can be used to study the surface topography as well as surface electronic structure of materials. The STM utilizes an atomically sharp tip to scan the surface of a material, similar to the scanning of an atomic force microscopy. However, in STM, sample is biased with respect to the tip, and the tip is held at a distance on the order of Ångstroms away from the samples surface (while never contacting the surface). The bias results in a tunneling current, which is on the order of pA to nA between the tip and the sample. By rastering the tip across the sample and using a feedback loop to control the tip-sample separation in order to keep the tunneling current constant, a convolution of the sample surface morphology and electronic structure can be imaged. A schematic diagram of an STM is shown in figure [2.5](#).

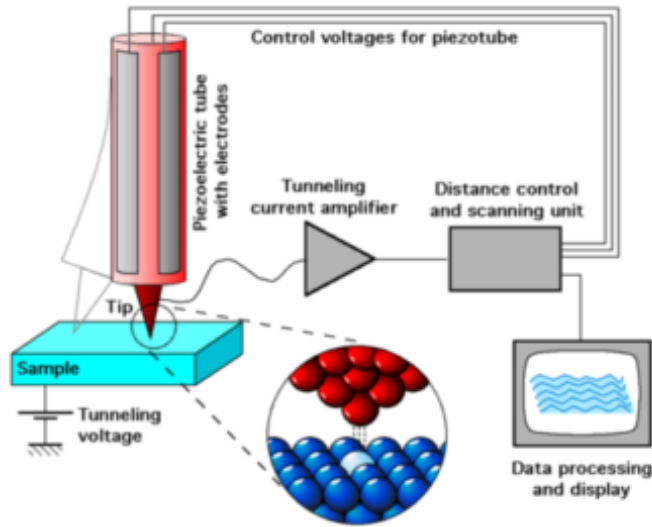


Figure 2.5. A schematic diagram of a scanning tunneling microscope and its related feedback components [47].

From a quantum mechanical description of tunneling, it can be seen that the tunneling current is directly proportional to the convolution of the density of states of the sample and tip, and, if the tip is made from a metal with nearly constant density of states near the Fermi level, the tunneling current is proportional to the local density of states (LDOS) of the sample [48]. Therefore, if the STM tip is kept at the same location, it can be used as a probe of the electronic structure directly under the tip, to the resolution of less than one nanometer.

To accurately probe the LDOS, AC lock-in techniques can be used to perform conductance spectroscopy measurements, where dI/dV is directly proportional to the LDOS [48]. An interesting example of this phenomena is seen in the imaging of subsurface Mn dopants in GaAs (110) surfaces, where the spatial extent of the change in density of states from Mn hole donors [49].

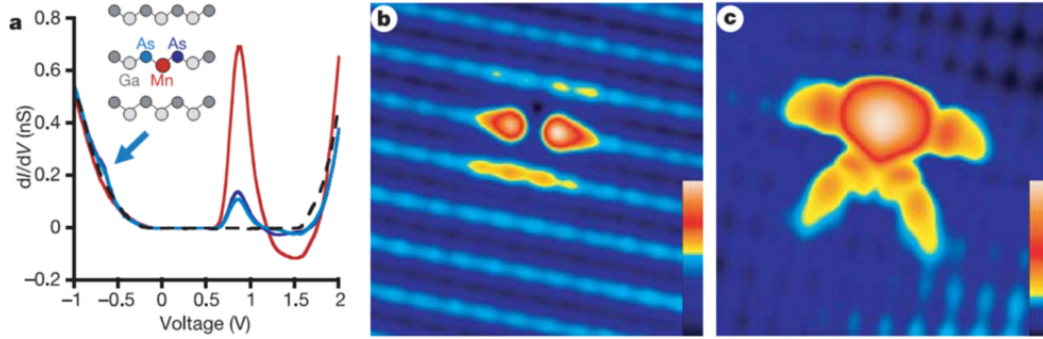


Figure 2.6. (a) dI/dV spectra from areas near a Mn acceptor in (110) GaAs. The red curve corresponds to spectra taken on the Mn acceptor while the blue and purple curves correspond to spectra taken from the neighboring As atoms. (b) 40 \AA^2 height contrast image of the Mn acceptor. A bias of -1.5V results in tunneling from the filled states of the sample to the tip. (c) 40 \AA^2 height contrast image of the Mn acceptor. A bias of $+1.55\text{V}$ results in tunneling from the empty states of the sample to the tip. The shapes observed in panels (b) and (c) show the anisotropic disturbance in LDOS due to the Mn acceptor [49].

Figure 2.6a shows dI/dV spectra on the Mn acceptor and on its neighboring atoms. A small shoulder appearing at the valence band edge is seen in spectra on the As neighboring atoms while a large DOS peak shows up on the Mn atom, due to its acceptor level. Figures 2.6b (filled states, valence band) and 2.6c (empty states, conduction band) show the spatial extent of the effect of the Mn acceptor on the LDOS. This technique therefore allows for a good probe of the surface electronic density of states and provides a strong spectroscopic tool on the *in-situ* growth and characterization setup. This localized spectroscopic and imaging probe was useful in the study of PtLuBi surfaces and surface defects, which will be discussed in section 3.3.1.

2.5 Photoemission spectroscopy

X-ray photoemission spectroscopy (XPS) or angle resolved photoemission spectroscopy (ARPES) is another probe to determine the physical and electronic structure at the surface of a material. Both techniques operate under the photoelectric effect, where light is shined on the sample providing energy for photoemitted electrons to leave the sample and travel in vacuum towards a detector. In XPS or UPS (ultra-violet photoemission spectroscopy) experiments, the light is provided by a beam of monochromatic x-ray radiation. The photoemitted electrons can be analyzed as a function of kinetic energy where $E_{kinetic} = h\nu - E_{binding} - \phi$. $h\nu$ is the energy of the incoming radiation, $E_{binding}$ is the binding energy of the electron, or the difference in energy between its initial state and the Fermi level, and ϕ is the work function. From measurements of a metal in contact with the sample, the work function can be determined, and since the incoming radiation is monochromated and has a known energy, the binding energy can be determined.

If this data is taken as a function of photoemission angle [2.7], information about the energy-crystal momentum dispersion of the photoemitted electron can be determined. Electrons photoemitted from core levels, which are energy levels not involved in bonding, have no E vs k dispersion, so angle resolution does not provide any additional information, but for electrons emitted from the valence band, angular resolution can recreate the E vs. k dispersion for the crystal.

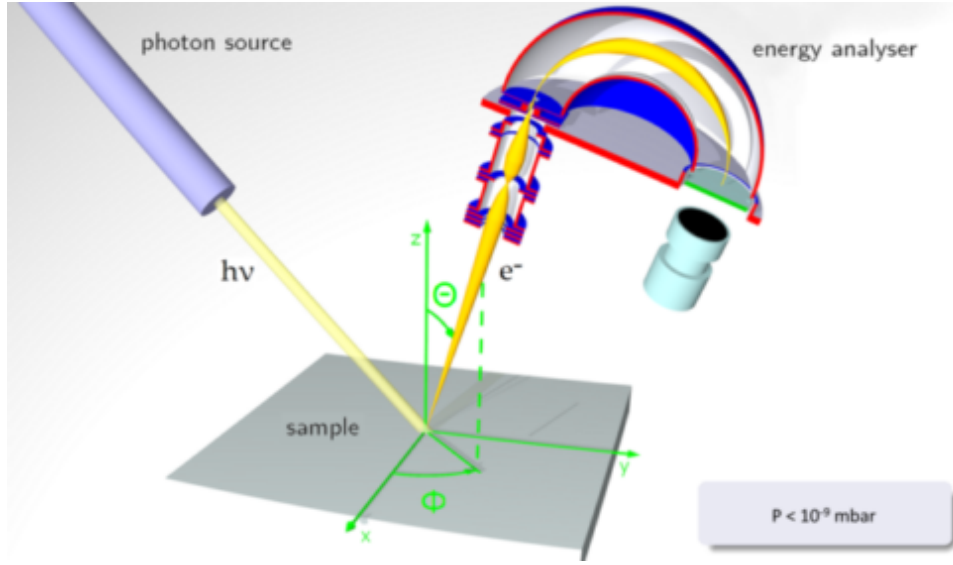


Figure 2.7. A schematic diagram of angle resolved photoemission spectroscopy (ARPES) techniques. When binding energy is mapped as a function of Θ and Φ , E vs. k dispersion of electron states in the crystal can be probed. This figure was adapted from [50].

Photoemission from the valence band can be explained simply using the three-step model developed by Berglund and Spicer [51]. The three steps involved in photoemission are:

1. Optical excitation of the electron from an initial state in the solid to a final state in the solid $[(E_i^s, k_i^s) \rightarrow (E_f^s, k_f^s)]$
2. Transport of the photoelectron to the surface
3. Escape of the photoelectron from the surface into vacuum $[(E_f^v, k_f^v)]$

In this simple model, optical excitation is only allowed for specific optical transitions resulting in polarization dependent intensity. These allowed optical transitions strongly determine measured photoemission intensity and are termed

matrix effects [52].

Using these assumptions, in addition to the assumption that the final state is a "free-electron" state, where $E_f^v = \frac{\hbar^2 k_f^2}{2m_e}$, the final electron state of the detected photoelectron can be related to the initial state of the electron in the crystal. k_f can be broken into two components, one parallel to the sample surface, $k_{f,\parallel}$, and one perpendicular to the sample surface, $k_{f,\perp}$. In the escape process, the in-plane momentum is conserved as the electron leaves the crystal, so:

$$k_{i,\parallel} = k_{f,\parallel} = k_f \sin\theta = \sqrt{\frac{2 m_e E_f^v}{\hbar^2}} \sin\theta \quad (2.2)$$

The perpendicular component of momentum, however, is not conserved, as there is an energy barrier required for the electron to leave the crystal. This energy is termed U_o and called the "inner potential" which can be described as the energy required for the electron to become "free-electron" like [52]. The inner potential is determined using the periodicity of the bulk k_z dispersion from experimental measurements [53]. Using U_o , k_z can be determined from the final state electron energy:

$$k_{\perp} = \sqrt{\frac{2 m_e}{\hbar^2}} (E_f^v \cos^2\theta + U_o)^{\frac{1}{2}} \quad (2.3)$$

These methods for determining the parallel and perpendicular components of momentum are used in the analysis of ARPES spectra of PtLuSb (001) films

using $U_o = 12\text{eV}$.

2.5.1 ARPES measurement instrumentation

Typically soft x-rays and ultraviolet light (less than 200eV) are used for this ARPES due to the high photoionization cross sections at these energies as well as the high energy resolution that can be obtained for monochromated light [52]. At these energies, the inelastic mean free path (IMFP) of electrons [figure 2.8] of photoemitted electrons is extremely short, typically less than 10\AA , so ARPES is a very surface sensitive technique.

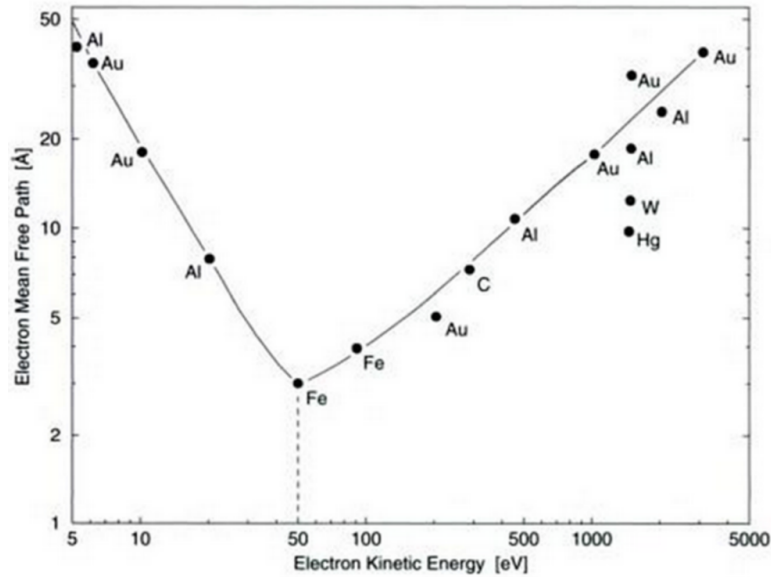


Figure 2.8. The inelastic mean free path (IMFP) universal curve for all elements. This curve does deviate slightly for different materials, but its general shape remains the same. In general ARPES measurements take place at energies less than 200eV, resulting in the detection of photoemitted electrons from less than 8\AA from the surface. This plot is adapted from Ref. [52].

Due to this surface sensitivity, obtaining clean and well-ordered surfaces is

imperative to obtain high quality ARPES data. While the MBE system used to grow the samples is equipped with an *in-situ* XPS analysis system, the x-ray source is fixed energy using Al- $k\alpha$ radiation at 1486eV, making it difficult for measurements of the valence band due to low count rates. Some lab-based ARPES systems currently use laser light sources or monochromated helium lamp light sources, but these sources are not photon energy tunable, so they can only probe certain regions of k-space. Synchrotron sources allow for tuning of photon energy with extremely high photon fluxes as well as monochromated beams. Our measurements at MAX-lab in Lund, Sweden were performed on beamline i4, which provided a tunable photon energy of 14-200eV, and an analyzer with acceptance angle of 15° .

The simplest ARPES measurements capture, with a CCD detector, snapshots of k_{\parallel} vs kinetic energy of electrons at a given photon energy. In order to obtain E-k dispersion in the direction perpendicular to the detector, the sample is tilted with respect to the entrance slit of the detector, and multiple snapshots are stacked up to create a 4 dimensional dataset including two perpendicular k_{\parallel} directions, binding energy, and photoemission intensity.

The surface Brillouin zone, shows electron and hole bands projected from the three dimensional bulk Brillouin zone. The final state momentum, k_f , of the detected electron determines which bulk states are projected onto the surface Brillouin zone. Since the detector detects electrons of a set kinetic energy, in

the simplest sense, the surface Brillouin zone shows the projection of bulk states from a hemispherically shaped surface centered around bulk Γ . By changing photon energy, the final state momentum of the photoemitted electron is varied, so the effective radius of the hemispherical surface is changed, and a different projection of the bulk Brillouin zone is observed.

Since ARPES is so surface sensitive, a surface protection scheme was developed to transfer the samples from the MBE system at UCSB to the ARPES beamline at MAX-lab. This scheme used elemental Sb caps to protect the surface during transport which were then removed at MAX-lab in the beamline i4 prep chamber. This development of this capping and decapping procedure will be discussed in section [3.1.1](#).

2.6 Measurements of spin injection in lateral spin valve heterostructures

Chapter [4](#) will focus on lateral spin transport measurements in Heusler/GaAs(001) heterostructures. Therefore, it is first important to define the methods used for the measurement of lateral spin transport signals.

The epitaxial growth structure consists of a ferromagnetic injector, a heavily doped Si:GaAs ($n = 5 \times 10^{18} \text{ cm}^{-3}$) Schottky contact region and a lightly doped Si:GaAs ($n = 3 \times 10^{16} \text{ cm}^{-3}$) channel region.

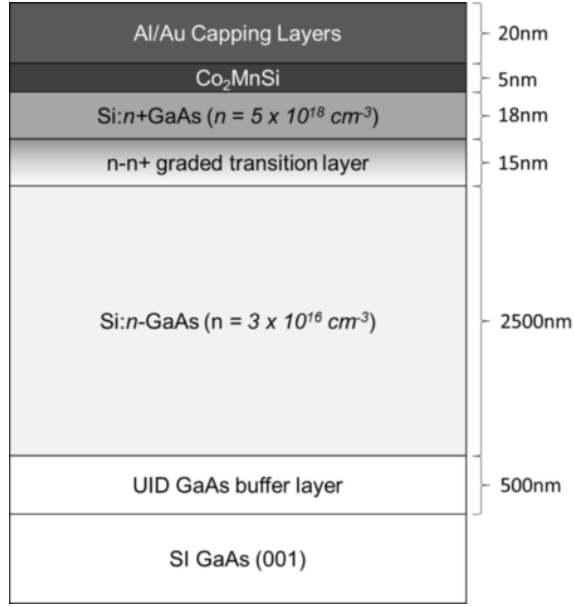


Figure 2.9. Schematic structure of an epitaxial growth stack for lateral spin valve device structures. Samples were grown on semi-insulating GaAs wafers. The Al/Au capping layers were used to protect the ferromagnet from oxidation.

As shown in figure 2.9, the use of a graded doping from the channel to the injector region is employed to smoothen out the conduction band profile in the out-of-plane direction [54]. After growth by molecular beam epitaxy, these samples are fabricated into lateral spin valves. In between the metallic contacts to the surface, the heavily doped GaAs regions are etched away, which allows for injection of spin from the ferromagnet, and then lateral transport through the lightly doped semiconducting layer without any influence of lateral conduction paths through the heavily doped region.

The lateral spin valve structure is shown in figure 2.11, with ferromagnetic contacts B, C, and D, and non-magnetic reference contacts A and E [37]. The distances l_1 are much longer than the spin diffusion length in GaAs, while the

distance l_2 are on the order of the spin diffusion length. In the operation of the device, contacts A and C are used as a current source, while contacts D and E are used for non-local spin detection.

After growth of the heterostructure by MBE, as shown in figure 2.9, the samples are then fabricated into lateral spin valve structures. Ferromagnetic contacts are patterned and etched using ion-milling techniques to remove the ferromagnet as well as the degenerately doped GaAs regions that are not under a contact. The schematic of the device, as well as the measurement geometry, is shown in figure 2.10.

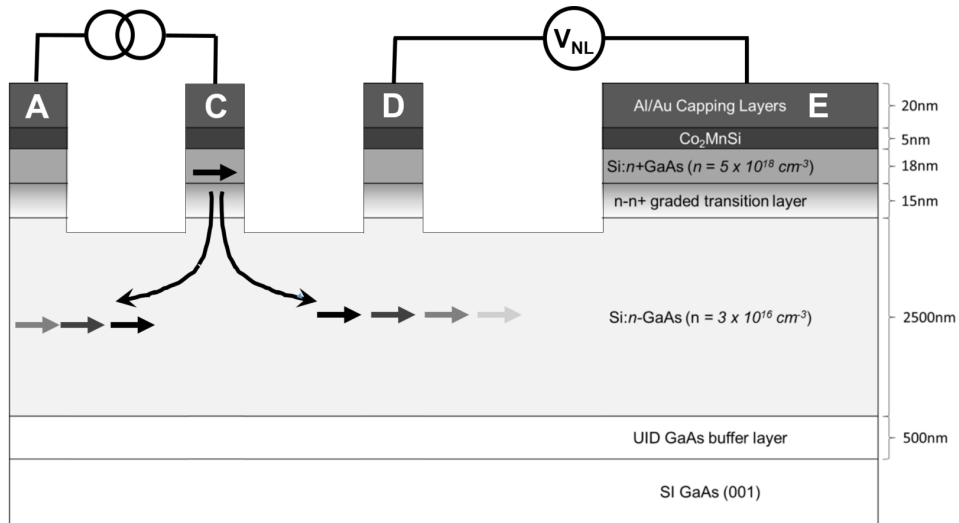


Figure 2.10. Schematic diagram of the fabricated of the non-local spin valve heterostructure devices used for the study of $\text{Co}_2\text{MnSi}/\text{GaAs}$ (001) heterostructures. Spins are injected under contact C and then diffuse in the semiconductor channel where they dephase due to spin-scattering events, then are detected by contact D.

This extraction of current at contact C in figure 2.11 leads to an accumulation of majority spin in the lightly doped GaAs channel, which then diffuses outwards

from contact C. The ferromagnet detection electrode D experiences a shift in chemical potential which is sensitive to the chemical potential of the spin in the channel that is aligned to its magnetization.

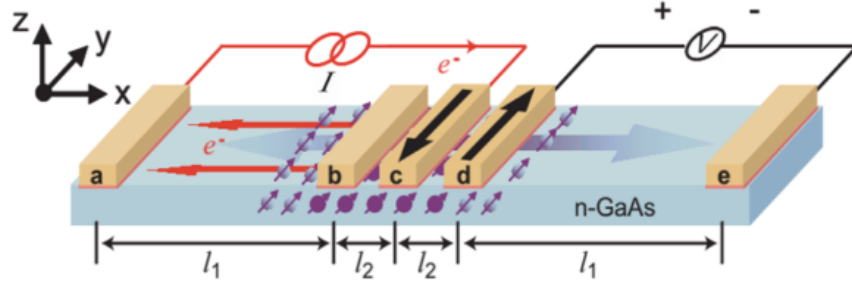


Figure 2.11. Schematic structure of the non-local spin valve devices measured for sample in this dissertation [37].

Two measurements can be taken using this device geometry: non-local spin valve measurements and Hanle measurements. In a non-local spin valve measurement, starting with both contacts, C and D, aligned, magnetic field is swept in an in plane direction which causes contacts C and D become anti-aligned as field is swept from positive to negative values (and from negative to positive values). When the injection contact (C) becomes anti-aligned with the detection contact (D), the result is a jump in the potential measured by contact D, because of the change in sign of the steady state spin accumulation in the channel. This is observed as the field is swept in the positive to negative direction as well as the negative to positive direction, as seen in figure 2.12. The magnitude of the chemical potential shift is referred to as the spin signal [37].

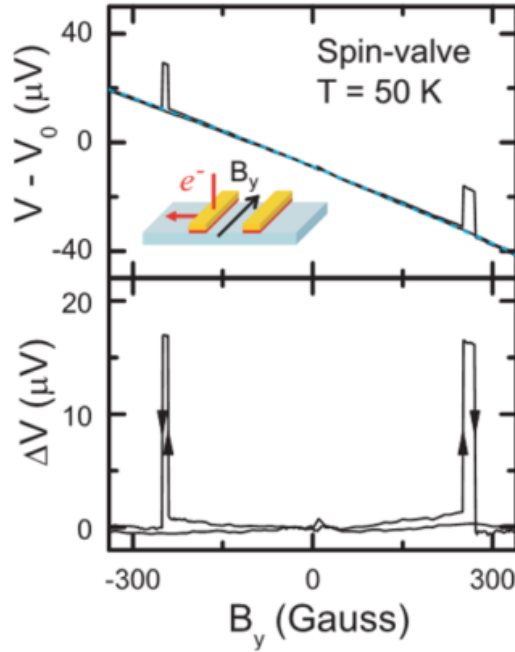


Figure 2.12. A typical spin valve measurement of the non-local spin signal. Field is swept in the plane of the sample to cause the ferromagnetic contacts to flip in-plane. The change in spin accumulation in the GaAs channel is observed by a shift in chemical potential when the detection and injection contacts are aligned vs. anti-aligned. The top panel shows raw data, and the bottom shows the data after the subtraction of magneto-resistive contributions [37].

A verification of the spin dependency of the voltage spike can be done by the measurement of the Hanle effect, in which electron spins can be dephased by the application of a transverse magnetic field, illustrated in figure 2.13 [37, 55, 56]. The Hanle effect can be observed in either the parallel or anti-parallel contact configuration, and at high enough field, the spin dephases completely, resulting in the observation of non net spin signal. Both the non-local spin valve measurement and the Hanle measurement require the subtraction of a background voltage signal which is due to changes in the magneto-resistive changes in the semiconductor.

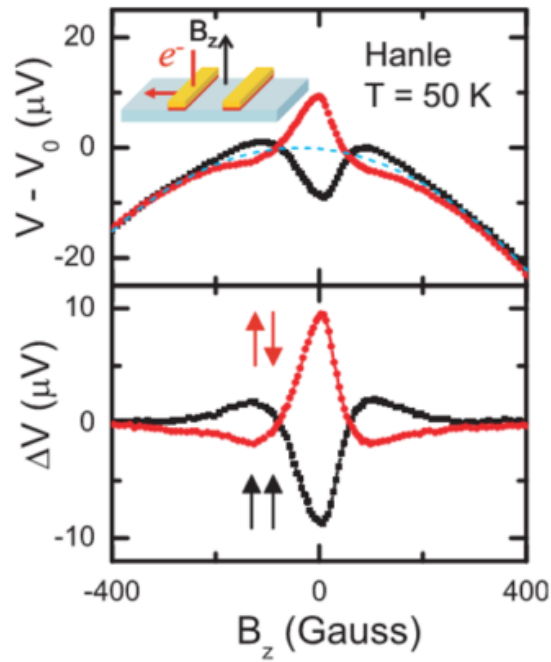


Figure 2.13. An example of a Hanle measurement, where field is applied transverse to the direction of the injected spin, which results in the dephasing of electron spins in the semiconducting channel. This measurement can be done with the injection and detection contacts in either the parallel or anti-parallel configurations. The top panel shows raw data, and the bottom shows the data after the subtraction of magneto-resistive contributions [37].

2.6.1 Biased detector non-local spin valve measurements

The previous section has described a typical non-local spin valve device, where spin can be injected into the semiconducting channel, allowed to diffuse laterally, and then detected by a non-local ferromagnetic contact. In this measurement, the detection contact is purely allowed to shift chemical potential based on the chemical potential of spins in the channel, and no bias is applied to the detected. However, for the samples measured in this thesis, Mn in-diffusion from the Co_2MnSi electrode into the GaAs resulted in the compensation of the Schottky contact, which will be discussed in chapter 4, and the increased Schottky barrier width prevented the observation of a purely non-local spin signal with an unbiased detector. To counteract the effects of the increase in Schottky barrier width, a biased detector scheme was used for these measurements. The setup of the biased detector is shown in figure 2.14, where the detector is forward biased at the same bias as the injector contact. It is important to note that the current from the biased detector flows between the grounded reference contact and the detector, but not to the voltage reference contact, which is floating.

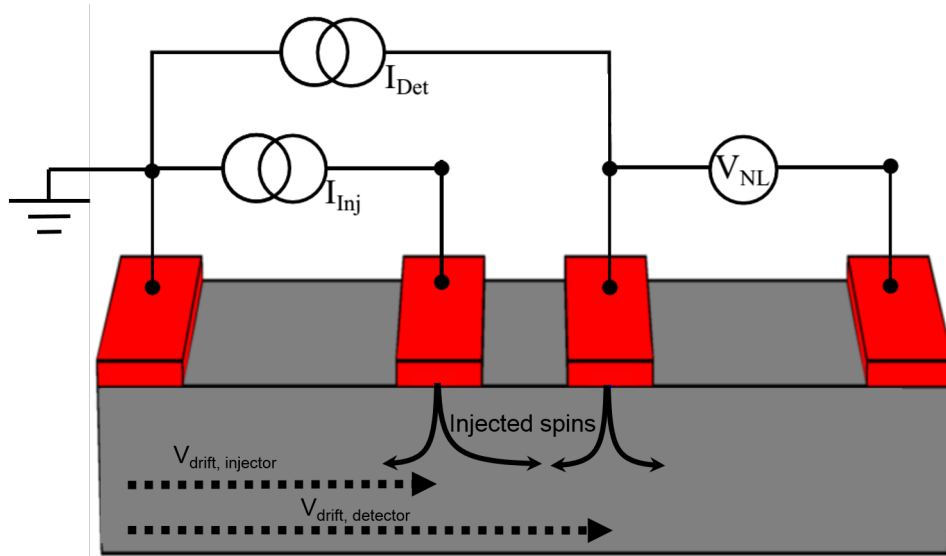


Figure 2.14. A schematic diagram of the biased detector measurement geometry. The detector bias results in an increase in spin injection efficiency, a spin injection into the channel, and an increase in spin drift current as shown by the increased bias contributed from the detector bias.

This bias causes two major effects which allow for the observation of spin signal [57]:

1. The spin detection efficiency changes.
2. The potential shift of the biased detector contact results in an increase in spin drift current in the semiconductor channel.

The spin detection efficiency of the detection contact can be varied greatly by applying a bias. The exact nature of the bias dependence of a FM/semiconductor interface is determined by the interfacial band structure and ordering. These bias dependencies have been studied in depth by Crooker, *et al.*, in 2009, for Fe/GaAs (001) heterostructures. To calculate the detection efficiency, optical

pumping of spins into the GaAs channel was used to create a spin polarization in the channel that was independent of applied biases. The detection efficiency was studied by applying a bias to the detector, then measuring the chemical potential shift of the contact as the spin in the channel was dephased using the Hanle effect. While the details of the study can be found in Ref. [57], the net result is shown in figure 2.15, where the spin detection efficiency is plotted as a function of detector bias. From these results, we can see that the detection efficiency is greatly enhanced at large forward biases.

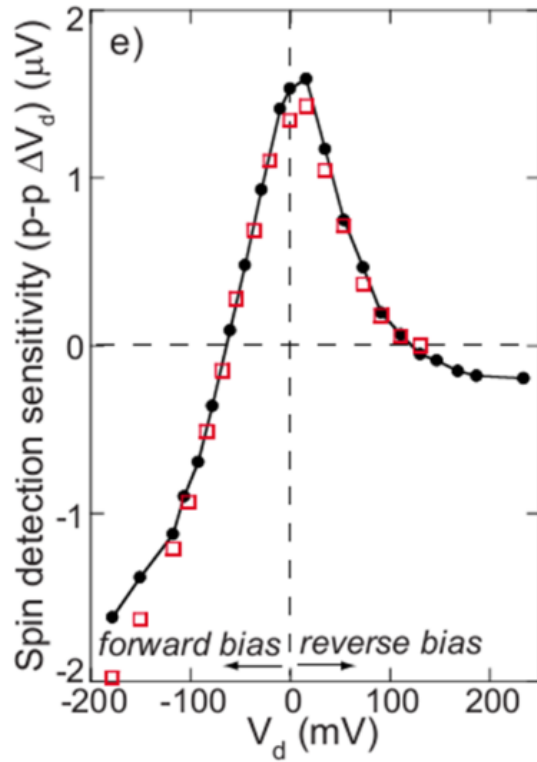


Figure 2.15. The spin detection efficiency of an Fe/GaAs (001) heterostructure as a function of detector bias.

In addition, the application of a bias voltage in the configuration shown

in figure 2.14, results in an additional potential drop over the semiconductor channel. This voltage drop creates a drift current for the spins, pushing the spin diffusion profile further under the detection contact. This shift results in a larger spin accumulation under the detection contact, which also serves to increase the signal detected by the contact. For $\text{Co}_2\text{MnSi}/\text{GaAs}$ (001) heterostructures, the details of the effects of biased detector measurements on spin signal, and the details of the determination of spin accumulation in the GaAs channel using these models can be found in greater detail in the thesis of Kevin Christie from Paul Crowell's group at University of Minnesota.

2.6.2 Determining the sign of spin accumulations in $\text{Co}_2\text{MnSi}/\text{GaAs}$ (001) lateral spin valve devices

Using the non-local spin valve device and measuring the spin-valve signal, as described previously, the sign of the spin accumulation cannot be determined. However, using Hanle effect measurements, the sign of the spin accumulation can be determined. A detailed explanation of the determination of the sign of spin accumulation can be found in the thesis of Kevin Christie [58], but a simple description will follow.

The ensemble of electron spins can interact with the nuclear spins in the GaAs crystal through hyperfine interactions. The sign of the spin accumulation can be determined from measurements of the Hanle effect in the presence of a

hyperfine field .The electrons in the GaAs experience an effective magnetic field from the spin polarization of the GaAs nuclei which is given by

$$\vec{B}_{eff}^n = b_n \frac{\vec{B} \cdot \vec{P}}{B^2} \vec{B}, \quad (2.4)$$

where B is the applied magnetic field, P is the electron spin and b_n is a nuclear field coefficient on the order of a few Tesla with a negative sign for GaAs.[59–61]. By manipulating the applied field direction with respect to the direction of spin polarization, the sign of $\vec{B} \cdot \vec{P}$ can be changed, therefore modifying the effective nuclear field. The effective nuclear field can be measured and studied using ”oblique Hanle measurements” [62], in which the transverse applied magnetic field is slightly canted. The details of this measurement, and how it can be used to obtain the effective nuclear field, can be found in the thesis of Mun Chan [62]. Paul Crowell’s group at University of Minnesota, with their expertise in semiconductor based spin transport measurements and theory, used these techniques to determine the magnitude and sign of the spin accumulation in $\text{Co}_2\text{Fe}_x\text{Mn}_{1-x}\text{Si}/\text{GaAs}$ (001) lateral spin valve devices.

Chapter 3

Half-Heusler topological insulators: PtLuSb (001) and PtLuBi (001) thin films

The proposed existence of a topologically insulating phase in some half-Heusler compounds has recently sparked a great interest in their synthesis and characterization [6–8]. Compared to conventional topological insulators, like Bi_2Se_3 , $\text{Bi}_x\text{Sb}_{1-x}$, and others, the draw to half-Heusler compounds is the extraordinary ability to continuously tune the electronic structure as well as the physical lattice parameter, all while retaining the same cubic $C1_b$ crystal structure. The cubic symmetry, plus the ability to tune lattice parameter, allows these half-Heusler compounds to be easily integrated with conventional elemental semiconductors, such as Si or Ge, and compound semiconductors, such as

III-Vs with zinc blende crystal structure. Being able to incorporate these materials with each other can allow for the fabrication of novel, gateable thin film devices which utilize the unique helical surface states of a topological insulator in conjunction with the well established device structures of conventional semiconductors such as field-effect transistors. Moreover, the difficulties that have been encountered in trying to grow traditional topological insulators and doping them could be overcome in the half-Heuslers by simple alloying to increase or decrease the valence electron count. The flexibility of the system is the strongest attractor to the half-Heuslers, but considerable work must be done to synthesize high quality crystals and study their electronic structures. From the large number of predicted topological half-Heusler compounds, we chose to study two: PtLuSb and PtLuBi [6–8]. These two compounds represent two extremes of the topological band inverted class, with PtLuSb lying right on the border of the topologically trivial and non-trivial states, and PtLuBi having the strongest band inversion. This chapter describes some of the techniques used to grow extremely high quality thin films of PtLuSb and PtLuBi, and characterizations of their electronic structure through scanning tunneling microscopy and spectroscopy (STM/STS), photoemission spectroscopy (XPS, ARPES), and electronic transport measurements.

3.1 PtLuSb Growth and Electronic Structure

Since Heusler compounds are well lattice-matched to III-V semiconductors, and half-Heuslers in particular retain their crystalline symmetries, the choice of the III-V substrate was obvious. For PtLuSb, there were two choices, $\text{Ga}_x\text{In}_{1-x}\text{Sb}$ and $\text{Al}_x\text{In}_{1-x}\text{Sb}$, to grow a lattice-matched buffer. The composition of $\text{Al}_{0.1}\text{In}_{0.9}\text{Sb}$ was chosen because of its larger band-gap than comparable lattice parameter $\text{Ga}_x\text{In}_{1-x}\text{Sb}$ ternaries resulting in more insulating buffer layers. The more insulating buffer layers reduced the effects of parallel conduction in lateral electrical transport measurements. For most of these studies, UID GaAs (001) substrates were used due to their insulating electrical properties at room temperature, but in samples where vertical conductance was required, for example in STM samples and ARPES samples, n +GaAs (001) substrates were used.

The lattice-matched buffer layers were grown in the dedicated VG-V80H III-V chamber. After native oxide desorption under As_4 overpressure at 580°C , 200-500nm of GaAs was grown to trap any remaining impurities and smooth the surface. For vertically conducting samples, GaAs layers were doped with Si to an n-type carrier density of $5 \times 10^{18} \text{ cm}^{-3}$. After GaAs growth, the sample was cooled to 380°C while As was shuttered to retain a As-stabilized $(2 \times 4)/c(2 \times 8)$ surface reconstruction [63]. After residual As was pumped out of the chamber, $\text{Al}_{0.1}\text{In}_{0.9}\text{Sb}$ was nucleated by a 10s presoak of the surface with Sb, followed by the opening of Al and In shutters. Typical V-III ratios were close to 1.2, which

prevented the sticking of excess Sb to the surface at the very low nucleation temperatures required for heteroepitaxial growth [64]. Due to the significant lattice-mismatch of 14.1% between $\text{Al}_{0.1}\text{In}_{0.9}\text{Sb}$ and GaAs, the $\text{Al}_{0.1}\text{In}_{0.9}\text{Sb}$ film immediately relaxed to form a three-dimensional island like structure as observed by the formation of a three-dimensional spotty RHEED diffraction pattern. At this point, the substrate temperature was rapidly ramped to a growth temperature of 450°C for continued growth, which allowed for increased surface diffusivity and a smoothing of the rough three dimensional surface. For samples grown for lateral transport measurements, this layer was grown only to a thickness of 19.4nm, where the RHEED was observed to transition from a spotty pattern, indicating a three-dimensional surface to a streaky one, indicating the smoothing to a two-dimensional surface. At this thickness, an extremely high threading dislocation density is present at the surface at a concentration near 10^{12} cm^{-2} [65] due to the dramatic mismatch between the GaAs and $\text{Al}_{0.1}\text{In}_{0.9}\text{Sb}$, and the lack of film thickness which would allow dislocation lines to cross and annihilate. However, this reduction in film thickness was crucial in reducing the effects of parallel conduction in the $\text{Al}_{0.1}\text{In}_{0.9}\text{Sb}$ layer on transport measurements. For all other samples, the buffer layer was grown to a thickness of 200nm resulting in a smooth surface with a reduced threading dislocation density. The samples were terminated with a mixed, Sb-rich, $(1\times 3)/c(4\times 4)$ surface reconstruction.

Following III-V buffer layer growth, samples were transferred *in-situ* to the

Heusler Gen II MBE chamber. After carefully calibrating the fluxes as detailed in section 2.2, the substrate was heated to growth temperature and a shuttered sequence of Lu, Pt, Sb was used to grow alternating 0.5MLs and build up an epitaxial seed template of PtLuSb. This template was grown to a total thickness of 8MLs after which Pt, Lu, and Sb were codeposited for the remainder of the growth. Initially, atomic flux ratios of 1:1:1 were used at growth temperatures below 300°C, but after determining that PtLuSb (001) surface could be subject to Sb overpressures at higher substrate temperatures without the deposition of elemental Sb [See section 3.1.2], samples were codeposited with Pt:Lu:Sb ratios of 1:1:1.3, similar to those used for III-Sb semiconductors as previously described. Samples grown for lateral transport measurements were capped with 20nm AlO_x from an e-beam evaporator while samples grown for structural characterization were capped with 2nm amorphous Si to prevent oxidation. Samples grown for ARPES measurements were capped with approximately 100nm Sb to protect the sample surface for transport to the beamline at MAX-lab in Lund, Sweden. Section 3.1.1 describes in more detail the sample structures grown for ARPES measurements and the development of the Sb capping and decapping procedure.

X-ray diffraction $\omega - 2\theta$ measurements verified epitaxial growth and crystal quality of the PtLuSb (001) films. Shown in figure 3.1 is a representative $\omega - 2\theta$ scan showing GaAs (002) and (004) substrate reflections, Al_{0.1}In_{0.9}Sb (002) and (004) buffer layer reflections, and (002) and (004) reflections of PtLuSb. The

absence of non-(00l) reflections confirms the epitaxial growth with (001) out of plane orientation. Finite thickness fringes corresponding to a film thickness of $7 \pm 0.1\text{nm}$ are observed around both the (002) and (004) reflections suggesting good, abrupt interface quality. From these measurements, the experimental, out-of-plane lattice constant was determined to be 6.46\AA , in good agreement with published lattice parameters of bulk crystals [66, 67] and well-lattice matched to the underlying $\text{Al}_{0.1}\text{In}_{0.9}\text{Sb}$ buffer layer.

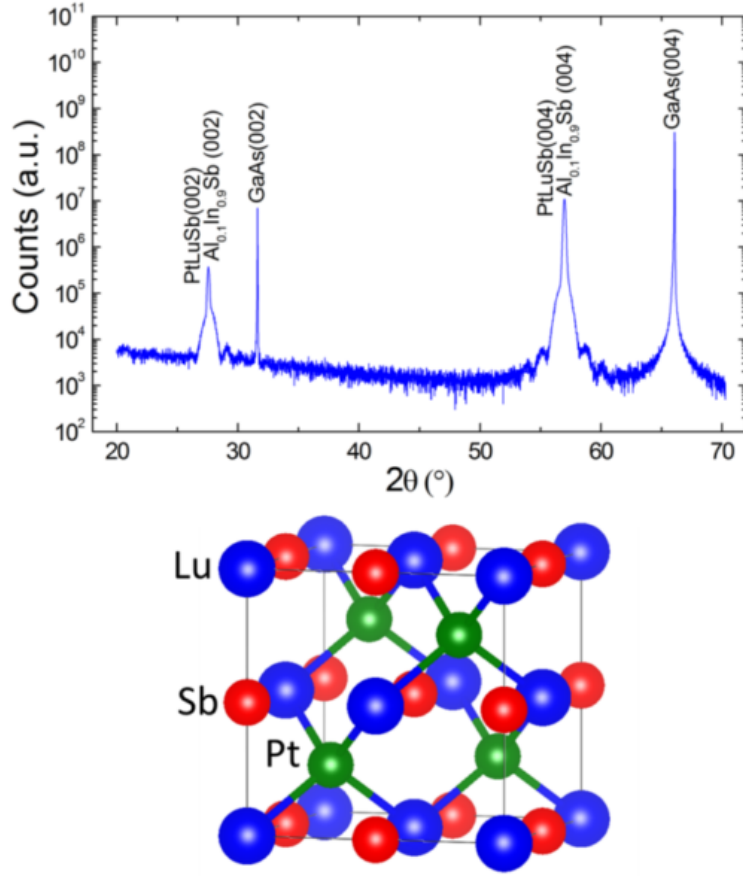


Figure 3.1. Top: X-ray diffraction $\omega - 2\theta$ out-of plane diffraction pattern of a PtLuSb/Al_{0.1}In_{0.9}Sb/GaAs (001) structure. The absence of non-00l reflections confirms epitaxial growth with an out-of-plane lattice parameter of 6.46Å. Bottom: PtLuSb, C1_b crystal structure.

3.1.1 Sb capping and decapping

In order to protect sample surfaces from oxidation and contamination during transport from our MBE growth facility at University of California, Santa Barbara to the beamline at MAX-lab at Lund University, an elemental Sb cap was used. The elemental Sb cap, which has been used before in III-Sb semiconductors [68, 69] and the half-Heusler CoTiSb by Jason Kawasaki [1] was chosen due to

its relatively high vapor pressure at moderate evaporation temperatures, and its presence in the compound PtLuSb. The high vapor pressure allows for thermal desorption of the cap at moderate substrate temperatures and the presence of Sb in PtLuSb eliminates possibilities of the cap reacting significantly with the film. However, for PtLuSb/Al_{0.1}In_{0.9}Sb (001) heterostructures, at the temperature required to thermally desorb the Sb cap ($\approx 380^\circ\text{C}$) significant reactions occur between the PtLuSb and Al_{0.1}In_{0.9}Sb layer, leading to the destruction of the film before decapping. To prevent this reaction from happening, a diffusion barrier was employed. Previous work has demonstrated the use of rare-earth arsenides, including ScAs and ErAs, as diffusion barriers between transition metals and GaAs [70]. However, for the growth of PtLuSb (001) films, these diffusion barriers have two major flaws: (1) the lattice constant of ScAs and ErAs is not large enough for PtLuSb (001) lattice matching and (2) the four-fold symmetry of the rare-earth arsenide rocksalt crystal structure can lead to the growth of rotational variants of two-fold symmetric crystals on top. For our growths, we had the ability to grow GdSb (001) due to the availability of a Gd source in our III-V chamber. While the equilibrium lattice parameter of GdSb (001) is approximately 6.22Å [71], we attempted to grow the material at a thickness of 5ML in attempt to strain the in-plane lattice constant to 6.45Å for PtLuSb (001) growth. At first glance, this procedure seemed to succeed, with the successful growth of PtLuSb films on GdSb. However, upon examination of x-ray diffrac-

tion data, it was clear that the GdSb films relaxed to their equilibrium lattice constant, but remarkably, the PtLuSb films also grew epitaxially and relaxed on that GdSb film. Another interesting result, was that by RHEED and LEED, no rotational domains of PtLuSb were observed, and the final surface was 2-fold symmetric.

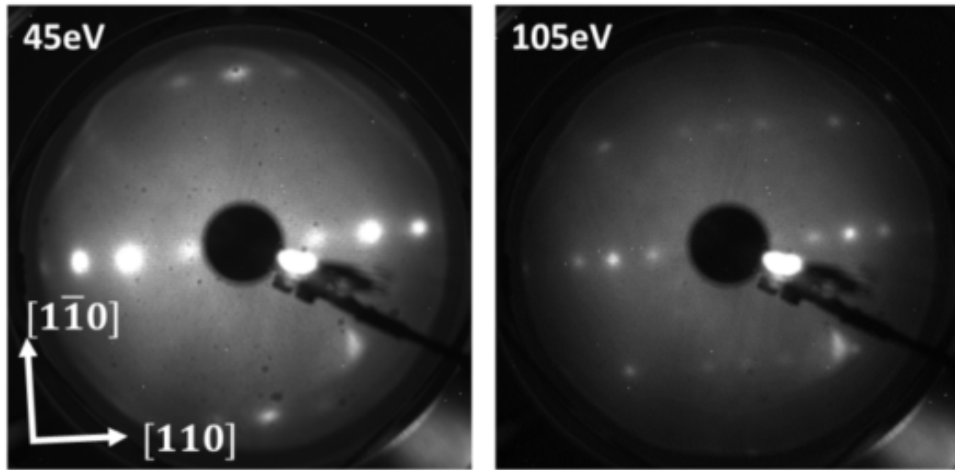


Figure 3.2. LEED images of a decapped PtLuSb (001) surface taken at MAX-lab in Lund, Sweden. A (1x3) surface reconstruction is observed, and the absence of 90° rotational domains is verified by the observation of a 2-fold symmetric LEED pattern.

The growth of the additional GdSb layer allowed access to slightly higher temperature for thermal desorption of the cap. This desorption was verified at the beamline in two ways: observation of (1x3) LEED patterns and by analyzing core level emission in XPS and verifying the absence of Sb-metal components. The LEED patterns are presented in figure 3.2, showing a clear (1x3) pattern. Further analysis of the core level XPS will be presented in section 3.1.2.

3.1.2 Surface reconstructions of PtLuSb (001)

The surface of PtLuSb (001) was observed to reconstruct in two different phases depending on substrate temperature and Sb overpressure: (1x3) or c(2x2). The (1x3) reconstruction was observed at high substrate temperatures and low Sb overpressures while the c(2x2) reconstruction was observed at relatively lower substrate temperatures and high Sb overpressures. By systematically varying substrate temperature and Sb overpressure on a PtLuSb (001) surface, a reconstruction phase diagram was constructed consisting of three regions: (1x3), c(2x2), and Sb capping. RHEED and LEED images of the (1x3) and c(2x2) surface reconstructions are shown in Figure 3.3, as well as the reconstruction phase diagram.

While these reconstructions are stable at the temperature and fluxes described, they can also be retained at room temperature by specific cooling procedures. For (1x3) surface, the Sb overpressure is held at $8.75 \times 10^{14} \frac{\text{atoms}}{\text{cm}^2\text{min}}$ and the sample is annealed at temperatures between 350°C and 380°C until the (1x3) reconstruction is observed. Then, the Sb is shuttered and the sample is rapidly quenched by turning off power to the substrate heater. To retain the c(2x2) surface, samples are first cooled to 330°C under an Sb overpressure of $8.75 \times 10^{14} \frac{\text{atoms}}{\text{cm}^2\text{min}}$ until the c(2x2) reconstruction is obtained, then the Sb is shuttered and the sample is quenched to room temperature.

The similarities to III-V semiconductors in reconstruction phase diagram,

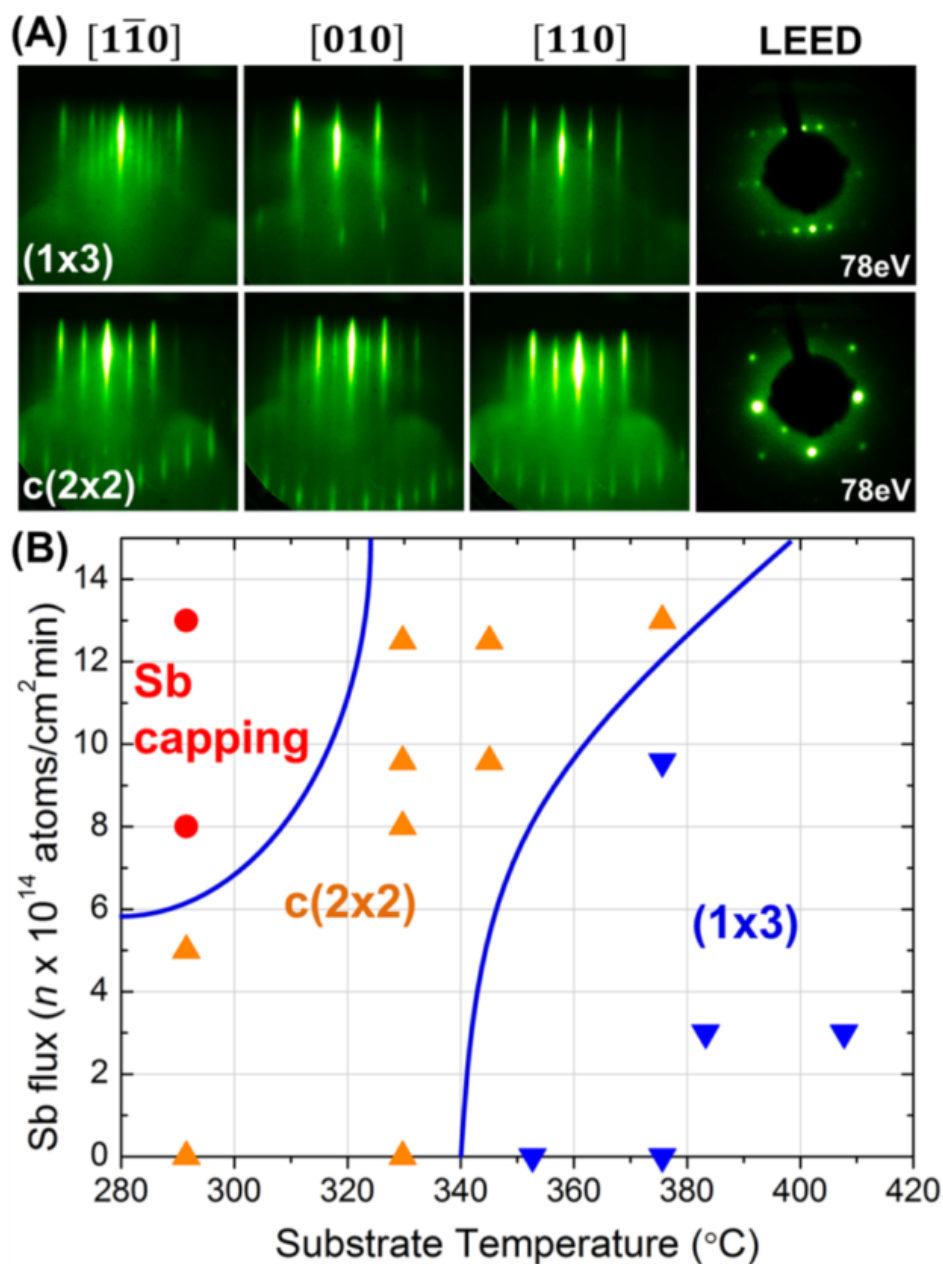


Figure 3.3. Top: RHEED and LEED images taken after stabilization of the (1x3) and c(2x2) surface reconstructions of PtLuSb (001) surfaces. Bottom: Reconstruction phase diagram obtained by varying Sb₄ overpressure and substrate temperature.

where the reconstruction is controlled by group V overpressure and substrate temperature, suggest that group V adsorption and desorption is the most likely

candidate for reconstruction changes [63]. To investigate the nature of the surface reconstruction, Sb 4d core levels were examined by XPS at the i4 beamline at MAX-lab in Lund, Sweden. These samples were capped with elemental Sb, as described in section 3.1, then decapped at the beamline. Figure 3.4 shows the Sb 4d core level for two different photon energies of 90eV and 120eV. Since the core level binding energy of each atom is affected by its surrounding chemical environment, XPS allows for a study of different bonding configurations of, in this case, Sb atoms in or on the PtLuSb crystal. In the bulk, we would expect one Sb component, as each Sb atom has the same local bonding environment. At the surface, we can expect that the local Sb bonding environment changes due to the end of the crystal periodicity, and by studying the shift in energy of the Sb 4d core level, a bonding configuration can be suggested. In this experiment, varying photon energy changes the kinetic energy of the detected electrons for emission from a single core level. This change in energy leads to a change in inelastic mean free path (IMFP) (See Fig. 2.8) of the photoelectron escaping the crystal. Therefore, for the Sb 4d core level, scans taken at a photon energy of 90eV are more surface sensitive than scans taken at a photon energy of 120eV, where the photoelectron can escape from a greater depth due to a longer inelastic mean free path.

To analyze different bonding components, spectra were fit to Voigt functions (Gaussian Lorentzian convolution) for each binding component. The full-width

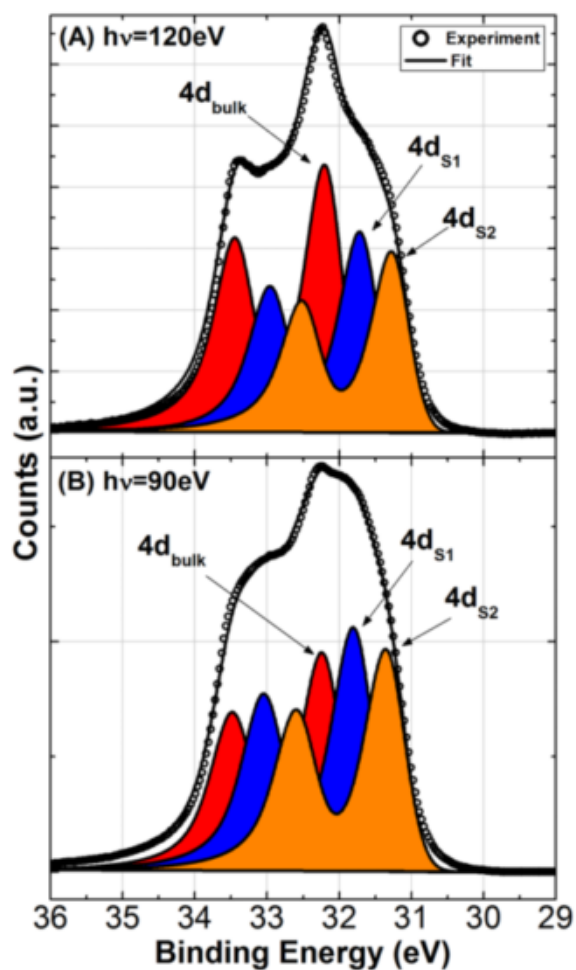


Figure 3.4. (A) XPS spectra of the Sb 4d core level at a photon energy of $h\nu = 120\text{eV}$. (B) Spectrum of the Sb 4d core level at a photon energy of $h\nu = 120\text{eV}$. Three components are fit for each spectrum. The red represents the core level emission from the bulk Sb, while the blue and orange represent emission from surface Sb atoms which have a modified local bonding environment, leading to a shift in the electron binding energy.

half-maximum (FWHM) of each component was held to 0.57eV at $h=90\text{eV}$ and 0.61eV at $h=120\text{eV}$. The energy splitting between the Sb $4d_{5/2}$ and Sb $4d_{3/2}$ spin orbit split components was constrained to 1.25eV for all fits. Three different chemical components are seen in the fitted data. To determine which of the components relate to bulk bonding, the ratio of peaks can be compared at the

two different photon energies. As the 120eV scan is more bulk sensitive, a lower surface component to bulk ratio should be expected. The ratio of the area of the sum of s1 and s2 to the area of the bulk component, is 2.1 at 90eV and 1.4 at 120eV, confirming that s1 and s2 components arise from surface bonding. Additionally, ratio of the area of s1 to s2 is nearly constant at 1.1 for both photon energies. From this analysis, we observe the bulk Sb $4d_{5/2}$ at $31.21 \pm 0.02\text{eV}$, and binding energy shifts from the bulk component: $\Delta\text{BE}^{s1} = -0.46 \pm 0.03\text{eV}$ and $\Delta\text{BE}^{s2} = -0.92 \pm 0.03\text{eV}$. The component s1 is likely associated with Sb dimerization, as the binding energy shift of -0.46eV is similar in energy to shifts observed in III-V semiconductors like GaAs (001) and GaSb (001), which have been attributed to surface dimerization [72, 73]. The component which is shifted -0.92eV from the bulk component represents a more negative Sb atom than those present in an Sb dimer, which could be caused by broken dimer bonds at step edges or broken dimer bonds due to disorder in the surface reconstruction. At these locations, singly bonded Sb surface atoms could have three lone pair electrons surrounding them, which would be a more negative bonding environment than the Sb dimer, which would be surrounded by 2 lone pairs and two bonds. The spectra also show a lack of a higher binding energy Sb surface component, which would be indicative of the presence of elemental Sb at the surface, confirming the complete desorption of the elemental Sb capping layer.

3.2 Electronic Structure of PtLuSb (001) thin films

3.2.1 Measurement of the electronic quality of PtLuSb (001) films

Measurements of carrier concentration and mobility are good metrics to determine the electronic quality of grown films. For PtLuSb (001) films, this measurement proved to be difficult due to the conductivity of the $\text{Al}_{0.1}\text{In}_{0.9}\text{Sb}$ buffer layers. $\text{Al}_{0.1}\text{In}_{0.9}\text{Sb}$, when grown directly on GaAs (001), undergoes a relaxation process that leads to the introduction of a large number of threading dislocations and misfit dislocations to relax the strain. These dislocations, and defects associated with the relaxation process, have been shown to contribute a very large number of carriers to the $\text{Al}_{0.1}\text{In}_{0.9}\text{Sb}$ film [64]. Coupled with the relatively high mobility of $\text{Al}_{0.1}\text{In}_{0.9}\text{Sb}$, this results in a high conductivity for films grown directly on GaAs. Due to the high conductivity of the $\text{Al}_{0.1}\text{In}_{0.9}\text{Sb}$, it is difficult to ensure that the current path for Hall measurements of PtLuSb films remains in the PtLuSb. To overcome this barrier, the thickness of the $\text{Al}_{0.1}\text{In}_{0.9}\text{Sb}$ layer was drastically reduced to 19.4nm, which increased the resistivity of the film, and limited the effects of parallel conduction on the Hall measurements. Additionally, the PtLuSb film was grown 20nm thick, to reduce its sheet resistance and "encourage" transport through that layer.

To verify that this approach was effective, two identical buffer structures were grown: one was capped with amorphous Si and removed from vacuum, and the other was used to grow PtLuSb for measurement, then capped with SiO_x from an e-beam evaporator, and removed. Figure 3.5 shows the resistivity of both samples. The dramatic change in sheet resistance of the PtLuSb sample suggests that transport is dominated by the PtLuSb film. Additionally, thin $\text{Al}_{0.1}\text{In}_{0.9}\text{Sb}$ films have been observed to have high n-type carrier densities [64], which we verified for our sample. Measurements on PtLuSb samples showed a positive, linear Hall coefficients up to 5kOe, suggesting the measurement of p-type carriers with little or no influence from the n-type $\text{Al}_{0.1}\text{In}_{0.9}\text{Sb}$ layer.

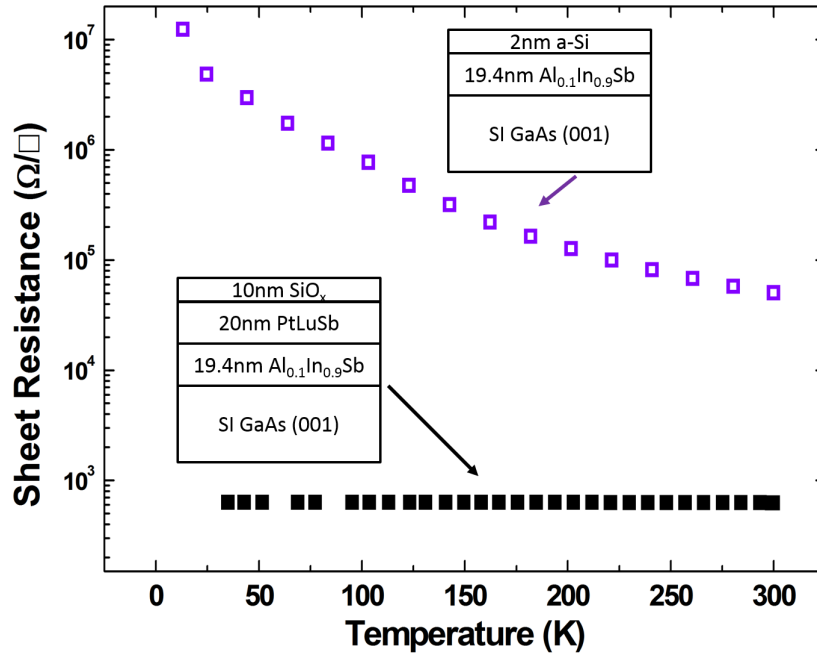


Figure 3.5. Sheet resistance of both samples with purple squares representing just the buffer structure, and black squares representing the buffer structure and PtLuSb film. The dramatic decrease in sheet resistance of the sample with PtLuSb is evident, suggesting that the PtLuSb film dominates transport measurements. [44]

3.2.2 Improving the electronic quality of PtLuSb (001) films

From the reconstruction phase diagram shown in figure 3.3, we were able to determine a growth window where the PtLuSb crystal could be grown with an Sb overpressure, while still retaining the 1:1:1 stoichiometry of a PtLuSb film. The ability to keep a constant overpressure without the growth of excess elemental Sb on the surface of the film suggests that when the substrate temperature is in the right range for a given Sb flux, the Sb terminated surface prevents the sticking of any additional Sb. At an overpressure of $8.75 \times 10^{14} \frac{\text{atoms}}{\text{cm}^2\text{min}}$, the reconstruction

phase diagram shows that from a substrate temperature of 320°C to 390°C leads to a stable Sb terminated surface. To study the effect of Sb overpressured growth on film quality, three samples were grown at substrate temperatures of 320°C, 350°C, and 380°C using Pt:Lu:Sb flux ratios of 1:1:1.3, which corresponded to an Sb flux of $8.75 \times 10^{14} \frac{\text{atoms}}{\text{cm}^2\text{min}}$.

For these three samples, Hall measurements were performed at room temperature using annealed indium contacts in the Van Der Pauw geometry. For all of the samples measured, Hall measurements suggest that holes are the majority carrier from measurement of a positive Hall coefficient. A trend of decreasing carrier concentration with increasing hole mobility was observed for increasing substrate temperatures as shown in figure 3.6.

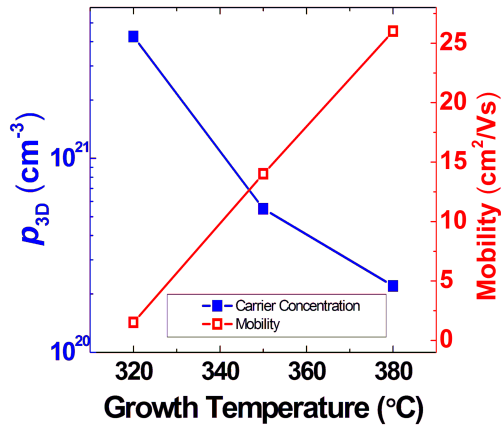


Figure 3.6. Hall measurements taken at 300K of carrier concentration and calculated mobility for PtLuSb samples grown with a 1:1:1.3 Pt:Lu:Sb flux ratio at varying substrate temperatures. A notable decrease in carrier concentration and increase in mobility is observed for higher growth temperatures.

The likely cause of this decreased carrier concentration and increased mobil-

ity is the increase in crystalline quality of the half-Heusler film. High substrate temperatures allows for greater surface diffusivity of adatoms, allowing them to reach their lowest energy site locations and growing a high quality crystal. Another possibility is that increasing growth temperature could lead to a decrease in incorporation of excess Sb. Excess Sb could serve as a point defect and therefore a scattering center for holes, and if incorporated as an antisite defect, could possibly hole dope the material. These results point towards the growth of PtLuSb at even higher substrate temperatures, but a practical limit is reached at 380°C for the PtLuSb/ Al_{0.1}In_{0.9}Sb system, as significant interfacial reactions between the PtLuSb and the Al_{0.1}In_{0.9}Sb occur above this temperature. This opens the door to a search for other suitable substrate for the growth of PtLuSb which are less reactive. There has been some work demonstrating growth on Ta (001) buffers on MgO(001) [74], and other rare-earth arsenide diffusion barriers could be used, but these layers are metallic or semi-metallic, and will serve as unwanted parallel conduction paths for electrical transport measurements and devices. The best candidate will be near lattice-matched to PtLuSb, insulating, and will also possess two fold surface symmetry to match the half-Heusler structure.

3.2.3 Temperature dependent Hall measurements of PtLuSb (001)

Although trends show that higher growth temperatures are likely to improve the properties of the PtLuSb films, an analysis of the temperature dependent carrier concentration and Hall mobility can provide insights into the electronic structure for the best PtLuSb films. A Van der Pauw geometry with annealed indium contacts was used for Hall measurements of the PtLuSb sample grown at a substrate temperature of 380°C as a function of temperature from 35K to 300K. Figure 3.7 shows both the carrier concentration as well as the mobility as a function of temperature.

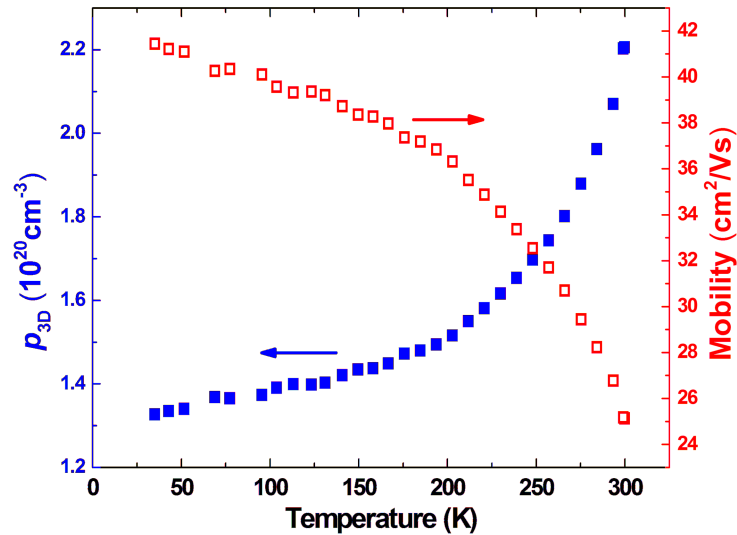


Figure 3.7. Temperature dependent Hall-measurements show a decrease in carrier concentration and an increase in mobility as a function of decreasing sample temperature. These trends are consistent with the transport characteristics of a zero-gap semiconductor. [44]

The p-type carrier concentration measured at room temperature for the PtLuSb film was $2.3 \times 10^{20} \text{ cm}^{-3}$ and decreased to $1.3 \times 10^{20} \text{ cm}^{-3}$ at 35K. The mobility increased from $25 \frac{\text{cm}^2}{\text{Vs}}$ at 300K to $41 \frac{\text{cm}^2}{\text{Vs}}$ at 35K. This sample showed higher carrier densities and lower mobilities than bulk samples that were annealed at 1073K for 2 weeks [66]. A significant decrease in mobility and increase in carrier concentration is expected for the thin film samples, as they were grown on highly defective $\text{Al}_{0.1}\text{In}_{0.9}\text{Sb}$ layers. For InSb/GaAs (001) structures at similar thicknesses, which undergo a similar strain relaxation, threading dislocation densities as high as 10^{12} cm^{-2} were observed [75]. This high dislocation density results in a large number of defects for carrier scattering, and will greatly decrease mobility of carriers. Additionally, these defect cores can serve as "dopants" and increase the carrier density of the film. To reduce these effects, a buffer structure could be grown that would reduce the threading dislocation density in the PtLuSb, and a thicker PtLuSb film could be grown to reduce both the effects of dislocation and interface scattering on the hole transport through the material. Although this structure has not yet been grown, a possible method of reducing threading dislocation density would be the use of a step-graded buffer layer structure grown on GaSb(001) substrate. This would involve a stepped increase in lattice constant from the composition of AlSb, which is nearly lattice matched to GaSb, up to the composition of $\text{Al}_{0.1}\text{In}_{0.9}\text{Sb}$. The step graded layer would create multiple interfaces at which threading components could turn into

misfit components by nucleation of a different lattice parameter in the next step up in indium content. Varying the thickness of the step-graded layers as well as the steps in indium content can allow for control over final threading dislocation density at the PtLuSb film. This optimization will be left for future work.

3.2.4 Scanning tunneling spectroscopy (STS) and ultra-violet photoemission spectroscopy (UPS) of PtLuSb (001)

Hall measurements of PtLuSb show p-type conduction, suggesting a Fermi level position in the valence band, but to study the electronic structure in greater detail and determine the location of the Fermi level, UPS and STS were employed. STM and STS measurements were performed (*in-situ*) at UC-Santa Barbara in an Omicron Low Temperature Scanning Probe Microscope. Shown in figure 3.8 is a topograph of a PtLuSb (001) surface quenched immediately following growth. Highlighted are two regions of atomically resolved (1x2) and (1x3) reconstructions. The (1x2) reconstruction is believed to be metastable and present in these images only due to the lack of annealing under Sb overpressure.

Regardless of the surface reconstruction, STS spectra were identical, suggesting that tunneling was dominated by bulk bandstructure rather than strongly influenced by surface states. The spectra, taken at 78K to reduce the effects of piezo-electric drift as well as adatom diffusion, are shown in figure 3.9a. The

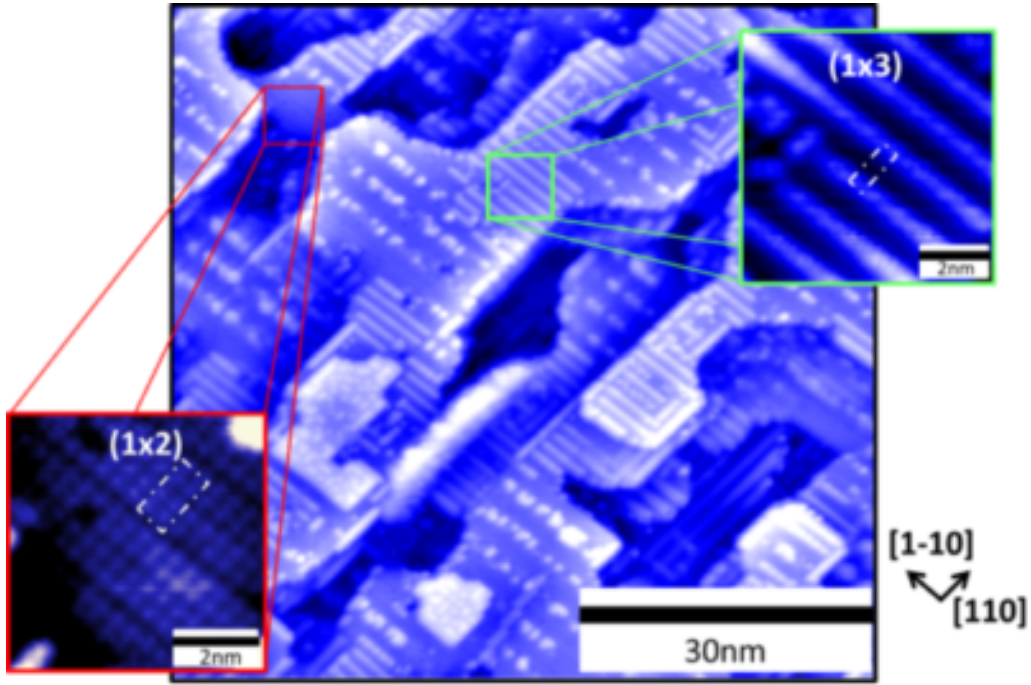


Figure 3.8. STM topographical image of a PtLuSb (001) surface quenched immediately following codeposition. A mixed (1x2) and (1x3) reconstructed surface is observed. This figure was previously published in Ref. [44].

smoothly decreasing density of states of the valence band is in good agreement with both theoretical calculations and measurements of bulk crystals [6–8, 66]. The continued decrease in the LDOS across the Fermi level suggests that the Fermi level lies in the valence band. Two features are observed in STS spectra at 160mV and at 450mV. Positive bias indicates tunneling into empty states, and the LDOS feature observed at 450mV is possibly due to the local minimum at X predicted in the bulk band structure [6]. The LDOS feature at 160mV is possibly related to a light-hole band maximum that occurs above the Fermi level, or may arise due to the presence of a trivial surface state. Further studies will be needed to determine the true nature of the 160mV feature.

For the photoemission spectroscopy measurements described in this section, samples were grown *in-situ* and then capped with Sb, which was desorbed at beamline i4 at MAX-lab in Lund as described in section 3.1.1. The angle-integrated valence band density of states was studied using $h\nu = 50\text{eV}$ light to increase the photoemission intensity from the valence band. Shown in figure 3.9(b), the valence band spectra closely match those measured in bulk PtLuSb crystals and band structure calculations [66]. The continued decrease in density of states at approaching the Fermi level suggests that the Fermi level is located in the valence band, which is in good agreement with both the measurement of p-type carriers by Hall measurements as well as STS measurements and ARPES measurements that are presented in section 3.2.5.

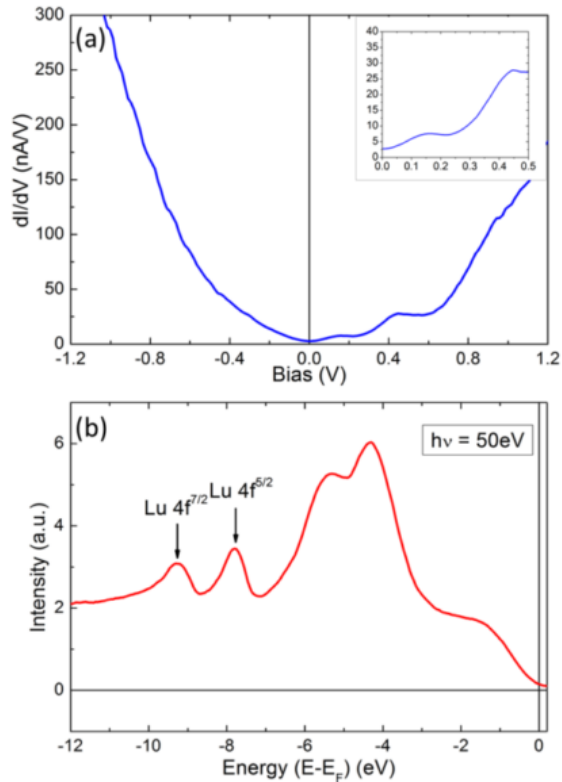


Figure 3.9. (a) STS spectra taken from a PtLuSb at 78K. (001) surface. (b) Valence band spectroscopy using angle-integrated ultraviolet photoemission spectroscopy with an incident photon energy of $h\nu=50\text{eV}$. This figure was taken from Ref. [44].

3.2.5 Angle resolved photoemission spectroscopy (ARPES) of PtLuSb (001) surfaces

To probe the electronic structure of the valence band of PtLuSb (001) films in greater detail, ARPES techniques were used. These measurements allowed for the mapping of not only the bulk band structure, but also the surface states of PtLuSb (001) surfaces.

3.2.6 Normal Emission

Normal emission scans, which reproduce bulk band structure in the direction of Γ to X, are shown in figure 3.10. The values of k_{\perp} were calculated assuming free-electron-like final states, i.e. $k_z = \sqrt{2m/\hbar^2(E_{kin} + U_0)}$, with an inner potential of $U_0 \approx 12.0$ eV. The inner potential was used as an adjustable parameter to match the periodicity of measured bands [53]. Although the resolution of these scans is poor, it is clear that there is a band maximum located near k_{\perp} values of 3.9 and 5.8. By comparison to the bulk band structure of PtLuSb from calculations, these points must correspond to the bulk Γ points. Using a lattice constant of 6.46\AA the expected periodicity of the bulk band structure is 1.94\AA^{-1} , which matches well with the periodicity observed over the whole normal emission dispersion. From this data, a band near a binding energy -0.5eV is clearly observed and does not disperse as a function of k_{\perp} . The lack of dispersion is indicative of a two dimensional state, which is most likely a surface state. The normal emission scans are unclear, but to better investigate the nature of the band structure, and to see the dispersion of the surface state in plane, a more detailed study of k_{\parallel} dispersions is required.

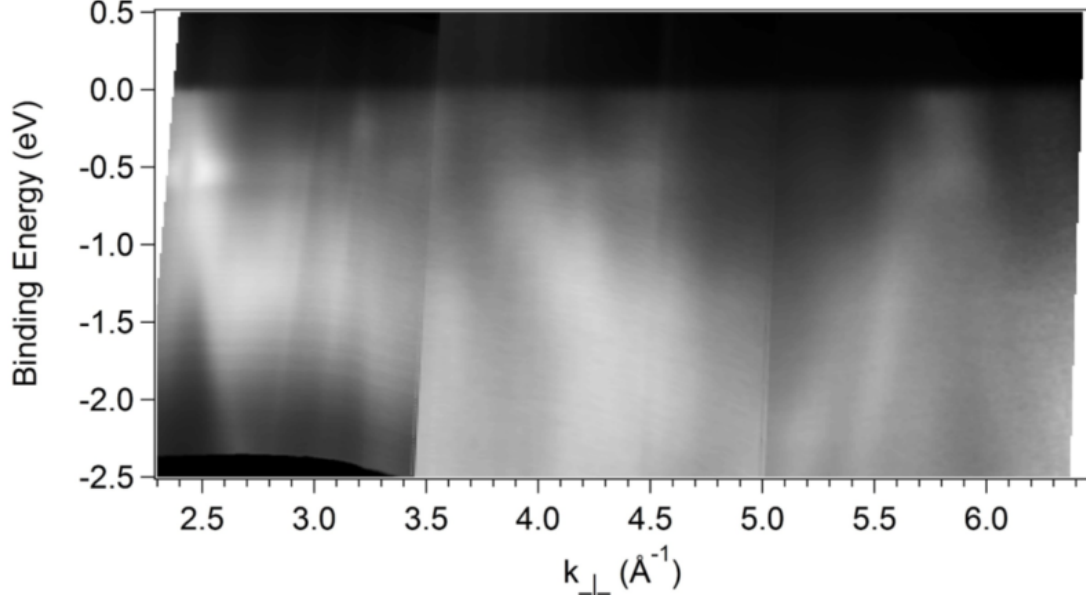


Figure 3.10. A normal emission scan of PtLuSb (001) resulting in the visualization of bulk bandstructure in the Γ -X direction. This data has been converted to values of k_{\perp} or k_z by the assumption that the final state of the electron is free-electron like, and that its escape from the crystal leads to a loss of energy called the "inner potential" which is experimentally determined from the periodicity of the bands. k_z values of 1.8, 3.9, and 5.8 correspond to Γ points while values of approximately 2.7 and 4.8 correspond to X points. This figure is courtesy of John A. Logan.

3.2.7 k_{\parallel} dispersions as a function of incident photon energy

While the visualization of normal emission scans is relatively simple, where dispersing bands correspond to dispersion of k vectors in the Γ -X direction and non-dispersing bands correspond to 2D states, the information contained in one k_{\parallel} vs. binding energy slice gets relatively complex. The reason is that all of bands in a crystal including bulk and surface bands disperse in the $k_x - k_y$ plane. As previously discussed, since the in-plane momentum of the free-electron like state

of the photoemitted electron is preserved while the out-of-plane momentum is not, the resulting k_{\parallel} slice combines surface states and the projection of bulk states that have a k_z component that is determined by the incident photon energy. To deconvolute which states are bulk-like and which are from the surface, we must look at k_{\parallel} slices taken at different photon energies and determine which bands do not change from slice to slice.

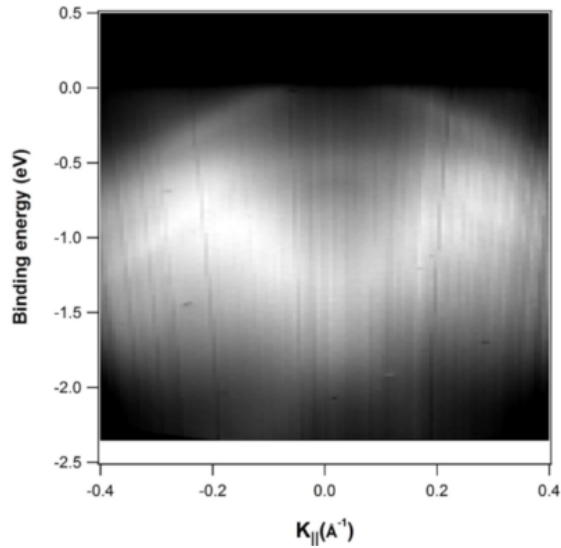


Figure 3.11. An in-plane dispersion slice taken at $h\nu = 16\text{eV}$ showing dispersion in the k_x direction as a function of binding energy.

Shown in figure 3.11 is a long-integration snapshot of a PtLuSb (001) film around normal emission. The incident photon energy for this acquisition was 16eV, which means that states near a k_{\parallel} value of 0 (normal emission) have a k_z value close to the first observed Γ point. Since the in-plane dispersions are projections of a 3D structure onto the 2D surface Brillouin zone, it is impossible to pick out which states are surface states and which are bulk states by looking

at one single frame.

If the photon energy is varied, however, states that are related to the surface should appear exactly the same in each acquisition, while states related to the bulk will change. Shown in figure 3.12a are the in-plane dispersions taken at $h\nu=16\text{eV}$, 18eV , and 20eV . Figure 3.12b shows the second derivative along the energy axis of the same set of data to increase the contrast observed from the bands. There are numerous bands that seem to move with photon energy. There are two sets of states that are not observed to disperse: one is a set of bands that appear 0.5eV below the Fermi level near normal emission, and another which look like linearly dispersing states that cross the Fermi level at a k_{\parallel} value of approximately $\pm 0.13\text{\AA}^{-1}$. The states that appear 0.5eV below the Fermi level are the same states that appear as a constant, non-dispersing band in the normal emission scans shown in figure 3.10. It appears that these are surface states which are spin-orbit split due to their equal displacement away from $k_{\parallel}=0$ in the positive and negative directions. Preliminary spin-ARPES measurements confirm that these bands are non-spin-degenerate, confirming the spin-orbit splitting, but due to the requirement of further analyses of these results, they are not included in this dissertation.

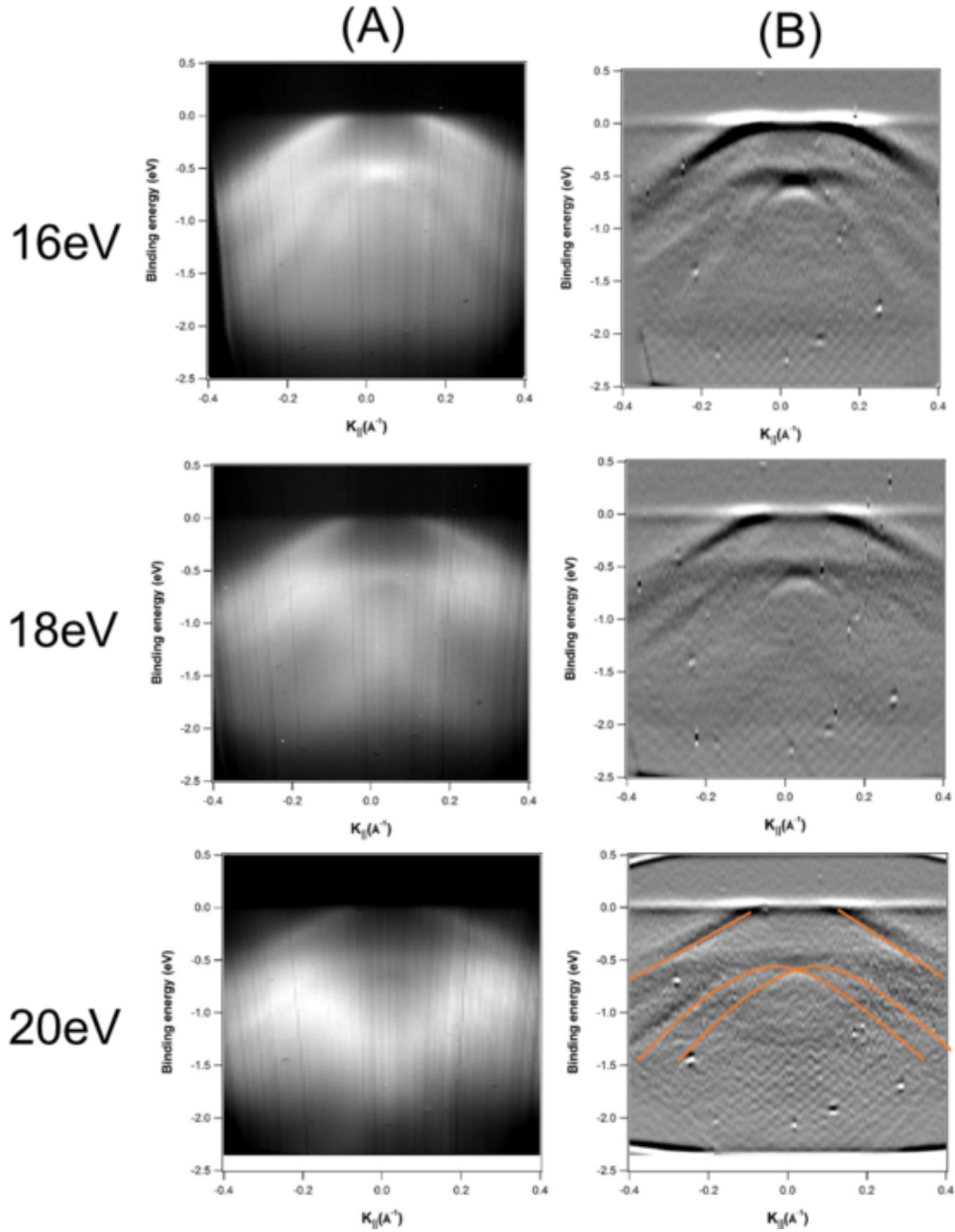


Figure 3.12. (A) Raw data of in-plane dispersions as a function of incident photon energy. (B) Second differential images with respect to both k_{\parallel} and binding energy. Shown at 20eV are highlights of the surface states observed that do not disperse as a function of photon energy. Two bands of a linearly dispersing state appear to cross the Fermi level, while spin-orbit split bands appear shifted in the k_{\parallel} direction with maxima near -0.5eV.

The more interesting surface state is the linearly dispersing state, which, when extrapolated above the Fermi level, can be estimated to reach a crossing point at $\approx +240\text{meV}$ above the Fermi level. This linear dispersion is characteristic of the helical Dirac-like dispersions of topological insulators [16–18]. To verify that this state does not disperse, k_x as a function of k_z can be plotted at a binding energy of -150meV , right below the Fermi level [Fig. 3.13].

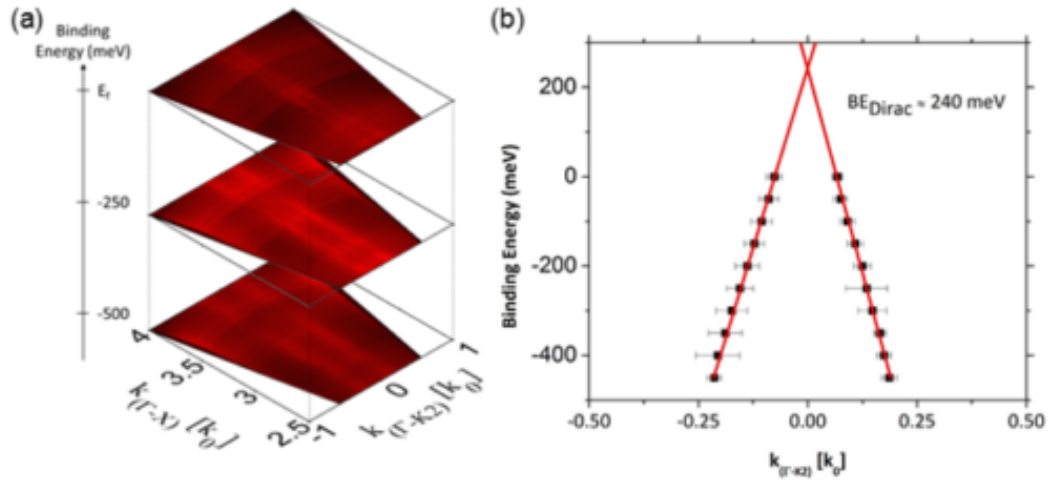


Figure 3.13. (a) The linearly dispersing surface state can be viewed in a plot of k_z vs k_x as a non-dispersing state at various binding energies. Since the state is not present in the valence band at $k_x = 0$, it cannot be observed in the normal emission scans shown in figure 3.10. (b) The surface state’s k_x vs binding energy can be extrapolated from the data and plotted to find a band crossing point approximately 240meV above the Fermi level. This figure is courtesy of John A. Logan.

These dispersion maps verify that the Fermi level is located approximately 240meV below the zero-gap point of PtLuSb. Additionally, surface states are observed, and the presence of a linearly dispersing state suggests a topologically non-trivial nature of PtLuSb (001) films.

3.2.8 spin-ARPES of linearly dispersing surface states

To investigate the spin texture of the linearly dispersing surface state observed in PtLuSb (001) films, spin resolved ARPES measurements were taken. The measurements were taken at an incident photon energy of $h\nu=16\text{eV}$ at two locations on the Fermi surface that had equal and opposite k_x and k_y wave vectors as shown in figure 3.14.

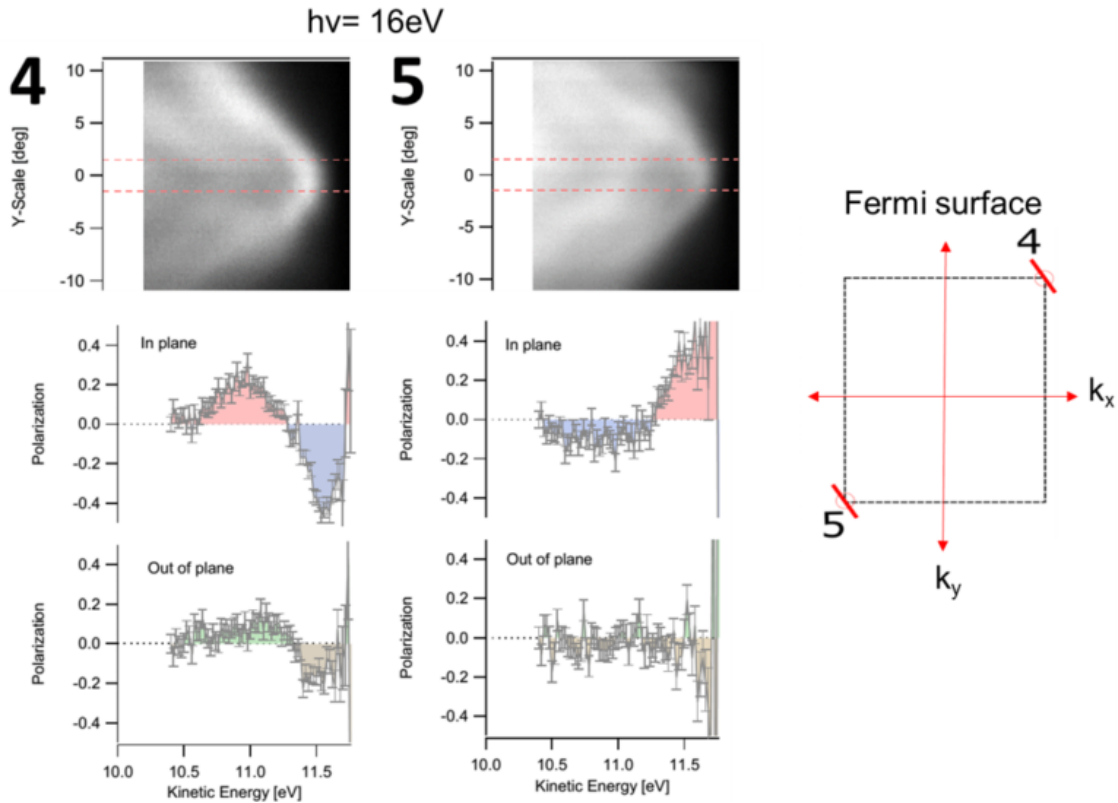


Figure 3.14. Preliminary spin-ARPES measurements of the linearly dispersing surface state. Shown is a schematic diagram of the Fermi surface (right) in dotted black lines. Spin polarization measurements were taken at cuts 4 and 5, shown on the left, in a direction tangential to the Fermi surface. Shown are the spin polarizations measured for the in and out of plane directions within a region of the ARPES spectra denoted by the dotted red lines. The results suggest that the surface state has a strong helical spin polarization with spins lying in-plane at cuts 4 and 5.

The two slices are labeled 4 and 5. By subtracting the intensities of two anti-parallel spin directions that were tangential and in-plane to the Fermi surface, we were able to observe a strong spin polarization, as seen in figure 3.14 in both cuts 4 and 5 (above a binding energy of 0.5eV) which are equal in magnitude and opposite in sign. Also shown are the spin polarization of states in the out-of-plane direction, where the magnitude of the signal is much smaller than the in-plane signal. This suggests that the spin polarization at cut 4 is opposite of the spin polarization of cut 5, and the linearly dispersing surface state has a strong helical spin polarization that is tangential to the Fermi surface with an in-plane spin orientation.

3.2.9 Summary

This study found that PtLuSb (001) films could be grown epitaxially on $\text{Al}_{0.1}\text{In}_{0.9}\text{Sb}$ (001) buffer layers, and that PtLuSb (001) surfaces reconstruct in either $c(2 \times 2)$ or (1×3) unit cells. The $c(2 \times 2)$ reconstruction is believed to be more Sb-rich, as it occurs at lower substrate temperatures and higher Sb overpressures than the (1×3) reconstruction which occurs at higher substrate temperatures and lower Sb overpressures. The nature of the surface reconstruction for the (1×3) reconstruction was determined to be Sb-Sb dimerization by investigation of the Sb 4d core level emission using variable photon energies at MAX-lab in Lund, Sweden. By verifying that there was a window where excess Sb did not stick

on the surface after the surface reconstruction was stabilized, a growth window was discovered where PtLuSb could be grown at an atomic flux ratio of 1:1:1.3 of Pt:Lu:Sb. Investigation of the film properties within this growth window suggests that higher substrate temperatures lead to the highest quality films with an eventual limit at 380°C due to significant reactions between the film and the $\text{Al}_{0.1}\text{In}_{0.9}\text{Sb}$ substrate. Higher quality films may be obtained by growing on different substrates, but it is difficult to find a lattice-matched insulating substrate for these films. However, the possibility of discovering a substrate where a coincident lattice-match is used remains promising.

By improving growth techniques, we were able to study the electronic structure of PtLuSb (001) surface by both scanning tunneling microscopy and ARPES. STS and photoemission measurements confirm the position of the Fermi level in the valence band of PtLuSb and match well with predicted band structures. A linearly dispersing state was observed as well as spin-orbit split surface states through ARPES measurements. Preliminary measurements of the spin texture of the linearly dispersing state suggests that PtLuSb is topologically non-trivial. These promising results will be the subject of future study, as the complete spin texture of this surface state needs to be investigated and compared to theoretical spin-texture predictions.

3.3 PtLuBi (001) Thin Films

Using techniques developed for the growth of PtLuSb (001) films on $\text{Al}_{0.1}\text{In}_{0.9}\text{Sb}$ buffer layers, epitaxial PtLuBi (001) films were also grown. These films are predicted to be semi-metallic at the equilibrium lattice parameter, but can also become gapped upon application of strain [8]. The bulk lattice constant, however, for PtLuBi has been reported to be 6.578\AA [9, 76], which is much larger than attainable by conventional III-V semiconductors. For the growth of this compound, InSb (001) buffer layers were grown with a lattice constant of 6.49\AA to get the closest lattice match to PtLuBi.

Similar to the growth of buffer layers for PtLuSb (001) films, (100nm) InSb (001)/GaSb (001) buffer layer structures were grown in the VG-V80H III-V MBE chamber, then transferred in ultra-high vacuum to the Heusler Gen II chamber in which the PtLuBi films were grown. Two difficulties were encountered during the growth of PtLuBi films directly on InSb (001) that were not previously observed in the growth of PtLuSb: Bi reactions with the InSb (001) surface destroyed the epitaxial interface, preventing further epitaxial growth and the Bi incorporation rate in the crystal at growth temperatures in excess of 350°C was greatly reduced. To counteract the effects of Bi reaction into the surface, 8 ML thick PtLuSb (001) films were used as an interlayer and grown directly on the InSb (001) surfaces. These interlayers served to prevent Bi from diffusing into the InSb layer. To ensure Bi incorporation a low substrate temperature of 270°C

was used for growth using atomic flux ratios of 1:1:1. Unlike PtLuSb films, no growth window has been discovered that allows for Bi overpressured growth. This is likely due to the relatively lower vapor pressure of Bi, which leads to an increased sticking coefficient.

A shuttered growth sequence was used to grow both the PtLuSb interlayer as well as an 8ML thick seed layer of PtLuBi as previously described in section 3.1. To study the growth mode of codeposited PtLuBi films, Pt, Lu, and Bi shutters were opened simultaneously allowing for a natural ordering limited by surface diffusion. For these growths, intensity oscillations of the spectral RHEED beam were observed, confirming a layer-by-layer growth mode with a period corresponding to the growth of a PtLuBi bilayer, or one-half of the unit cell. This layer-by-layer growth mode is similar to the growth mode observed in both PtLuSb and Co_2MnSi films where step heights correspond to complete bilayers, and no monolayer steps are observed. RHEED images of a typical PtLuBi (001) surface after growth as well as the RHEED intensity oscillations during codeposition of Pt, Lu, and Bi are shown in figure 3.15.

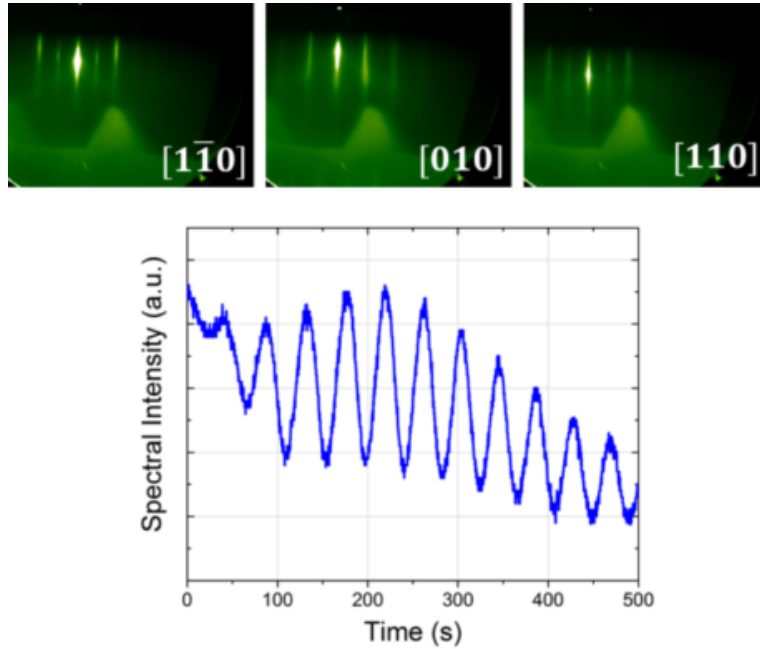


Figure 3.15. RHEED diffraction patterns along the $[1\bar{1}0]$, $[010]$, and $[110]$ azimuths of PtLuBi suggest epitaxial growth with a single in-plane orientation. Also included is the intensity of the spectral RHEED beam as a function of growth time. The period of oscillation is 42.8s and corresponds to the growth of a PtLuBi bilayer as calibrated by beam flux calibrations.

3.3.1 STM PtLuBi (001) surfaces

To study the morphology of PtLuBi films, samples were transferred *in-situ* to an Omicron Low Temperature Scanning Probe Microscope (LTSPM) which was kept at 78K to reduce the effects of piezoelectric drift and adatom diffusion on the sample surface. Large area scans of the PtLuBi (001) surface show a terraced surface with terraces covered in bilayer deep holes [Fig. 3.16].

The terrace height corresponds to a bilayer of PtLuBi as expected from the observed RHEED intensity oscillations. Upon closer observation, many of the "holes" in the terraces are related to spiral-like growth around threading dis-

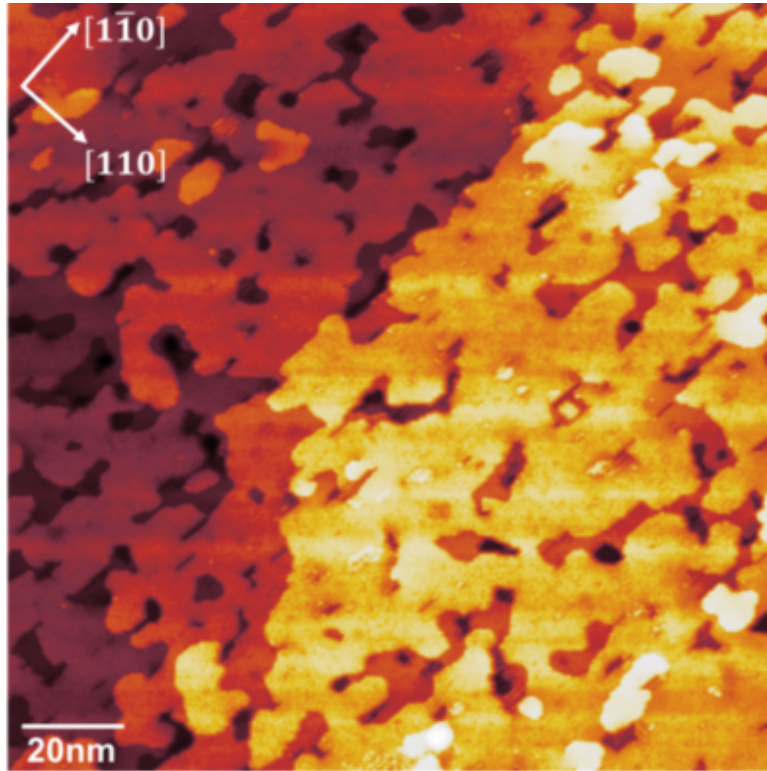


Figure 3.16. STM topographical image of a 4nm PtLuBi/8ML PtLuSb/100nm InSb/GaSb (001) heterostructure. The image was taken at a tip-sample bias of +100mV and a current of 900pA. Step heights correspond to $\approx 3.3\text{\AA}$ or one half unit cell of PtLuBi, in good agreement with the period of RHEED intensity oscillations. A number of dislocation spirals can be observed in the image.

locations with screw-like character at the surface. By counting the number of spirals, an estimated threading dislocation density of $\approx 2 \times 10^{11} \text{ cm}^{-2}$ can be determined. The high threading dislocation density is likely a result of both the InSb(001) buffer layer relaxation on the GaSb(001) substrate as well as the additional relaxation of the PtLuBi film on the InSb buffer layer which both serve to nucleate additional threading dislocations. The absence of spiral hillock growth is likely due to the relatively low substrate temperatures during growth which leads to a decreased surface diffusivity and the inability of adatoms to diffuse to

the lowest energy positions at the dislocation spiral. Looking closer at the step edges in the topographical image, clear faceting can be observed in $\langle 010 \rangle$ and $\langle 110 \rangle$ directions, a characteristic typical of (001) Heusler compound surfaces [1, 44].

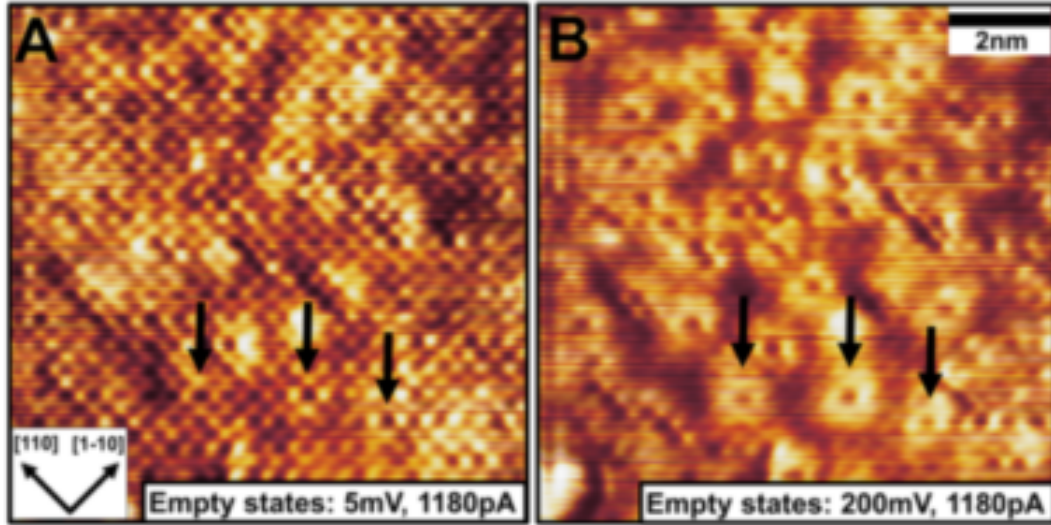


Figure 3.17. Atomic resolution topographical STM images of PtLuBi (001) surfaces. The two panels are taken from the same location at a constant tunneling current of 1180pA with a tip-sample bias of (A) +5mV and (B) +200mV. Three black arrows denote a subsurface atomic defect which is visible in both images. At a tip-sample bias of +200mV, the defect becomes most evident, as a local electronic structure change around the defect site is visualized as a "donut" like feature.

A closer inspection of the surface shows a number of atomic scale defects. Figure 3.17 shows two images of the same area of the sample, one taken at a tip-sample bias of (A) +5mV and the other (B) at +200mV. At +5mV two "brighter" atoms are observed on either side of the defects, which are noted by black arrows. Increasing the tip-sample bias makes these defects more obvious, and their shape is "donut"-like. As this "donut" shape is much more clearly

visible at +200mV, and is very sensitive to the tip-sample bias, it is likely that these features are atomic defects that cause a longer range perturbation to the crystal potential which is visualized by the STM as it is very sensitive to the LDOS. To check the influence of the defect on the measured LDOS, the STM tip was held above the defect site and scanning tunneling spectroscopy (STS) was used to study the exact LDOS on and around the defect.

In these experiments, the technique of varied tip-sample separation, or varied- z spectroscopy, was used, and normalization of dI/dV spectra developed by Feenstra was performed [77, 78]. This technique increases the dynamic range and therefore the sensitivity of dI/dV spectra at low tip-sample biases, allowing for the observation of fine LDOS features at both low tip-sample biases and high tip-sample biases using the same set of lock-in electronics. Figure 3.18 shows an expanded view of three defects near the top of the frame, and a defect free area at the bottom, as well as three representative tunneling spectra taken from different locations on the surface.

Panel A and B show representative spectra taken on the defect site, while panel C shows representative spectra taken from a non-defective area. The shapes of the three spectra are very similar, with peak features evident at -1800mV, -1400mV, +500mV and +1000mV. However, as indicated by black arrows, a peak at approximately +200mV bias is only present for spectra taken around the defect site, and vanishes at spectra taken away from the defect site.

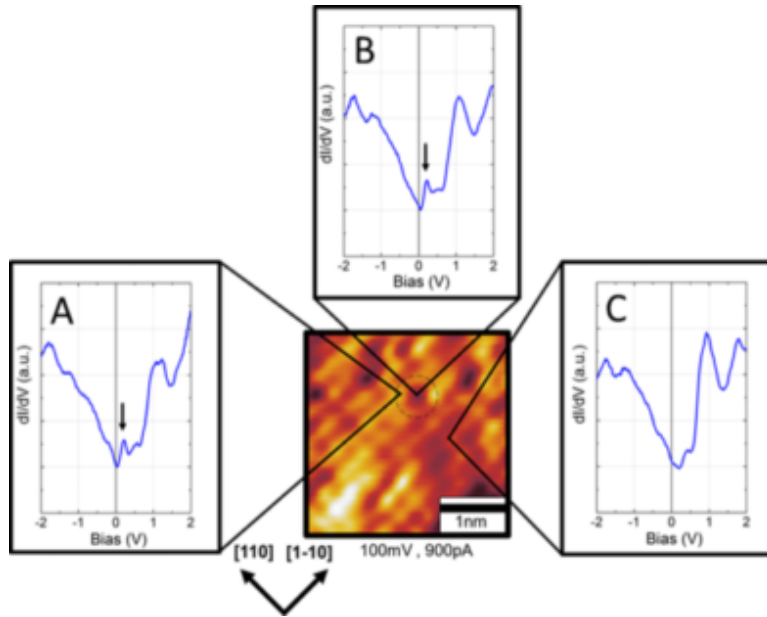


Figure 3.18. An STM image shows three defects near the top of the frame and none near the bottom. Panels (A), (B), and (C) represent STS spectra taken from the noted locations on the PtLuBi surface. The dotted circle indicates the "donut"-like defect radius. Panels (A) and (B), taken from the defect site, clearly show an additional peak near +200mV as compared to panel (C) which was taken from a "defect-free" location on the PtLuBi (001) surface.

This result indicates that the sub-surface crystallographic defect has an observable electronic state at +200mV. These spectroscopy results are consistent with imaging of the defects, where defects had pronounced donut-like shapes that were visible at +200mV, but only slightly visible at +5mV. A possible origin of this defect is Sb from the underlying PtLuSb (001) layer. In the growth of GaSbBi and InSbBi by molecular beam epitaxy, recent work has shown that the incorporation of Bi is difficult, and high Bi-Sb flux ratios must be used to incorporate Bi into the growing film [79]. This implies a stability of the Sb compound over the Bi compound, which could lead to the preferential formation of PtLuSb over PtLuBi, and some diffusion of the Sb from the PtLuSb into the

PtLuBi layer. This theory is also substantiated by the observation of Sb 3d peaks in XPS core level spectra of 10nm thick PtLuBi films on 8ML PtLuSb templates. An Sb substitution in the PtLuBi (001) film could lead to states near 200mV, similar to those observed in STS measurements of PtLuSb (001) films [44]. Additionally, STM/STS measurements of 20nm thick films show no observable defect states at 200mV tip-sample bias, suggesting that these defects are no longer present. It is possible that in thick films, the interfacial intermixing does not affect the surface of the film, and the presence of Sb at the surface is greatly reduced. To confirm these observations, further studies involving STM and STS measurements at varying thicknesses must be performed.

The observed LDOS features in the spectra taken from the defect free areas, which match those observed in thick PtLuBi films, match well with band structure calculations. A large peak in density of states at +1000mV can be attributed a sharp increase in density of states due to the flat character of the conduction band near the X point. The smaller feature near +500mV can be described by the semimetallic overlap of the valence and conduction band near Γ . From this analysis of LDOS features with respect to the Fermi level position of the free surface, it is believed that the Fermi level at the surface of these films lies approximately 500mV below the valence band maximum. This result is similar to that observed in PtLuSb and PtLuBi thin films and bulk crystals where transport, XPS, and STS measurements all indicate a Fermi level position

within the valence band [44, 66]. ARPES measurements of bulk PtLuBi crystals also suggest a similar Fermi level position, as determined by the extrapolation of linearly dispersing states in the valence band and measuring their predicted crossing point [80].

Unfortunately, due to the reactivity of PtLuSb with InSb, and the high temperature required to thermally desorb a Bi cap, ARPES measurements were not performed on PtLuBi (001) films. However, due to the inability to cap and decap the sample for transport to the synchrotron, an *in-situ* lab source x-ray photoemission spectrometer (XPS) was used to probe photoemitted electrons at binding energies corresponding to the valence band. XPS measurements used a monochromated Al-k lab source at $h\nu=1486\text{eV}$ with a fixed analyzer angle of 55° from sample normal. Figure 3.19 shows the comparison of XPS (A) measurements STS (B) spectra of taken from a defect-free area of the PtLuBi (001) surface.

Valence band features in the STS spectra at approximately -1800mV are also observed in XPS spectra. Additionally the continued decrease in photoemission intensity approaching the Fermi level is similar to the observed decrease in tunneling spectra. At higher binding energies, Lu $4f_{7/2}^7$ and $4f_{5/2}^5$ core levels are observed.

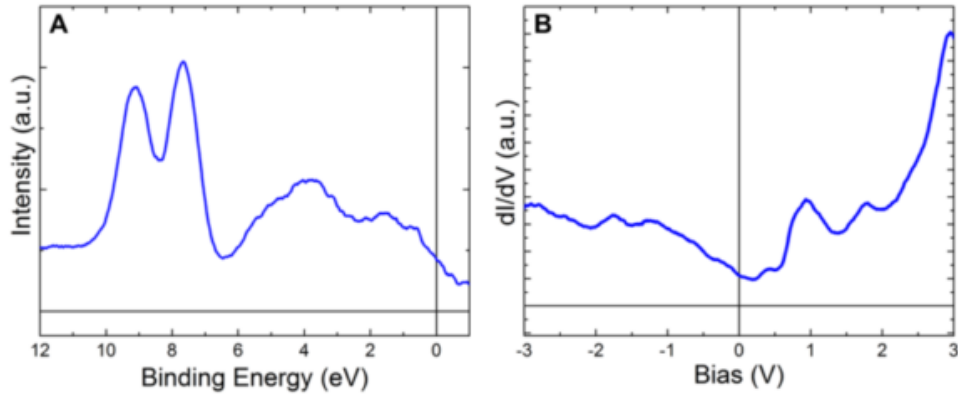


Figure 3.19. XPS measurements of the valence band (A) show similar DOS features as STS measurements (B) as evidenced by features near -1800mV in both spectra. The combination of the two measurements, plus theoretical density of states calculations suggest that the Fermi level is located 500mV below the valence band maximum in PtLuBi (001) films.

3.3.2 Summary

In this study, *in-situ* measurements of the valence band as well as STS spectroscopies were in good agreement to place the Fermi level position 500mV below the valence band maximum, which is similar to results of bulk crystals [80]. Unfortunately, an inability to cap and decap the grown films made it impossible to transport samples to the beamline at MAX-lab, so ARPES measurements were unable to be performed. This difficulty in capping, however, can be overcome by the development of a vacuum suitcase transfer to bring samples to a local synchrotron (Advanced Light Source at Lawrence Berkeley National Laboratory or SLAC National Accelerator Laboratory) in a van or truck without breaking vacuum and contaminating the sample surface. Plans for this type of transfer are underway at the time of the writing of this dissertation.

3.4 Outlook for topological half-Heusler thin films

The future is bright for the research of topological half-Heusler thin films. More and more research groups are starting to work on the materials, leading to better synthesis methods and eventually higher materials qualities. One important result of this research has been the determination of the Fermi level positions of both PtLuSb (001) and PtLuBi(001) thin films. The dramatic shift of the Fermi level into the valence band compared to theoretical predictions suggests that either the predictions were incorrect, or materials quality issues are affecting the band structure and Fermi level position. Fortunately, due to the great tunability of the Heusler compounds, it is possible to alloy and dope the materials to move the Fermi level position, as will be further discussed in the next chapter. To raise the Fermi level, which is accomplished by increasing the number of valence electrons per formula unit, alloying of Au onto the Pt site in both of these compounds could be used. This would potentially move the Fermi level position up towards the zero-gap point in PtLuSb or the conduction band in PtLuBi. Au is a suitable alloying material because its atomic number, Z , is only one unit higher than Pt, so the resulting change in crystal potential is unlikely to drastically affect band structure, but the extra electron it can donate can dramatically influence Fermi level position. If the Fermi level can be tuned to these positions, then the application of biaxial tensile strain can be used to open a bulk band gap at the energy levels that dominate transport. This promising

avenue of research can result in a better understanding of Heusler compound electronic structure and the knobs that can be used to adjust it.

Chapter 4

Full-Heusler/GaAs

Heterostructures for Spin

Injection

4.1 Introduction

The "holy grail" of semiconductor spintronics is the realization of the Datta-Das spin field effect transistor (spin-FET) proposed in 1990 [23]. Since the original proposal, however, creating an actual device has remained elusive, as it requires detailed understanding of how to put spins into a semiconductor, and an arguably more difficult task, manipulate them once they are inside. This chapter will not focus on spin transport within a semiconductor, but rather will detail work that has attempted to gain a better understanding of the design of

the spin injection contact to optimize and obtain control over spin injection.

The three important factors in determining spin injection efficiency from a ferromagnet into a semiconductor have already been discussed: the bulk spin polarization of the ferromagnet, the interfacial spin polarization of the ferromagnet/semiconductor interface, and the semiconductor band structure near the ferromagnet/semiconductor interface. To simply put spins into a semiconductor so that they can be manipulated requires a detailed understanding of each of these factors which can vary greatly for each materials system.

Fortunately for GaAs spintronics, nearly lattice-matched Fe contacts have served well as a source for spins, and there has been a great deal of work in optimization of the Fe/GaAs interface to improve spin injection efficiencies. However, Fe has a fundamental limit in how well it can serve as a spin source, which is its relatively low bulk spin polarization of 43% [26]. Fortunately, many full-Heusler compounds also have a very good lattice match to GaAs, including Co_2MnSi and Co_2FeSi . These two full-Heusler compounds also boast extremely high spin polarizations. Theoretically, both Co_2MnSi and Co_2FeSi are predicted to be 100% spin polarized in the majority direction [81, 82] as well as high curie temperatures of 985K and 1100K, respectively [4, 83], allowing them to retain their magnetic ordering at room temperature operation. However, when shifting from a simple elemental Fe ferromagnetic electrode to a complex ternary intermetallic one, the structural formation of the interface and structural ordering within the

ferromagnet come into play, and can play a large role in spin injection efficiency.

This chapter will be split into three major sections regarding spin injection from full-Heusler compounds into GaAs (001) lateral spin valve structures: Controlling the bulk spin polarization, understanding the interfacial spin polarization, and finally, understanding changes in the semiconductor band structure that occur due to reactions between the ferromagnet and GaAs. First, a short section will describe the growth of the full Heusler compounds by molecular beam epitaxy.

4.2 Growth of full Heusler compound Co_2MnSi and Co_2FeSi thin films by molecular beam epitaxy (MBE)

The growth of transition metals and transition metal complexes on GaAs (001) is tricky at elevated temperatures, as strong reactions tend to occur between the film and the substrate [70, 84–88]. Therefore during initial growths of Co_2MnSi on GaAs (001) a diffusion barrier was used which helped to allow for a study of a variety of growth temperatures that would result in the highest quality Co_2MnSi films. The diffusion barrier $\text{Sc}_{0.3}\text{Er}_{0.7}\text{As}$ with a rock-salt crystal structure was used due to its lattice-match with GaAs, and its effectiveness at preventing reactions between the underlying GaAs and transition metals [70].

This diffusion barrier layer was grown *in-situ* in the III-V MBE chamber and then transferred in UHV to the Heusler Gen II system where the full-Heusler compounds were grown.

A templated growth method was used where alternating monolayers of Co and MnSi were initially deposited on the $\text{Sc}_{0.3}\text{Er}_{0.7}\text{As}$ layers to promote the heteroepitaxial nucleation of Co_2MnSi . For growths on $\text{Sc}_{0.3}\text{Er}_{0.7}\text{As}$, Co was always chosen as the first full monolayer to deposit, and a 10ML seeded template was grown. The substrate temperature was held near 300°C for both the template growth and the subsequent codeposition of Co, Mn, and Si for the remainder of the film.

This resulted in the growth of very high quality Co_2MnSi films as verified by x-ray diffraction [Figure 4.1] and magnetic hysteresis loops measured in a Quantum Design MPMS system [Figure 4.2]. ω - 2θ diffraction scans show finite thickness fringes from the $\text{Sc}_{0.3}\text{Er}_{0.7}\text{As}$ layer, indicated by red arrows, as well as the Co_2MnSi layer, indicated by grey arrows, suggesting the growth of high quality, abrupt interfaces. Magnetic hysteresis measurements show an extremely low coercivity and high remanence magnetization at zero field.

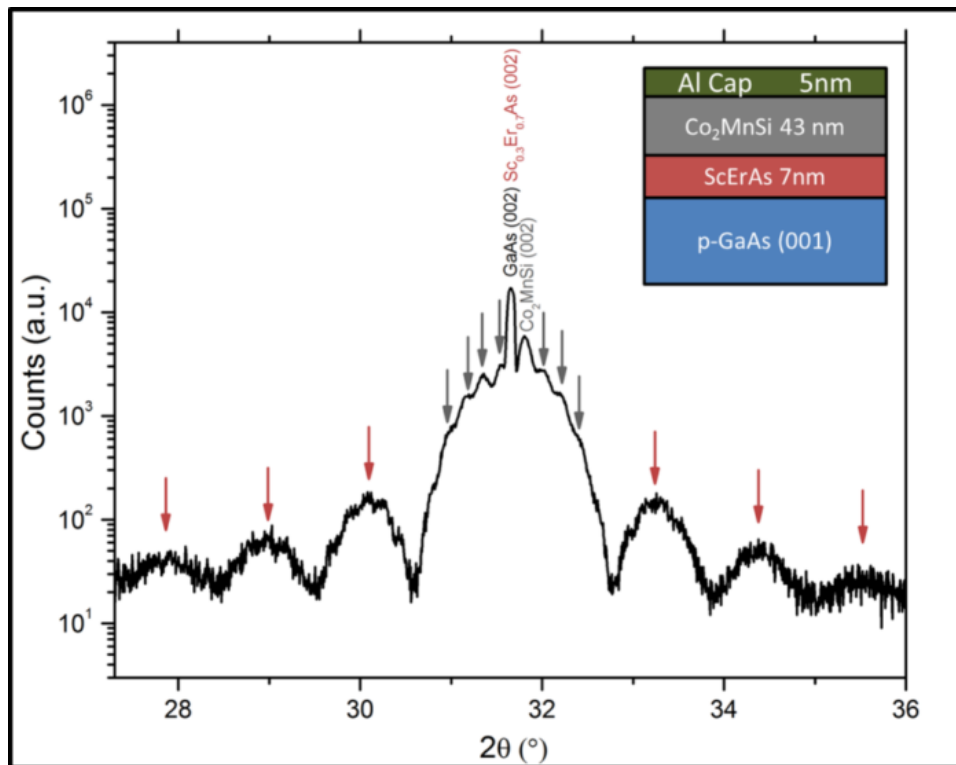


Figure 4.1. $\omega - 2\theta$ diffraction pattern around the GaAs (002) reflection of a Co_2MnSi film grown on $\text{Sc}_{0.3}\text{Er}_{0.7}\text{As}$ on GaAs (001). Inset is the sample structure. Arrows indicate finite thickness fringes from the $\text{Sc}_{0.3}\text{Er}_{0.7}\text{As}$ and Co_2MnSi layers suggesting the growth of high quality and abrupt interfaces.

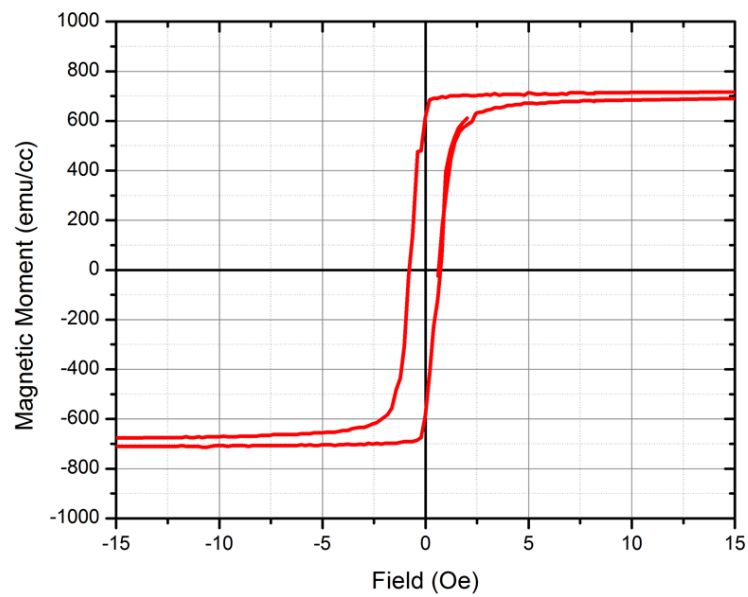


Figure 4.2. Magnetic hysteresis loop of Co_2MnSi grown on $\text{Sc}_{0.3}\text{Er}_{0.7}\text{As}$ measured at 300K in the $[110]$ direction. Due to the four-fold symmetry of the rocksalt crystal structure of the $\text{Sc}_{0.3}\text{Er}_{0.7}\text{As}$ layer, the film displayed four-fold magnetic anisotropy with easy axes in $\langle 110 \rangle$ directions.

After determination of the growth temperature of 300°C for Co₂MnSi on Sc_{0.3}Er_{0.7}As diffusion barriers, the Sc_{0.3}Er_{0.7}As was removed from the structure and Co₂MnSi was grown directly on GaAs (001) surfaces. At growth temperatures of 300°C, the films grew epitaxially, with RHEED intensity oscillations suggesting a layer-by-layer growth mechanism with a layer thickness of 0.5 unit cells.

The observation of RHEED oscillations at the expected rate based on beam flux calibrations helped to confirm the growth of stoichiometric crystals in a layer-by-layer growth mode, and was used in future growths as a metric for the verification of stoichiometric growth. The RHEED pattern observed after the growth of a thick Co₂MnSi film and the corresponding RHEED intensity oscillations are shown in figure 4.3.

The magnetic behavior of thin (<5nm) Co₂MnSi is quite different than its behavior on Sc_{0.3}Er_{0.7}As. This is due to the strong interfacial anisotropy induced by the two-fold symmetric GaAs surface. Similar to the behavior of Fe and other elemental ferromagnets, in thin layers, this anisotropy creates an easy axis in the [110] direction and a hard axis in the [1 $\bar{1}$ 0] direction [89].

The magnetic hysteresis loops of a 5nm thick Co₂MnSi film grown on GaAs in three high-symmetry directions are shown in figure 4.4. These results are of particular importance as lateral spin valve devices need to be fabricated with ferromagnetic contact stripes along the easy access so that magnetizations can be

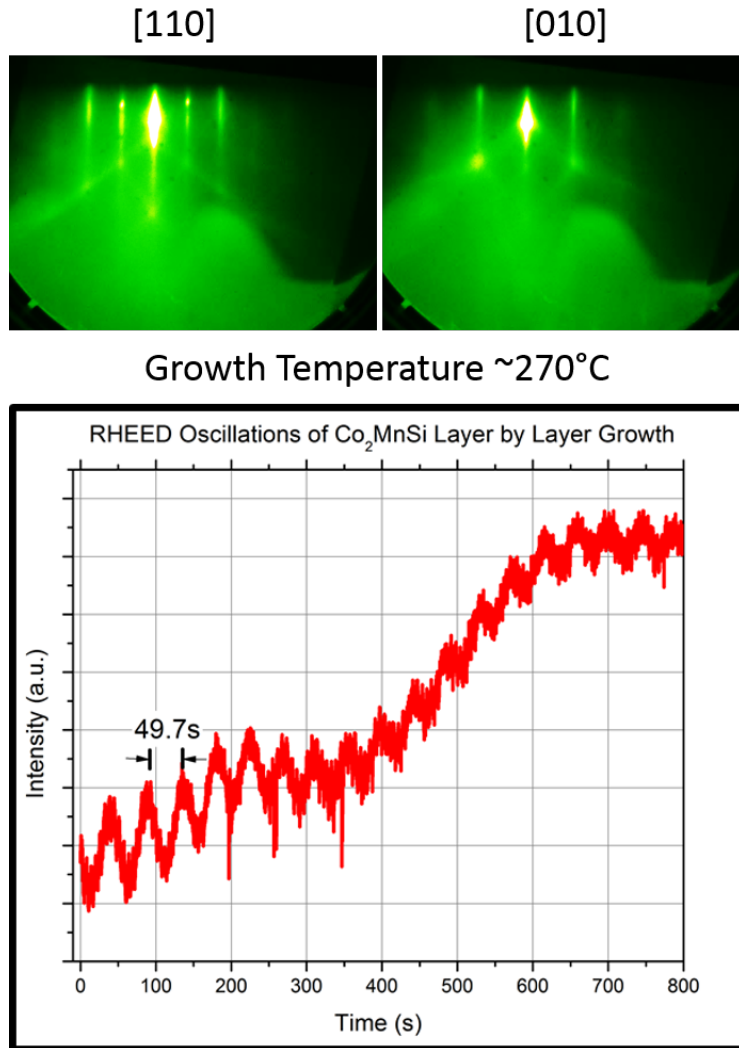


Figure 4.3. Top: RHEED patterns of 5nm thick Co₂MnSi grown on GaAs (001) at 270°C. Bottom: RHEED intensity oscillations with a period of 49.7s which agrees well with the expected growth rate from flux calibrations.

accurately controlled during device measurements. During device measurements, an in-plane field parallel to the [110] direction is used to control the magnetization of ferromagnetic contacts, and upon removal of the field, since the easy axis of the film is in the [110] direction, the contact will retain its magnetization, allowing for precise control of contact magnetizations.

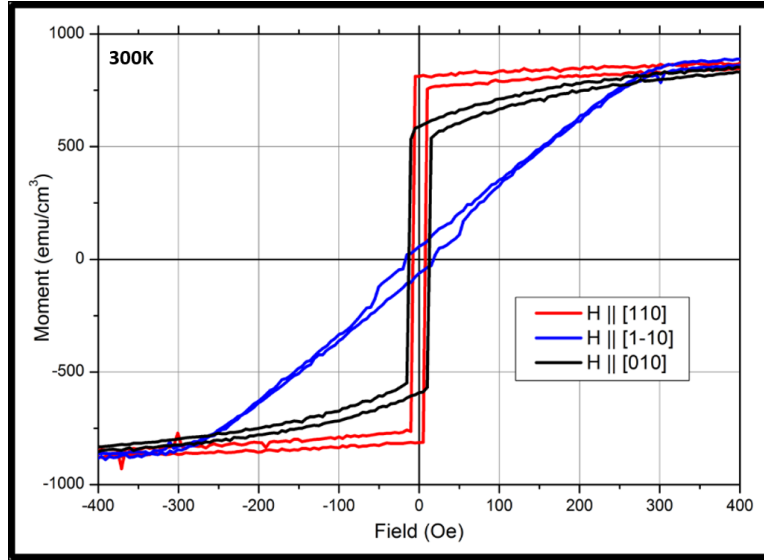


Figure 4.4. Hysteresis loops of a 5nm Co_2MnSi film grown directly on GaAs (001) taken with field applied and magnetization measured in the $[1\bar{1}0]$, $[110]$, and $[010]$ directions. The 2-fold surface symmetry of GaAs (001), combined with the thin film geometry, induces a strong uniaxial magnetic anisotropy on the Co_2MnSi films with an easy axis in the $[110]$ direction.

Figure 4.5 shows an *in-situ* topographical STM image of a 4nm thick Co_2MnSi grown directly on GaAs (001). The surface shows step heights of 2.8\AA , which corresponds to 0.5 Co_2MnSi unit cells, matching well with RHEED oscillations occurring at a period corresponding to the growth of one-half unit cell. The surface is as smooth as the GaAs (001) surface underneath, and retains the typical terrace elongation in the $[1\bar{1}0]$ of GaAs (001) surfaces.

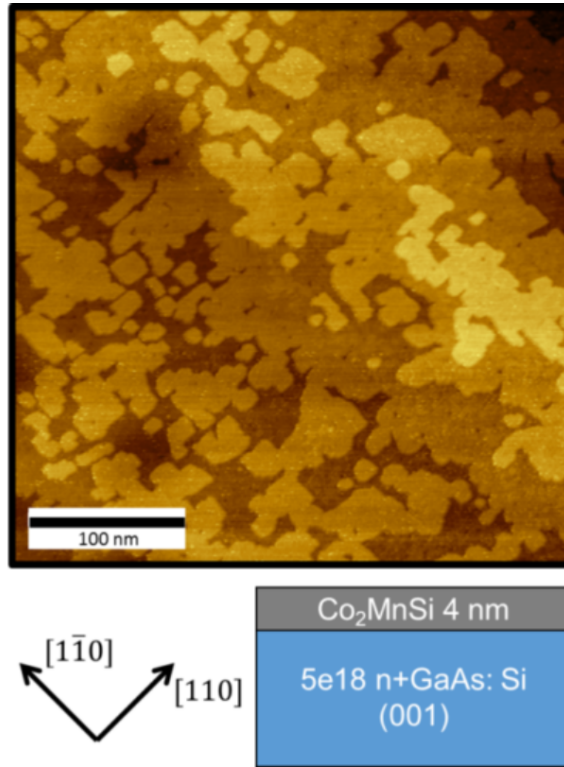


Figure 4.5. STM image of a 4nm thick Co_2MnSi film grown on GaAs (001). Step heights correspond to 1 bilayer of Co_2MnSi (2.8\AA).

4.2.1 Growth of Heusler/GaAs (001) layers for lateral spin valve heterostructures

Shown in figure 2.9 is the schematic diagram of III-V layers grown for lateral spin valve device stacks. This III-V stack consists of a lightly doped $n\text{GaAs}$ channel capped with a graded doping to a highly doped region to create a narrow Shottky barrier. These epilayers were grown in the III-V VG-V80H MBE system, then terminated with an As-rich $c(4\times 4)$ surface reconstruction for Heusler growth [63]. The $c(4\times 4)$ reconstruction was chosen because it is the most reproducibly attained in terms of cooling procedures after III-V growth. For all of the lateral

spin valve samples, a Heusler thickness of 5nm was grown. After the sample was allowed to cool to room temperature, a 10nm Al cap was grown followed by an additional 10nm of Au to protect the ferromagnetic film from oxidation.

Using these growth techniques, we were able to demonstrate spin injection directly from Co_2MnSi thin films into GaAs for the first time. The spin signals were observed in a lateral spin valve measurement and verified by the observation of spin dephasing in Hanle measurements as shown in figure 4.6. For this measurement, and all future measurements in this dissertation, the biased detector geometry was used for spin signal measurements with a forward bias of 2mA on the detector.

An ideal growth temperature of Co_2MnSi on GaAs (001) of 270°C was determined by lateral spin valve measurements [Fig. 4.7]. A series of samples were grown at different growth temperatures and their spin injection/detection efficiency was studied.

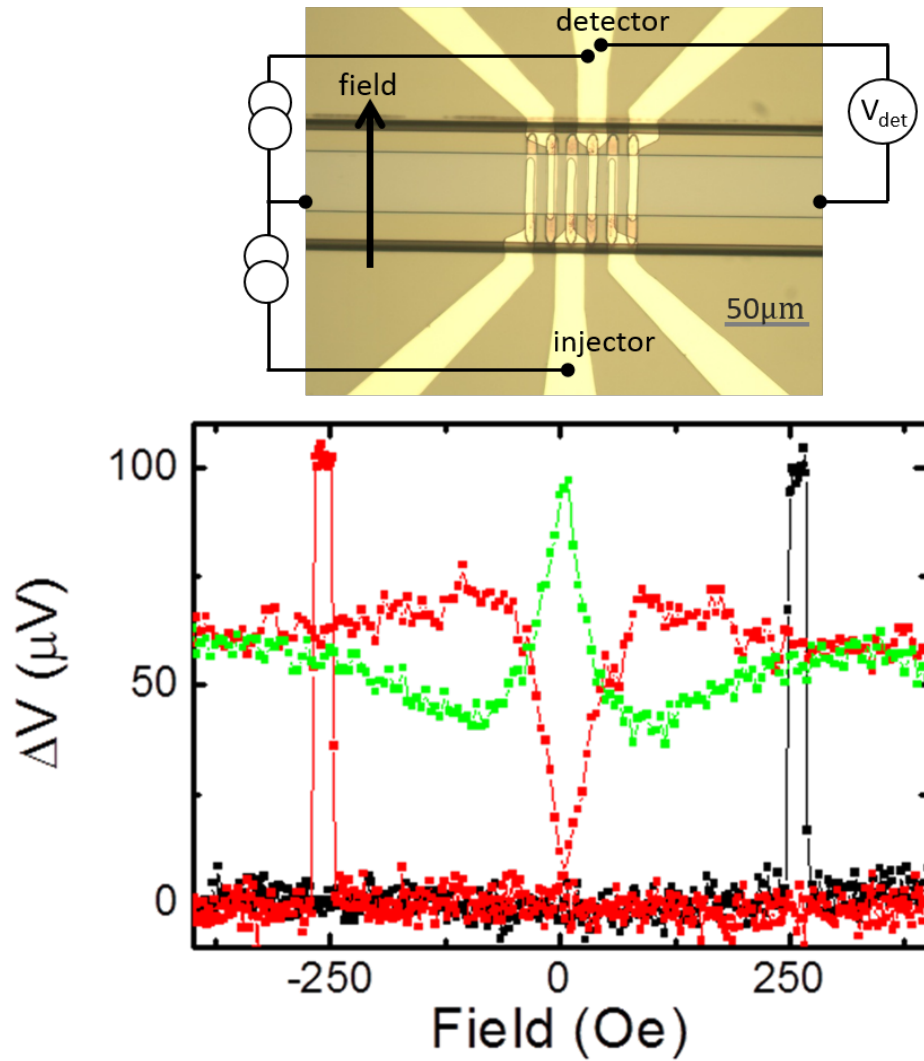


Figure 4.6. Spin valve signal at 60K shown in black as well as Hanle curves shown in red and green for a $\text{Co}_2\text{MnSi}/\text{GaAs}$ (001) lateral spin valve. The measurements were taken in a biased detector geometry as shown in the optical micrograph of the fabricated device.

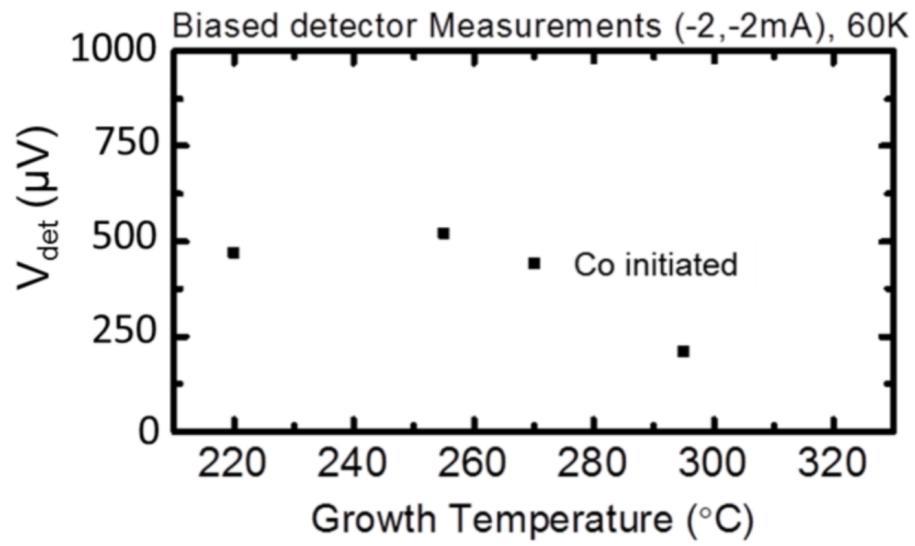


Figure 4.7. Growth temperature dependence of the non-local spin valve signal in $\text{Co}_2\text{MnSi}/\text{GaAs}(001)$ heterostructures. An ideal growth temperature of 270°C was determined by finding the maximum of the spin signal.

The measured spin signal in these devices peaked at a growth temperature of around 270°C with a significant decrease in spin signal above these growth temperatures. Therefore, all future samples were grown at a substrate temperature of 270°C.

For the best sample, we were able to obtain spin signals in excess of 2mV at room temperature, which is a 20x improvement over typical Fe/GaAs samples [see Fig. 4.8]. By modeling the spin injection efficiency and the enhancement due to detector bias, Paul Crowell's group at University of Minnesota was able to calculate a spin accumulation near 60% in the GaAs channel, as compared to typical values of 30% in Fe/GaAs devices. This near doubling of injected spin

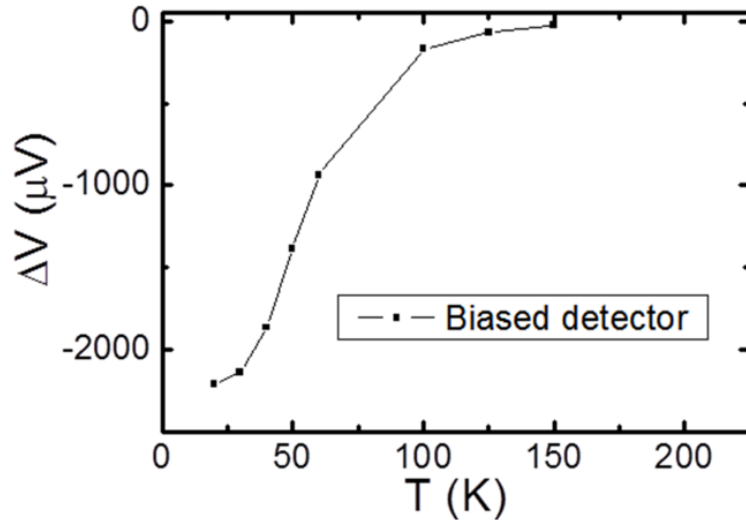


Figure 4.8. Temperature dependence of the spin signal with a detector and injector bias of 2mA (forward) in a $\text{Co}_2\text{MnSi}/\text{GaAs}$ (001) spin valve. This sample shows a tremendous spin signal in excess of 2mV at 30K.

polarization is attributed to the high spin polarization of the bulk Co_2MnSi film,

as well as a high interfacial spin polarization. These initial results showed the promise of highly spin polarized compounds, and the work in the rest of this chapter set out to control the magnitude and sign of the spin signals, as well to understand the Heusler/III-V interface.

4.3 $\text{Co}_2\text{Fe}_x\text{Mn}_{1-x}\text{Si}$ alloys: Controlling the bulk spin polarization

The two compounds Co_2MnSi and Co_2FeSi are nearly ideal choices for spin injection into GaAs. Their lattice constants are nearly identical at 5.65\AA , and are almost perfectly lattice-matched to GaAs ($< -0.6\%$ mismatch) [81, 82]. Additionally, their crystal structure is well suited towards epitaxial growth on GaAs as they retain the similar face-centered cubic sublattice structure of the Ga and As in the zinc blende structure. Both compounds also have high Curie temperatures of 985K for Co_2MnSi and 1100K for Co_2FeSi making them suitable for room temperature operation [4, 83]. Both of these materials also have very high spin polarizations, with Co_2MnSi predicted to be 100% spin polarized in the majority direction [82]. Co_2FeSi has been predicted to be both half-metallic with a majority spin polarization [90], and near half metallic with a spin polarization in the minority direction [91]. Experiments have suggested that Co_2FeSi is indeed minority spin polarized both by a sign reversal in anisotropic magnetoresistance

measurements [92] as well as an increase in Gilbert damping parameter, α , as compared to half-metallic films [38]. For the purposes of this experiment, these experimental studies are assumed to be correct, and pure Co_2FeSi is minority spin polarized.

Co_2MnSi and Co_2FeSi possess a valence electron count of 29 and 30 e^- per formula unit. The addition of one more valence electron results in a “higher” filling of electrons within the band structure, therefore raising the Fermi level. As shown in figure 4.10, the two compounds have electronic structures with similar density of states for each spin channel, but the Fermi level position is raised in the Co_2FeSi as compared to the Co_2MnSi . This suggests that by increasing the Fe content in the alloy $\text{Co}_2\text{Fe}_x\text{Mn}_{1-x}\text{Si}$ should raise the Fermi level to a point where the compound becomes minority spin polarized. If this is the case, then the alloying of Fe on the Mn site could prove to be a useful tool in tuning both the magnitude and sign of spin polarization.

To complement experimental results that suggest that $\text{Co}_2\text{Fe}_x\text{Mn}_{1-x}\text{Si}$ alloys become minority spin polarized at high Fe contents, we chose to study the spin injection from these alloys as a function of Fe content, x , into GaAs (001) spin channels. From previous lateral spin valve measurements using Fe spin injectors into GaAs, it has been determined that the sign of the spin accumulation in the GaAs is the same as the sign of the spin in the ferromagnetic contact, so this system allows for the measurement of not only magnitude of injected spin

polarization, but also for the measurement of sign of that spin polarization [58].

4.3.1 Growth of $\text{Co}_2\text{Fe}_x\text{Mn}_{1-x}\text{Si}$ alloys

To grow the $\text{Co}_2\text{Fe}_x\text{Mn}_{1-x}\text{Si}$ thin film alloys, a shuttered growth technique as was used for PtLuSb, PtLuBi, and Co_2MnSi could not be used. This is because the Co and Fe sources are part of a dual-source cell in the Heusler Gen II, which means that both fluxes are shuttered simultaneously by a single shutter, making it impossible to grow one versus the other. Since the seeded nucleation sequence was not possible for $\text{Co}_2\text{Fe}_x\text{Mn}_{1-x}\text{Si}$ alloys, a full series of compositions with $x = 0, 0.3, 0.33, 0.66, \text{ and } 1$ were grown using codeposition of Co, Fe, Mn, and Si from the start of the growth. The samples $x = 0, 0.33, 0.66, \text{ and } 1$ were all grown as a series, in immediate succession without changing the Co or Si source temperatures so as to eliminate any experimental variable changes aside from the Fe/Mn ratio.

4.3.2 Biased detector spin signal measurements of $\text{Co}_2\text{Fe}_x\text{Mn}_{1-x}\text{Si}/\text{GaAs}$ (001) spin valves

For measurements of spin signal in $\text{Co}_2\text{Fe}_x\text{Mn}_{1-x}\text{Si}/\text{GaAs}$ (001) spin valves, a constant injector and detector bias of 2mA (in the forward bias condition) were used. Even though the pure Co_2FeSi sample contained no Mn, and the detector was “on” at no bias, the sample was still measured under bias to be

able to compare the magnitude and sign of the spin signals.

The biased detector spin signals for each sample, measured at 30K, are shown in figure 4.9.

It is clearly observed that the spin signal first decreases as x is increased until it reaches a point at $x \approx 0.66$ where the spin signal is nearly 0, then flips sign and increases in the minority direction as x approaches 1. Using predicted band structures, a schematic diagram can be drawn that describes the transition, where at $x = 0.66$, the number of majority and minority states at the Fermi level are nearly equal, with the end results being an injection of an unpolarized spin current and the measurement of no spin voltage [Figure 4.10].

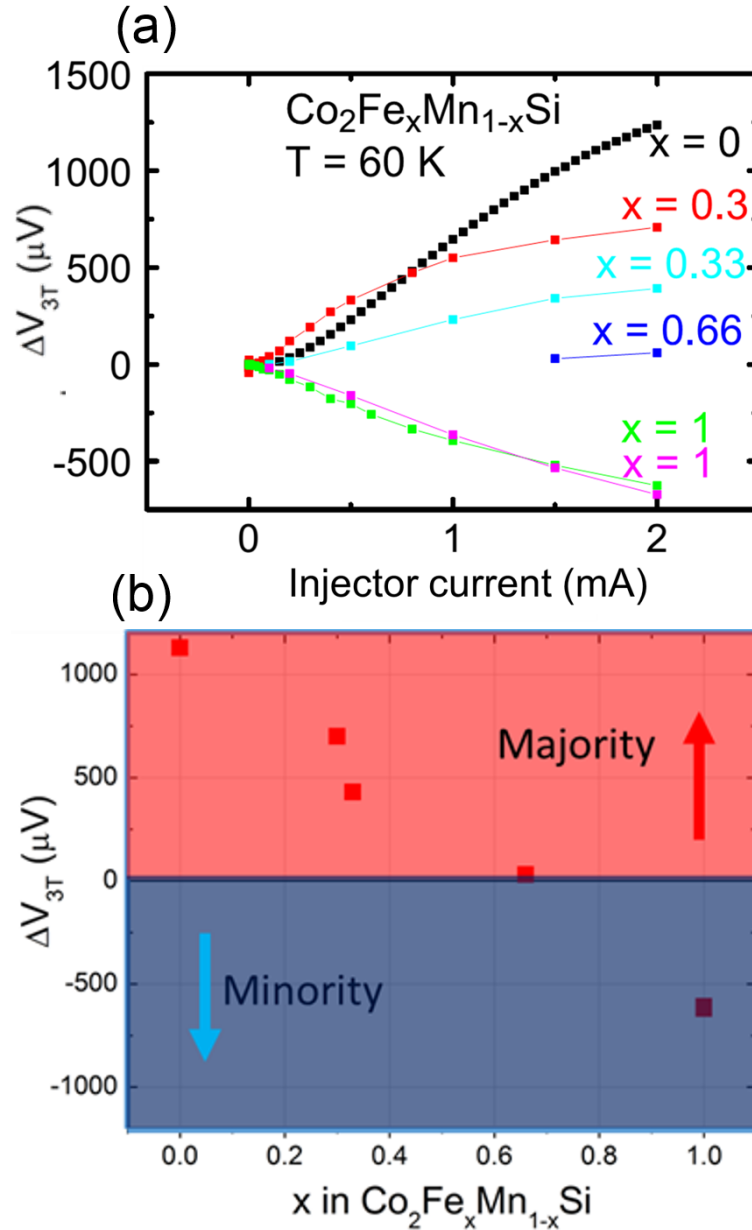


Figure 4.9. (a) Raw measurement of spin signal as a function of injector bias. (b) The biased detector spin signal as a function of concentration, x , of Fe in $\text{Co}_2\text{Fe}_x\text{Mn}_{1-x}\text{Si}$. Shaded in red is a region where the ferromagnet's spin polarization is majority, while the blue section and negative values show minority spin polarization. A clear crossover from majority to minority spin polarization at $x \approx 0.66$ is clearly observed in the $\text{Co}_2\text{Fe}_x\text{Mn}_{1-x}\text{Si}$ alloy.

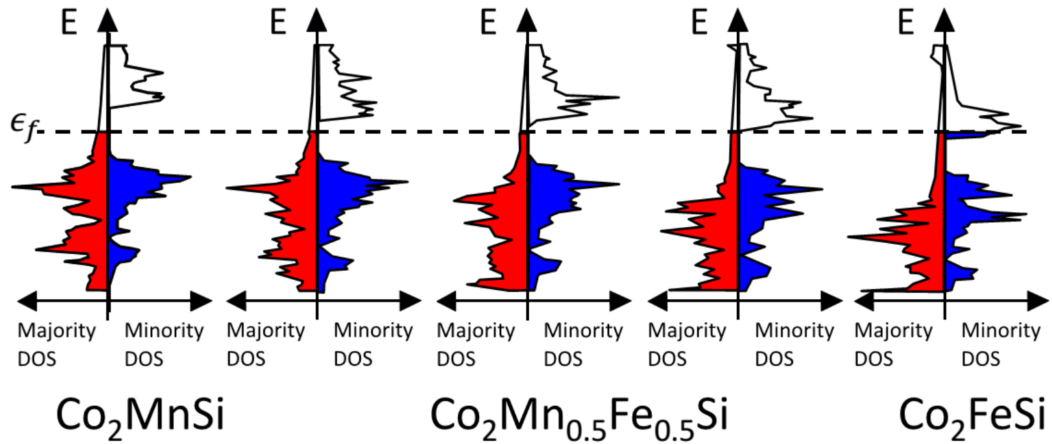


Figure 4.10. The density of states of $\text{Co}_2\text{Fe}_x\text{Mn}_{1-x}\text{Si}$ as x varies from 0 to 1. This figure was adapted by Kevin Christie from Ref. [81].

This apparent change in spin polarization, and the decrease in spin signal observed for $\text{Co}_2\text{Fe}_x\text{Mn}_{1-x}\text{Si}$ alloys with $0 < x < 1$, shows not only the opposite nature of the spin polarizations of Co_2MnSi and Co_2FeSi , but also the compositions in between where the spin polarization can be modified by alloying.

The ability to tune the spin polarization magnitude and sign by controllable alloying is a new concept to the field of semiconductor spintronics. Previous work has focused on efforts to increase injected spin polarization as well as increase overall spin signal in lateral semiconductor devices. Our work has demonstrated not only very high spin signals using Heusler compounds, but has been able to demonstrate control over magnitude and sign of spin polarization in the GaAs channel.

This study also shows the versatility of the whole class of Heusler compounds, as the Fermi level can be tuned through a band gap (in this case the minority spin

gap) by alloying with an element that increases the total valence electron count per formula unit. In future work, these concepts will be applied to modify the Fermi level position of the proposed topologically non-trivial Heusler compound PtLuSb, mentioned in chapter 3, by alloying on the Pt site with Au. Additionally, in work to be completed by Sean Harrington in our research group, we will investigate the Fermi level shift in purely semiconducting compounds and try to understand the semiconducting to metallic transition in $\text{Co}_{1-x}\text{Ni}_x\text{TiSb}$ compounds.

4.4 Understanding the effect of the $\text{Co}_2\text{MnSi}/\text{GaAs}$ (001) interface on spin injection

While theoretical predictions suggest that Co_2MnSi is half-metallic [82], a practical limitation of the spin polarization is often reached due to the breakdown of half-metallicity at surfaces and interfaces [39, 93–96]. Understanding the band structure at these interfaces, therefore, is of utmost importance when predicting and understanding device performance. In the case of $\text{Co}_2\text{MnSi}/\text{GaAs}$ (001) interfaces, the bonding and structure can be extraordinarily complex. This study attempted to modify the interfacial structure by a modification of the film nucleation, and see if changes in interfacial structure resulted in changes in the spin injection in $\text{Co}_2\text{MnSi}/\text{GaAs}$ lateral spin valves. However, the end result, presented in the following sections, was that the interfacial structure could not be modified.

4.4.1 Co- and MnSi- Initiated $\text{Co}_2\text{MnSi}/\text{GaAs}$ (001) Lateral Spin Valve Heterostructures

The $L2_1$ full-Heusler crystal structure consists of alternating planes of Co and MnSi. Therefore, using the epitaxial seeding layer technique, previously described for PtLuSb and PtLuBi growth, there are two choices for the initiation layer, Co or MnSi. To see if the choice of initiation layer would affect the spin

signal by modification of interfacial structure, two samples were grown: one with a Co initiation layer and one with a MnSi initiation layer. Regardless of initiation layer, the resulting structural quality and magnetic properties of the films remained the same, suggesting that the choice of initiation layer did not have a significant effect on the epitaxial growth or the bulk structure of the film.

Shown in figure 4.11 are RHEED diffraction patterns from the growth of both samples taken in the $[1\bar{1}0]$ direction as a function of growth thickness. After the growth of the second monolayer, no significant differences in RHEED are observed for either sample, and the only difference observed is after the growth of the initiation layer. For the Co initiation layer, faint streaks are observed at positions around the spectral beam that do not index to lattice parameters from reflections of the full Heusler crystal structure. These streaks may originate from the formation of a CoAs like phase which has been suggested to form after the deposition of $< 1\text{ML}$ Co on the $c(4\times 4)$ GaAs (001) surface [84]. After subsequent MnSi deposition, these faint streaks disappear and RHEED patterns representative of Co_2MnSi appear.

For MnSi initiated films, the $c(4\times 4)$ reconstruction of the GaAs (001) surface disappears, and reflections from the bulk GaAs dim considerably. After the deposition of the next Co layer, RHEED patterns representative of Co_2MnSi appear, suggesting the formation of a 2 monolayer thick film of Co_2MnSi .

After the growth of a few monolayers, both samples display $\frac{1}{2}$ order streaks

corresponding to a real space $2\times$ surface periodicity as compared to the bulk unit cell. As will be shown later, these RHEED patterns are consistent with a mixed $c(2\times 4)/c(4\times 2)$ surface reconstruction believed to originate from GaAs that is riding on top of the Co_2MnSi film.

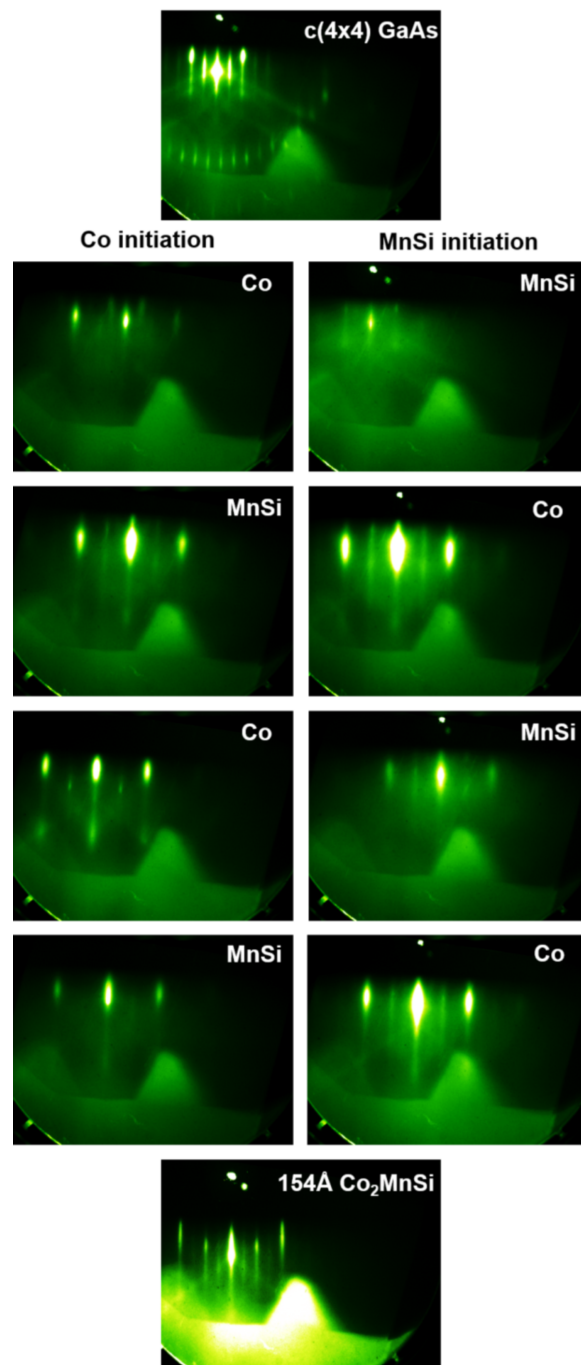


Figure 4.11. RHEED of a starting $c(4 \times 4)$ GaAs (001) surface as well as after the deposition of each monolayer in Co- and MnSi-initiated samples of Co_2MnSi . After the deposition of the first monolayer, there are no significant differences in RHEED, and after deposition of 15.4nm of film, the RHEED patterns are nearly identical, showing a slight 2x periodicity in both the $[110]$ and $[\bar{1}\bar{1}0]$ directions.

4.4.2 Spin signals of Co- and MnSi- initiated $\text{Co}_2\text{MnSi}/\text{GaAs}$ (001) non-local spin valves

After growth of the full lateral spin valve heterostructure for both Co- and MnSi-initiated Co_2MnSi films, the samples were then fabricated into non-local spin valve devices as shown in figure 2.11 for spin transport measurements. Shown in figure 4.12 are positive field non-local spin-valve measurements with a 2mA detector bias (to increase detection efficiency) of $\text{Co}_2\text{MnSi}/\text{GaAs}$ (001) Co- and MnSi- initiated samples.

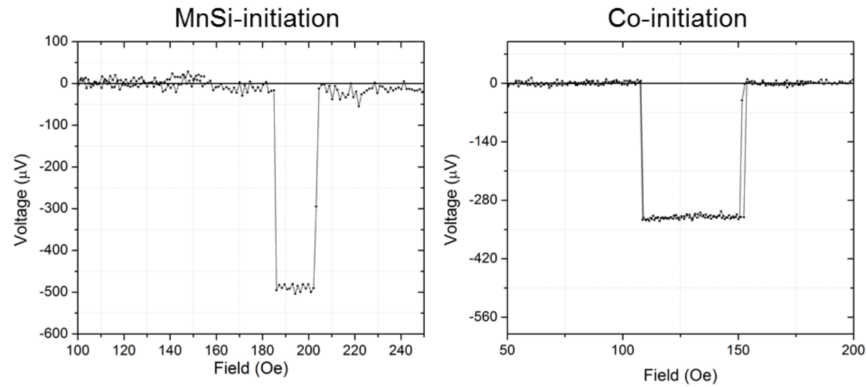


Figure 4.12. Non-local spin valve signals for Co- and MnSi-initiated $\text{Co}_2\text{MnSi}/\text{GaAs}$ (001) lateral spin valve structures. The observed spin signals are fairly similar.

The jumps in voltage are observed when the extraction contact is magnetically oriented in an antiparallel direction to the detection contact. The spin signal for the MnSi initiated device is similar to that of the Co initiated device ($500\mu\text{V}$ vs $375\mu\text{V}$), but there is an increase in noise on the spin-signal in the MnSi initiated sample as compared to the Co sample. The increase in noise suggests that the choice of nucleation sequence affects the spin injection process

from the ferromagnet into the GaAs channel. Since the bulk of the Co_2MnSi , as verified by RHEED during growth and transmission electron microscopy after growth, remains the same regardless of nucleation sequence, a change in bulk electronic structure of the ferromagnet can be ruled out. The change in spin injection properties, therefore, must be due to a modification of either the interfacial electronic structure or the semiconductor electronic structure. First, the interfacial structure was studied during growth by *in-situ* scanning tunneling microscopy and spectroscopy (STM/STS) and XPS as well as *ex-situ* by high angle annular dark field scanning transmission electron microscopy (HAADF-STEM) combined with electron energy loss spectroscopy (EELS) maps of the interfacial region.

4.4.3 *In-situ* STM and STS of Co_2MnSi growth on $c(4\times 4)$ GaAs (001) surfaces

The *in-situ* scanning tunneling microscope provides an ideal tool to study the heteroepitaxial nucleation of Co_2MnSi on GaAs (001) as it allows for both a topographical study of the nucleation as well as a study of the electronic structure of ultra-thin Co_2MnSi films by means of STS. For these experiments, STM/STS measurements were performed at 78K in an Omicron low temperature scanning probe microscope (LTSPM) to reduce the effects of piezoelectric drift during STS measurements and to reduce the effects of surface atom diffusion.

Tunneling spectroscopy measurements were used to study the local density of states (LDOS) by measuring differential conductance as a function of tip-sample bias using standard lock-in techniques. STS measurements were performed using a varied-Z spectroscopy mode where the tip-sample distance is linearly scaled with the magnitude of the applied bias. This measurement technique allowed for accurate measurement of semiconducting band edges as well as a high sensitivity to states close to the Fermi level as described by Feenstra [77, 78]. Spectra were normalized by I/V using previously published techniques in order to remove the effects of the change in conductance caused by ramping the tip closer to and further from the surface [77, 78]. In this study, for both Co- and MnSi-initiated samples, the STM was used to investigate surface topography as well as surface electronic structure during nucleation after each monolayer of growth. The results from the MnSi-initiated sample will be discussed first, followed by the results of the Co-initiated sample.

The GaAs $c(4 \times 4)$ surface reconstruction consists of triplets of As-As dimers along the $[110]$ direction bonded to an underlying As layer as shown in figure 4.13 [63].

This results in an extra 0.75ML of surface As on the nominally stoichiometric GaAs substrate. An STM image of the $c(4 \times 4)$ surface is included in figure 4.14.

After deposition of 1ML MnSi, STM images show that the $c(4 \times 4)$ reconstruction of GaAs is completely destroyed. However, GaAs terraces are still observed,

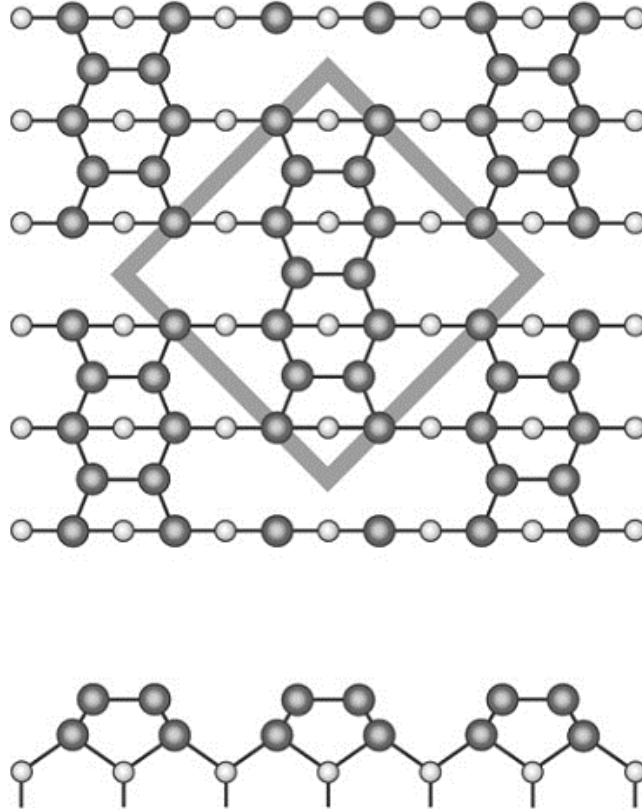


Figure 4.13. A schematic of the β -c(4x4) surface reconstruction showing both top down and side (along the $[1\bar{1}0]$ direction) views. The reconstruction results in an extra 0.75ML of As on the surface. This figure was taken from Ref. [63].

and approximately 4\AA tall islands cover $\approx 25\%$ of the surface. STS spectra at all areas of the surface suggest a gapped electronic structure, with a slightly different LDOS from spectra taken from the 4\AA tall islands [Fig. 4.15].

From STS spectra shown in figure 4.15, it appears as though STS spectra from the lower areas of each terrace are gapped, and that spectra on top of each island show similar STS spectra, with a gap present, convoluted with the existence of a smaller gap. From previous studies of Mn deposition on c(4x4) GaAs (001) surface, the areas in between the islands look nearly identical to the

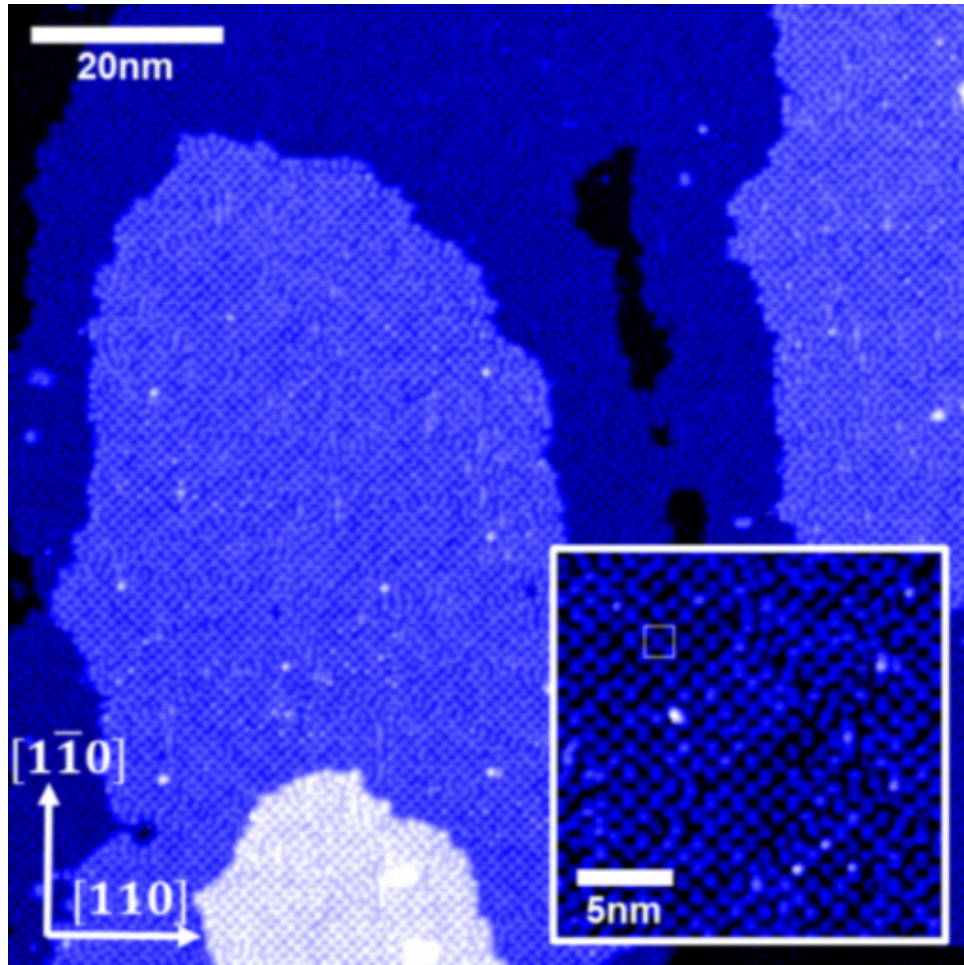


Figure 4.14. STM filled state images of $c(4 \times 4)$ GaAs surface. The inset shows a zoomed in view, with a highlight of the $c(4 \times 4)$ unit cell. Some disorder in the surface reconstruction is clearly observed, likely caused by As-deficiencies due to post-growth annealing procedures used to reduce excess As from sticking to the surface.

surfaces where pure Mn was deposited at similar growth temperatures of 250°C , where it is theorized that Mn reacts with the GaAs to form Mn_2As and $\delta\text{-MnGa}$ like phases [87]. Studies of the growth of Si on GaAs (001) surface suggest that Si sits on the GaAs surface to form rectangular islands [97]. The smaller observed gap (green dotted line) of the island like features suggests that these islands could be the formation of silicon with GaAs on top or directly beneath,

since the GaAs band-gap features still seem to be present (red dotted lines). Unfortunately, using STS, it is difficult to draw solid conclusions on band gap size from layer to layer, as factors that can affect tip-induced band bending can change [48].

After the deposition of the next ML, Co, the sample surface morphology changes dramatically, with the growth of islands over the whole surface (> 85% coverage) with clear $\langle 110 \rangle$ type faceting, typical of the Heusler compounds studied in this dissertation [Figure 4.16].

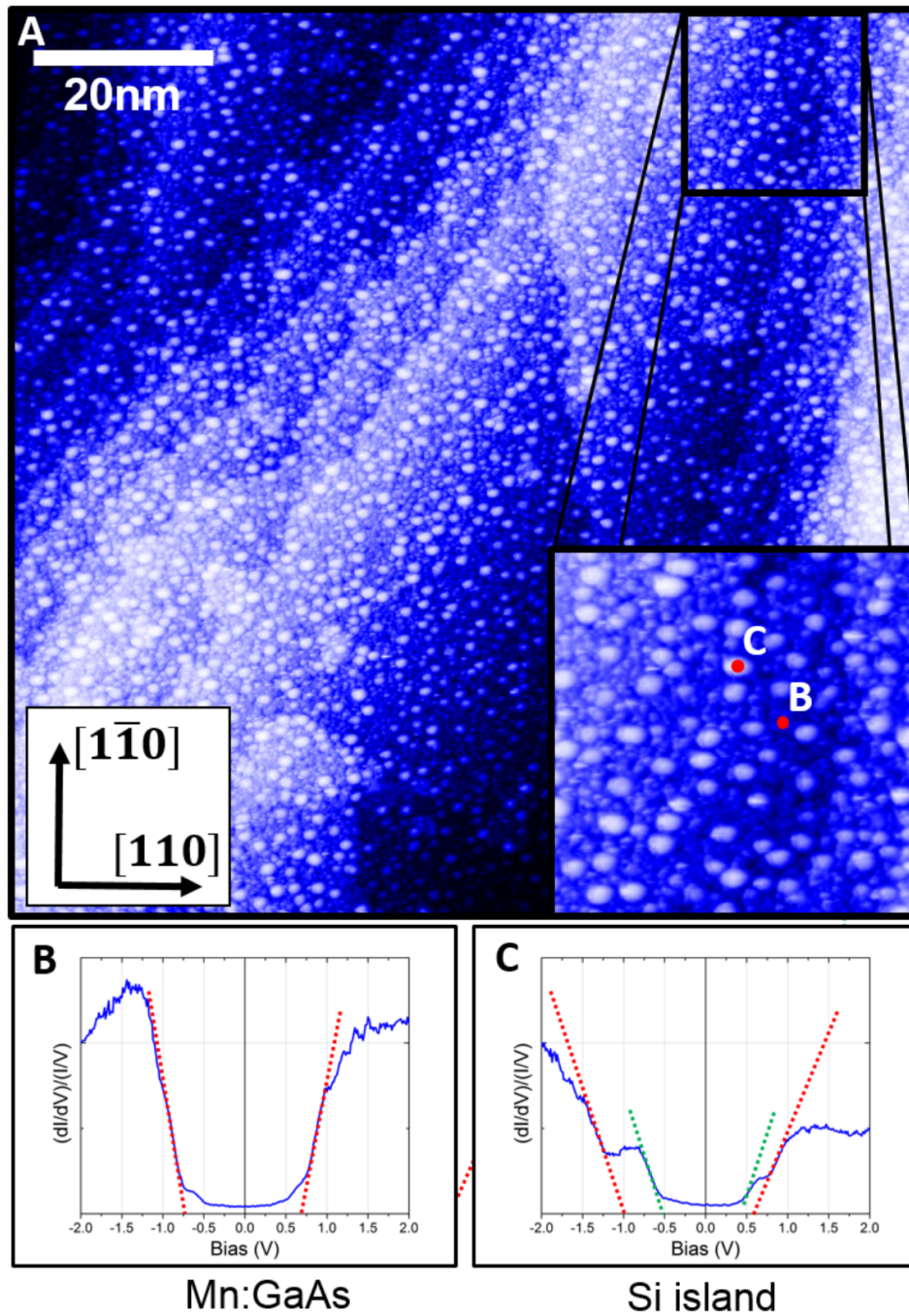


Figure 4.15. STM filled state images of GaAs surface after the deposition of 1ML MnSi. The $c(4 \times 4)$ surface reconstruction appears to be destroyed and the surface is 25% covered in 4 Å tall islands. Also shown are STS spectra taken on the areas where the reconstruction is destroyed (left) and on the islands (right) where the LDOS is modified.

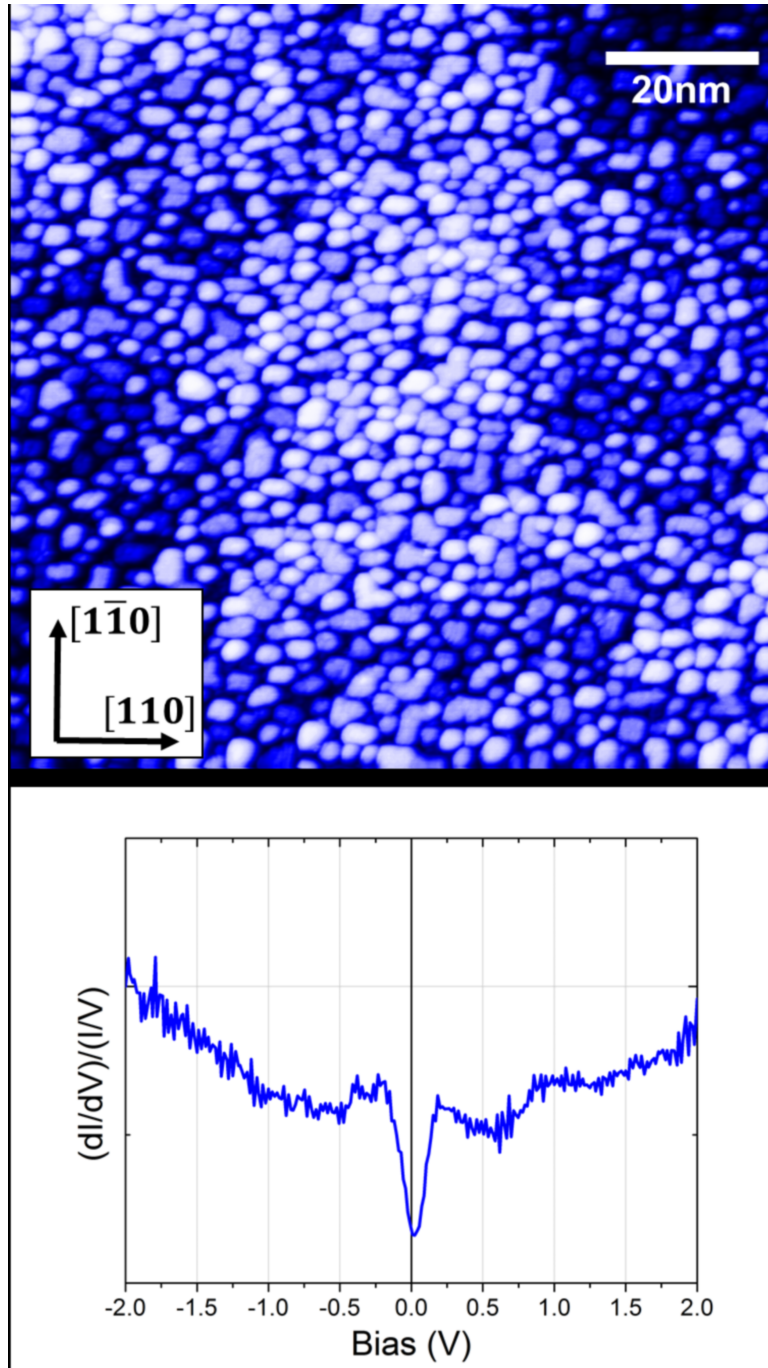


Figure 4.16. An STM image (top) and STS spectra (bottom) of a 2ML thick MnSi-initiated sample after the deposition of the first Co ML. STS spectra suggest a metallic surface and resemble the LDOS measured on thick Co_2MnSi films. $\langle 110 \rangle$ type faceting is observed in the STM image, which is typical of Heusler compounds.

STS measurements also show that the band gap is no longer present, and a LDOS representative of metallic surfaces is observed. The STS spectra for the 2ML thick sample are similar to those observed for thick Co_2MnSi films, suggesting that the full-Heusler crystal structure is present in this 2ML thick film.

For samples initiated with Co, STM images show very different surfaces for the initial monolayer of deposition, but after the second monolayer, both samples appear nearly identical [Figure 4.17]. After the deposition of 1ML of Co on the $c(4\times 4)$ GaAs (001) surface, STM images show the presence of small, densely packed islands. Clear $\langle 110 \rangle$ faceting is observed. At this point, STS spectra suggest a metallic surface, which is presumably a CoAs or CoGa phase, similar to those reported for the deposition of pure Co on $c(4\times 4)$ GaAs at elevated temperatures [84].

After deposition of the next ML of MnSi, no significant changes to the surface morphology are observed, except for a slight increase of $\langle 110 \rangle$ faceting. STS spectra taken on the island appear metallic, and show a density of states similar to that of bulk Co_2MnSi [Figure 4.18]. Also shown in the bottom of figure 4.18 is the evolution of STS spectra along the red line traveling from the semiconducting surface to the top of a Co_2MnSi island. The transition from a semiconducting spectra in between the islands to a metallic spectra on top of the islands is clear. It is important to note the presence of LDOS features (indicated by black arrows)

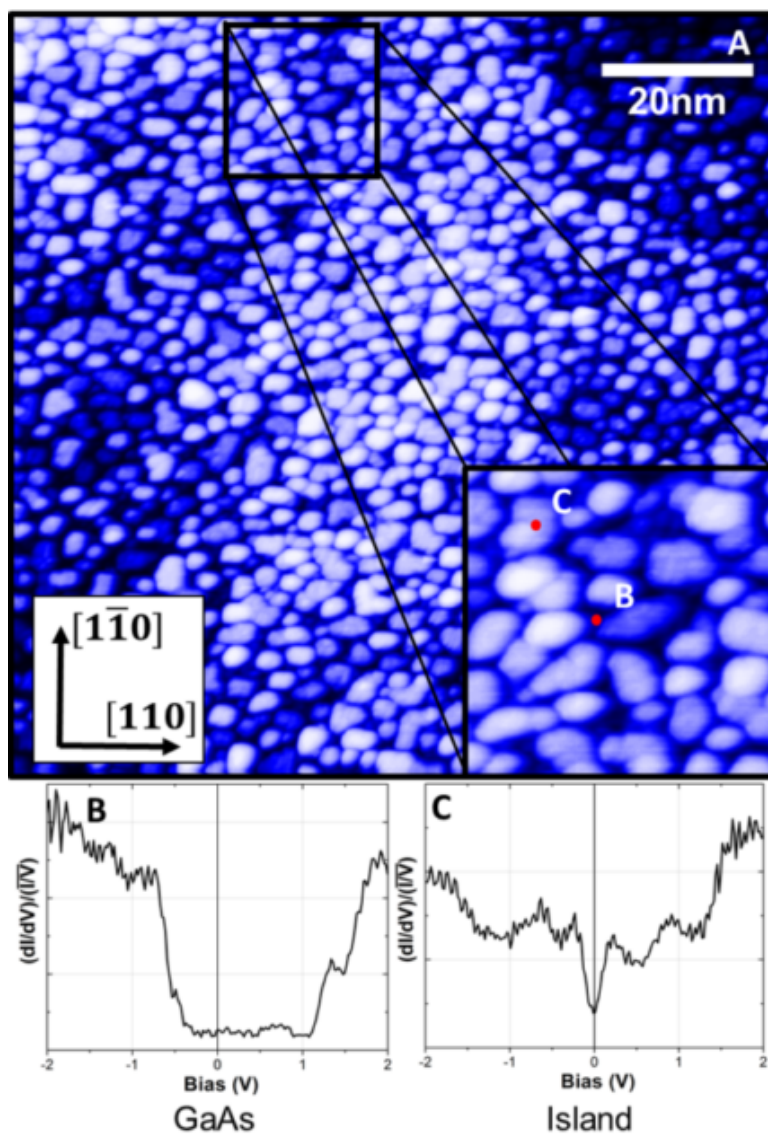


Figure 4.17. After the deposition of 1ML of Co on the $c(4 \times 4)$ GaAs (001) surface, $\langle 110 \rangle$ faceted islands are observed. STS spectra suggest that the surface is metallic, with regions of semiconducting area in between the islands which are labeled GaAs.

in both the semiconducting spectra as well as spectra taken from the top of the island. These features line up well with features observed from the GaAs surface (between islands) suggesting that there is some semiconducting material on top of the islands as well. The island height is 5.6 \AA from the semiconducting surface,

which, after the deposition of only 2ML Co_2MnSi , or 2.82\AA , suggests that these islands could be formed by a 2ML thick Co_2MnSi layer under a 2ML thick GaAs layer, which could give rise to the states observed in LDOS spectra.

After the deposition of the first two monolayers of film, no significant differences are observed in STS spectra or topography for the two different initiation sequences. Further evidence of GaAs riding on top of the growing Co_2MnSi film is seen in RHEED patterns as well as STM images of a 15.4nm thick Co_2MnSi film. The RHEED pattern shown in figure 4.11 of the thick film shows a slight 2x periodicity, suggesting a surface reconstruction. STM images of this film, shown in figure 4.19, suggest the presence of a mixed $c(2\times 4)/c(4\times 2)$ surface reconstruction with 90° rotational variants. This reconstruction, which is not observed in very thick Co_2MnSi films, is likely caused by 2-fold symmetric GaAs forming on the 4-fold symmetric Co_2MnSi crystal, leading to the formation of 90° rotated domains.

A study of the nucleation of Co_2MnSi on $c(4\times 4)$ GaAs (001) surfaces using both Co- and MnSi-initiation layers suggests that the only major differences in the seeded growth sequence occur during the first two monolayers of growth. MnSi initiations result in semiconducting surfaces after the deposition of the first monolayer, possibly as a result of reactions between the Mn and GaAs as well as the growth of Si clusters. After the growth of Co, films appear to cover the surface and are metallic with DOS similar to that of thick Co_2MnSi films.

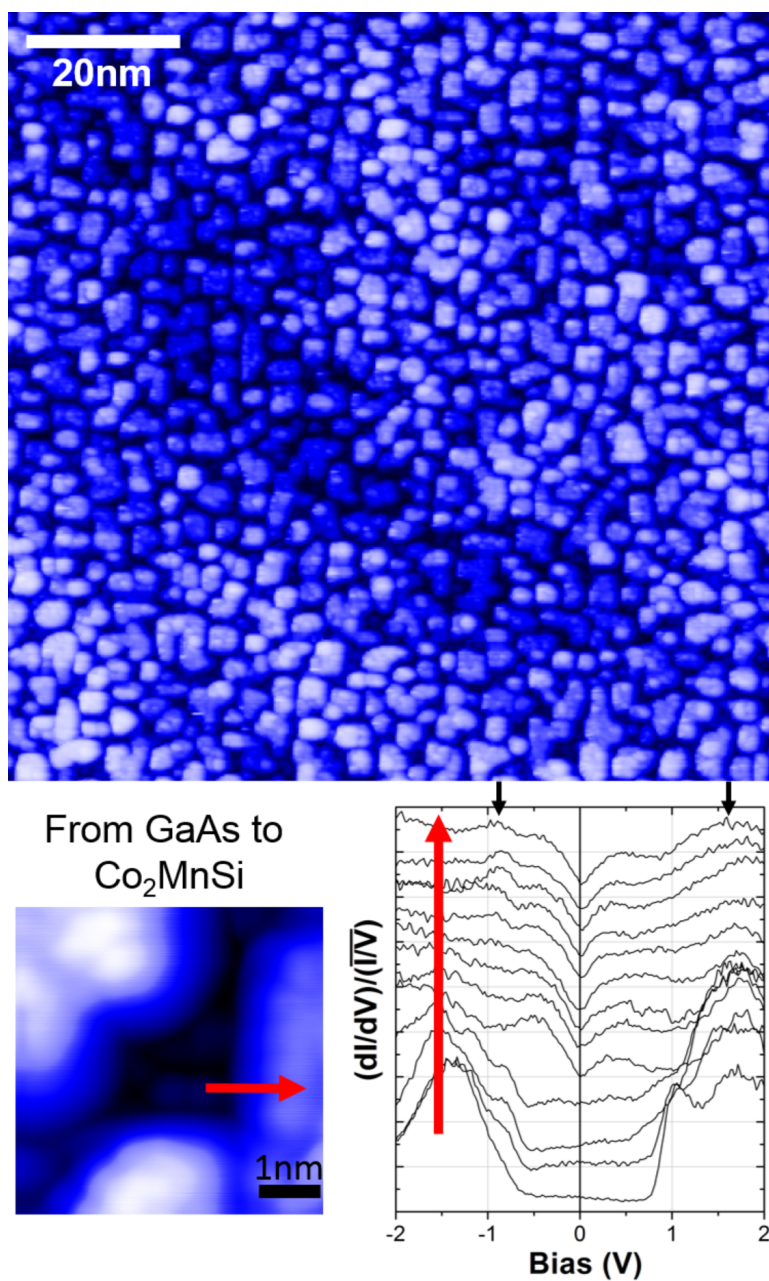


Figure 4.18. STM image (top) of a Co-initiated sample after the deposition of the first ML of MnSi. STS spectra (bottom) taken along a line (denoted by the red arrow) from in-between islands to the top of an island show the transition from a gapped electronic structure to a metallic one. The persistence of LDOS features denoted by the black arrows suggest the presence of GaAs on the surface of the Co₂MnSi island.

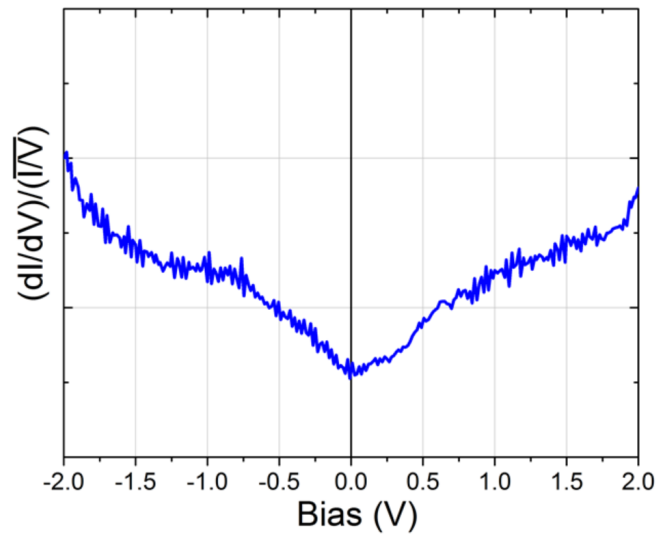
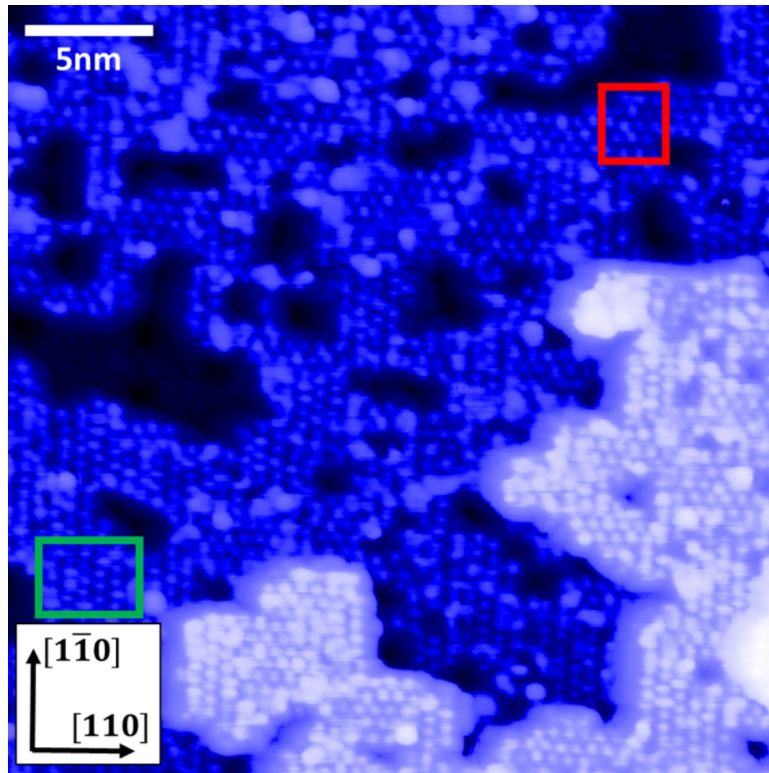


Figure 4.19. STM image (top) of a 15.4nm thick Co_2MnSi film grown on $c(4 \times 4)$ GaAs (001). The image shows surface reconstruction with two rotational variants of $c(2 \times 4)$ reconstructions oriented 90° to each other (red and green boxes). STS measurements (bottom) of the thick film show metallic behavior with a slight dip in LDOS near the Fermi level.

Co initiations results in a metallic film with full coverage from the start, with the deposition of the first monolayer of Co. Deposition of MnSi does not change the surface morphology much, and STS spectra are very similar to the those measured on thick Co₂MnSi films. The STS measurements, as well as height measurements of the growing islands suggest that GaAs rides on top of the surface of the growing Co₂MnSi film, which is further evidenced by the observation of mixed c(2x4)/c(4x2) surface reconstruction on the Co₂MnSi surface. To better understand how the interface forms, and to verify that GaAs rides on the surface of the growing Co₂MnSi film, *in-situ* XPS was used to study the attenuation of Ga and As core-levels as well as the intensity of Co and Mn core-levels as a function of monolayer deposition thickness.

4.4.4 *In-situ* XPS measurements of core-level emission intensity during Co₂MnSi nucleation on c(4x4) GaAs (001) surfaces

Similar to the sequence used for STM measurements, XPS spectra were measured *in-situ* after the growth of each monolayer using an Al K x-ray source with 700meV energy resolution detector at an emission angle of 55° for both Co- and MnSi- initiated samples. To investigate the possibility of Ga and As riding on the growing surface of the Co₂MnSi film, the Ga 3d and As 3d photoemission intensity was analyzed as a function of film thickness. The As 3d intensity at-

tenuation was nearly identical to that of the Ga 3d core level, so it is not shown here. To study the growing film, the Co and Mn 2p core levels were studied as a function of film thickness.

Studying the core level intensity attenuation of a substrate peak in XPS allows for a study of both growth mode and interfacial reactions. Since XPS is extremely surface sensitive, and inelastic mean free paths of electrons are on the order of Ångstroms, so after only the deposition of a few monolayers, substrate peaks attenuate rapidly, allowing for quantitative studies.

Shown in figure 4.20A are XPS spectra of the Ga 3d core level as a function of film thickness, with each subsequent curve corresponding to the deposition of an addition ML of Co_2MnSi . For both nucleation sequences, the Ga 3d core level attenuates for each subsequent monolayer deposition. Assuming that each monolayer provides complete coverage, the expected intensity attenuation of the Ga 3d peak can be calculated. For a detailed description of the intensity modeling and calculations, please refer to the thesis of Brian D. Schultz and the thesis of Jason K. Kawasaki [1, 98].

An inelastic mean free path can be calculated for each layer of Co and each layer of MnSi. Using that inelastic mean free path, since the geometry of the electron analyzer and sample are well known, a normalized intensity expected after each monolayer deposition can be calculated. This analysis makes assumptions about the attenuation coefficient of each layer, and more specifically, in

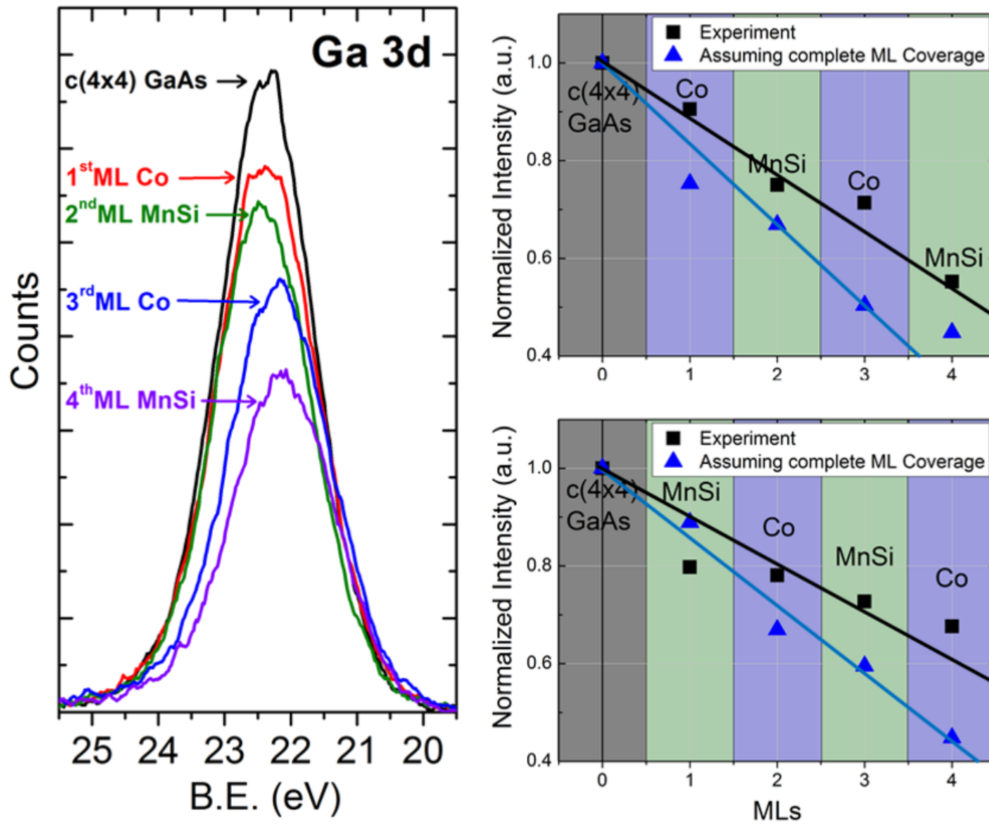


Figure 4.20. Left: Ga 3d core level spectra as a function of monolayer growth thickness for a Co-initiated sample to demonstrate the peak attenuation as a function of Heusler thickness. Top right: Intensity of the Ga 3d core level as a function of Co_2MnSi thickness for a Co initiated sample. Bottom right: Intensity of the Ga 3d core level as a function of Co_2MnSi thickness for a MnSi initiated sample. Black squares correspond to experimentally measured values while blue triangles correspond to theoretical intensity attenuations based on the growth of Co and MnSi monolayers. Also shown are fits as a guide to show the deviation of the experimentally observed attenuation rate from the theoretically expected one.

the case of a MnSi layer, an approximation was used by averaging the inelastic mean free path of a full Mn layer and a full Si layer. The expected intensities, along with the measured intensities are plotted in figure 4.20b and 4.20d for each initiation sequence: (B) Co-first (D) MnSi-first. It is clear that the intensity measured by experiment attenuates at a slower rate than is expected, suggest-

ing that either that the Co_2MnSi film is growing as islands and not completely covering the GaAs, or that Ga is riding on the surface of the growing film. From STM images, it is clear that the Co_2MnSi film is not growing as islands, and any slight deviation from perfect layer coverage that can be observed in the STM images is not reconciled by modeling. Additionally, after the deposition of very thick Co_2MnSi films in excess of 15nm, Ga is still observed by XPS, suggesting that even at these thicknesses, when the film thickness is much greater than the electron inelastic mean free path, Ga is present on the surface of the film. These results suggest that Ga (as well as As, due to the similarities in observed peak attenuation) are likely riding on the surface of the growing film.

Further information about the nucleation and growth of the film can be obtained from analyzing the emission intensity of the Co and Mn 2p core levels. These intensities are also shown in figure 4.21 for both nucleation sequences.

For MnSi initiated films, the core level intensity varies as expected, as the core level intensity for each species increases after deposition, and is attenuated by the deposition of the next monolayer. For Co initiated films, this trend is similar, except for the first two monolayers. The Co 2p intensity, after deposition of the first monolayer of MnSi, remains constant, and is not attenuated. This suggests that the MnSi buries under the previous Co layer to bond with the underlying GaAs. Continued deposition results in the expected rise and attenuation of core levels for both Mn and Co, which suggests a layer-on-top-of-layer growth mode

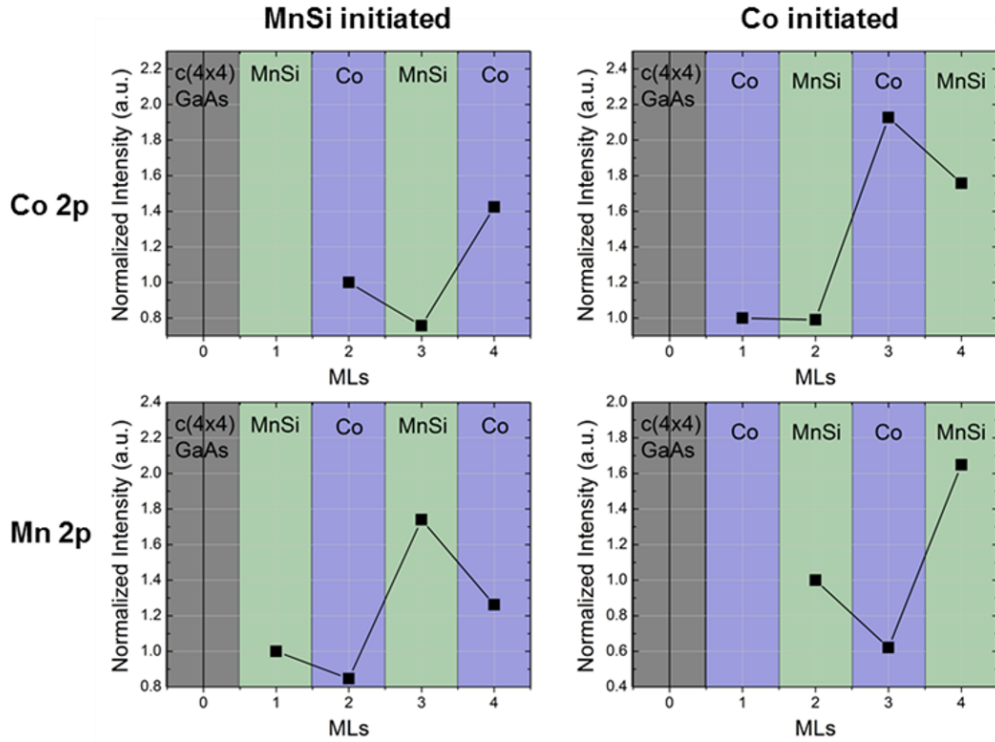


Figure 4.21. Measured intensities of the Co and Mn 2p core levels as a function of growth thickness. MnSi initiated films are shown on the left and Co initiated films are on the right. Intensities are expected to increase upon deposition of the layer that contains the element, and are expected to attenuate after deposition of the next layer. The trend in the MnSi initiated sample is consistent with this description, but for Co initiations, the MnSi layer does not attenuate the first layer, suggesting a burying mechanism.

after the first two monolayers.

These results suggest that there is a strong driving force to form a MnSi-GaAs type interface, and at the high substrate temperatures of 270°C, there is enough energy for the MnSi to bury under the Co layer to form a stable interface. This is consistent with STM measurements as well, as the deposition of MnSi was not observed to significantly change the surface morphology. To verify the formation of a similar MnSi-GaAs type interface regardless of initiation layer,

cross-sectional TEM samples were prepared and studied using HAADF-STEM imaging.

4.4.5 Investigation of the $\text{Co}_2\text{MnSi}/\text{GaAs}$ (001) interface by HAADF-STEM imaging

The $\text{Co}_2\text{MnSi}/\text{GaAs}$ (001) interface is atomically abrupt, as seen in figure 4.22.

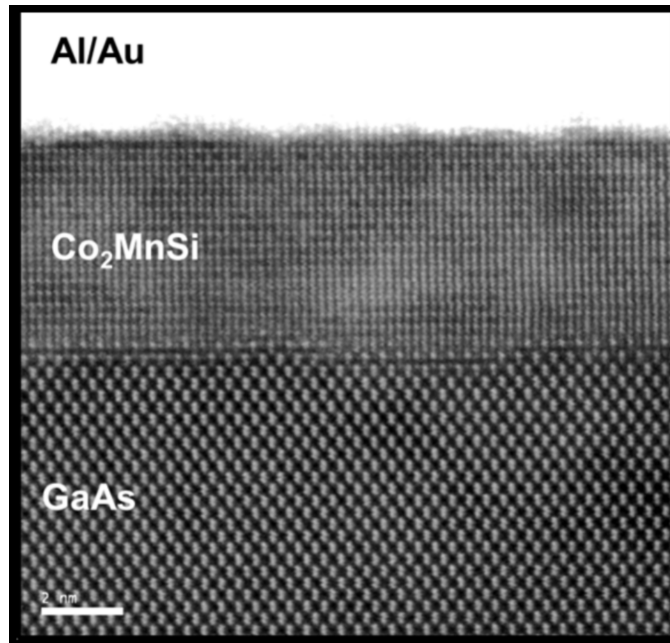


Figure 4.22. High-angle annular dark field scanning transmission electron microscopy (HAADF-STEM) image of the $\text{Co}_2\text{MnSi}/\text{GaAs}$ (001) interface viewed along the $[1\bar{1}0]$ direction showing an atomically abrupt transition from Co_2MnSi to GaAs.

However, rather than simple bulk terminations of Co_2MnSi and GaAs stacked on top of each other, the interfacial structure is rather complex, involving multiple layers of Ga, As, Co, Mn, and Si. HAADF-STEM imaging is sensitive to Z,

or the atomic number, of the atomic column being probed, so atomic columns made up of heavier atoms show up as brighter in the image. From this contrast, it is possible to pick out a few chemical species, but to differentiate between Co and Mn or Ga and As is difficult.

By analysis of the image contrast, possible interfacial atomic models have been calculated and allowed to relax to their equilibrium positions through computational methods. From these positions, HAADF-STEM simulations can be made, and their results can be directly compared to images. Since most of this work was completed in collaboration with Paul Voyles' and Bill Butler's groups at University of Wisconsin-Madison and University of Alabama, the details of the analysis will not be presented here. However, the proposed structure matches well with XPS and STM results, suggesting that a MnSi-GaAs type interface is formed [Figure 4.23].

HAADF-STEM imaging as well as density function theory calculations have suggested that the interfacial structure is similar for both Co- and MnSi- initiated samples. These results match well with *in-situ* XPS and STM measurements. Therefore, it is unlikely that interfacial electronic structure is different between the two samples, and the differences in observed spin signal must come from a modification of the semiconductor band structure near the interface.

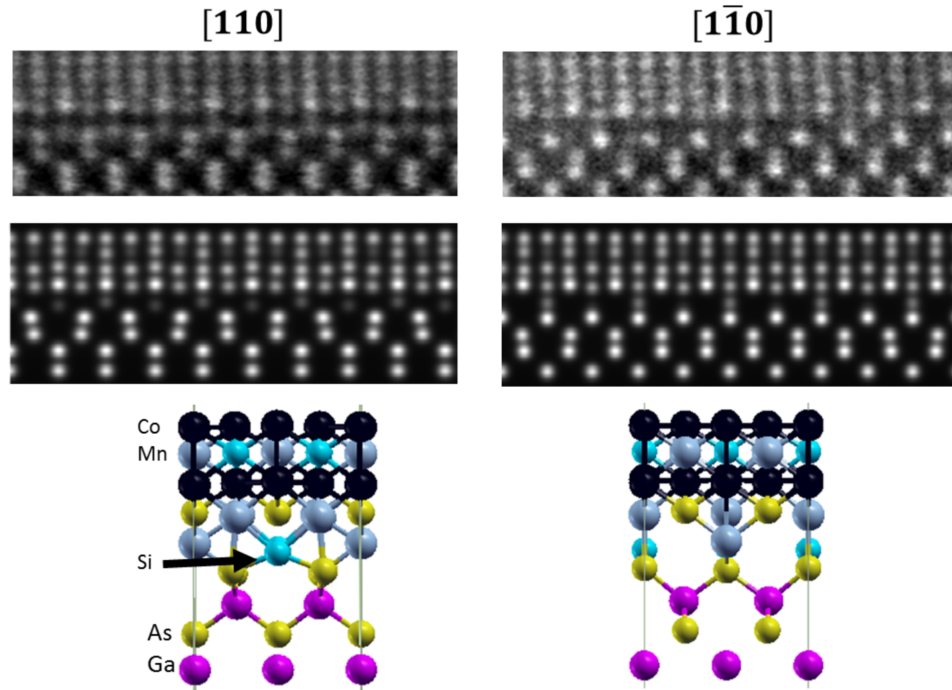


Figure 4.23. High-angle annular dark field scanning transmission electron microscopy (HAADF-STEM) image of the $\text{Co}_2\text{MnSi}/\text{GaAs}$ (001) interface viewed along the $[\bar{1}\bar{1}0]$ direction showing an atomically abrupt transition from Co_2MnSi to GaAs.

4.5 Effects of Co_2MnSi growth conditions on the GaAs band structure near the interface

Changing the nucleation sequence, while intending to modify interfacial structure and bonding, had no observable effects on the interfacial structure, likely due to a strong driving force to form a MnSi-GaAs type interface. Since the bulk and interfacial structures are the same using both nucleation sequences, it is likely that the change in spin injection properties is due to a modification of semiconductor band structure near the ferromagnet.

Mn is a shallow acceptor in GaAs, and Mn diffusion from the Co_2MnSi

into the GaAs could significantly effect the Schottky barrier width, which is determined by both the barrier height and the charge density profile of the space charge region. It is possible that compensation of the n-type Si dopants by Mn greatly affects the Schottky barrier shape, which has been shown to strongly effect the magnitude of observed spin signals [99].

In a study by Hu, *et. al.*, an optimal thickness of 15nm for the $n+$ GaAs contact region was determined [99], but for Co_2MnSi , this was too thin, and the $n+$ region was increased to 18nm to observe spin signals in non local spin valve devices. This suggests that for Co_2MnSi injectors, there is some compensation of the $n+$ region, likely by the diffusion of Mn into the GaAs from the Heusler electrode.

To study the extent of Mn diffusion into the GaAs, secondary ion mass spectrometry (SIMS) was employed. To avoid effects of knocking-on Co, Mn, and Si into the GaAs from the metal, and to increase depth resolution, the substrate was removed and SIMS analysis was performed by sputtering from the backside of the sample using previously developed techniques [85].

Specifically for this study, Co_2MnSi films were grown on 500\AA GaAs/(100\AA $\text{Al}_{0.1}\text{Ga}_{0.9}\text{As}/100\text{\AA}$ GaAs) x 3 superlattice/ 100\AA GaAs/ 5000\AA $\text{Al}_{0.8}\text{Ga}_{0.2}\text{As}/\text{GaAs}$ (001) structures. Two samples were grown, one with a Co- initiation sequence and one with a MnSi- initiation sequence. To remove the substrate, samples were mechanically polished to a thickness of $110\mu\text{m}$, then the remaining GaAs

was removed using 30:1 $\text{H}_2\text{O}_2:\text{NH}_4\text{OH}$ solution using the $\text{Al}_{0.8}\text{Ga}_{0.2}\text{As}$ as an etch stop. Finally, buffered HF (1:7 HF: NH_4F) was used to remove the $\text{Al}_{0.8}\text{Ga}_{0.2}\text{As}$ layer, leaving a GaAs surface. The 100\AA $\text{Al}_{0.1}\text{Ga}_{0.9}\text{As}/100\text{\AA}$ GaAs superlattice was used as a sputtering rate calibration for depth.

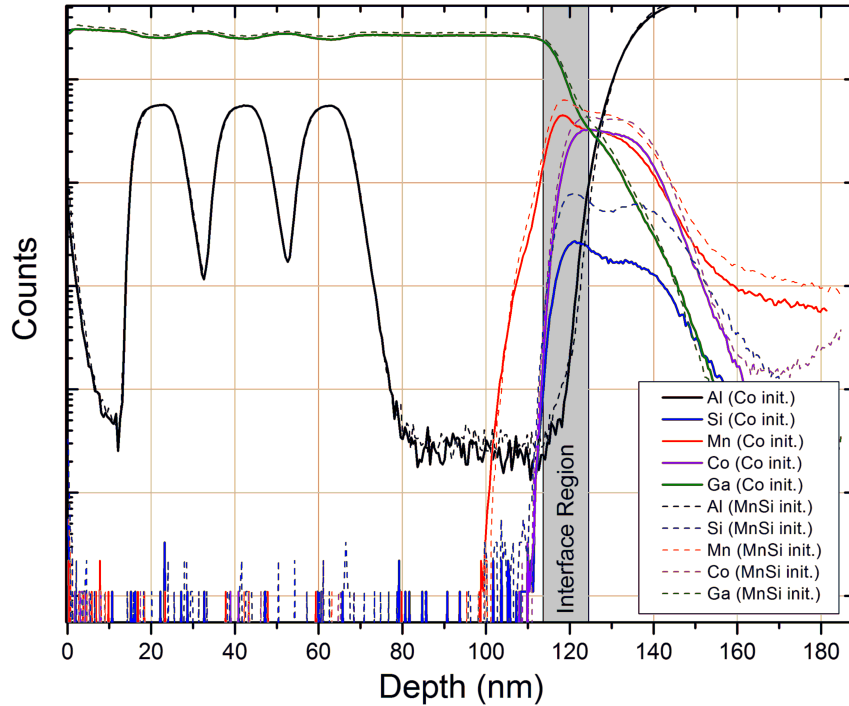


Figure 4.24. Backside SIMS profiles for MnSi- and Co- initiated $\text{Co}_2\text{MnSi}/\text{GaAs}$ (001) structures. A rise in Mn signal before the rise of Co and Si in the interfacial region suggests a diffusion of Mn into the GaAs which could be compensating the n-type Schottky contact. Due to the effects of intermixing and depth resolution of SIMS, a difference between MnSi- and Co- initiated samples was not observed and no conclusions regarding the difference in Mn in-diffusion could be made.

Figure 4.24 shows Ga, Al, Co, Mn, and Si signals from SIMS measurements. The interface of the Co_2MnSi and GaAs is located 1230\AA deep, which is seen in the spectra by the dramatic rise of both the Co and Si signals. The rise

of the Mn signal before the interface suggests significant Mn diffusion into the GaAs. This diffusion, on the order of 20Å - 50Å from the interface, is likely to partially compensate the effects of the Si doping which is required to obtain a narrow Schottky barrier. This “diffusion layer” thickness also matches well with the required increase of the $n+$ region in $\text{Co}_2\text{MnSi}/\text{GaAs}$ (001) structures from 150Å to 180Å as compared to Fe/GaAs (001) structures.

Unfortunately, for both initiation sequences, there were no strong differences in the observed Mn signal within the GaAs. It is likely that the SIMS technique is not sensitive enough to measure very small differences in Mn concentration near the interface. To obtain a more sensitive probe, I-V measurements of the contacts were taken.

4.5.1 I-V measurements of $\text{Co}_2\text{MnSi}/\text{GaAs}$ Schottky contacts

I-V characteristics of the grown Schottky diodes provide a more sensitive electronic probe to study the semiconductor bandstructure near the $\text{Co}_2\text{MnSi}/\text{GaAs}$ interface. I-V curves were measured on lateral spin valve devices grown using Co-, MnSi-, and Mn- initiated Co_2MnSi spin injectors. For this study, Mn- initiation corresponds to the replacement of the Si atoms in a MnSi layer with Mn.

Since the semiconductor-ferromagnet contact is a Schottky barrier, we expect

rectification and the I-V characteristic of a diode. The equation for thermionic emission, $J = A^*T^2 e^{-\frac{\phi_B}{k_B T}} (e^{\frac{V_F}{k_B T}} - 1)$, could allow for an extrapolation of Schottky barrier height, but unfortunately, due to the degenerate doping of the contact, there is a significant tunneling contribution. However, analysis of the I-V curves can give an idea of the width and height of the Schottky barrier by calculation of the effective barrier height. Using a Richardson constant for metal/*n*-GaAs Schottky contacts determined in Ref. [100] of $4.4 \frac{A}{cm^2 K^2}$, we can calculate effective barrier heights of the 3 different initiations.

Shown in figure 4.25 are forward biased I-V curves on semi-log plots for three samples with identical Si:GaAs doping profiles and three different spin injectors: Co₂MnSi (Co initiated), Co₂MnSi (MnSi initiated), and Co₂MnSi (Mn initiated). By initiating the growth with Co, MnSi, or Mn, an increased amount of Mn at the interface could lead to a larger amount of in-diffused Mn, or a greater modification of the effective Schottky barrier height. Also included are the calculated effective barrier heights for each curve. As the I-V data clearly shows, an increase in effective barrier height is observed for increasing Mn composition in the nucleation layer.

As seen in the data, a clear trend is observed towards higher turn on in I-V curves is observed as Mn content near the interface is increased. The Mn initiated sample is the most resistive, followed by the MnSi initiated sample, and finally the Co initiated sample. This increase in resistance (also observed as an increase

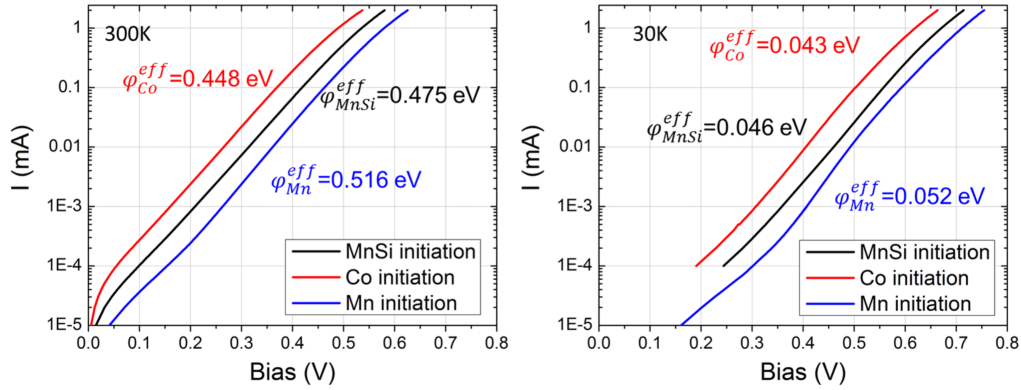


Figure 4.25. I-V characteristics of Co-, MnSi-, and Mn- initiated Co_2MnSi samples plotted on semi-log plots at 300K and 30K. Included are the effective Schottky barrier heights for each curve.

in rectification, as reverse bias IV curves show much lower current) is suggestive of a widening or increase in height of the Schottky barrier. This is likely due to the effects of Mn in-diffusion that were observed in SIMS measurements.

4.5.2 Effect of modification of band structure on spin injection properties

It is clear the Mn compensation of the Schottky barrier is dominating the spin injection process. The addition of excess Mn at the interface, by replacing all Si atoms with Mn, resulted in even more compensation as observed through IV curves.

From SIMS spectra, it is quite clear that Mn diffuses strongly in the GaAs layer, as it is seen as far as 20\AA - 50\AA into the GaAs. However, for the two nucleation sequences, the amount of Mn that diffuses is likely different. The more

rectifying I-V characteristics of lateral spin transport devices with a Mn initiation layer as compared to Co and MnSi initiation layers suggest that the Schottky barrier is modified by the diffusion of more Mn into the first few GaAs layers. Since the n-type silicon doping profile was held constant, this would result in a modification of both the Schottky barrier width. For Co initiated samples, the lower compensation ratio would result in a narrow Schottky contact with more ohmic I-V characteristics. For MnSi initiated samples, the higher compensation ratio would result in a wider Schottky contact with more rectifying I-V characteristics. Both of these trends are observed in lateral spin valve devices, with higher spin signals seen and more rectifying I-V characteristics observed in Mn initiated samples as compared to Co and MnSi initiated ones.

The increase in rectification observed in I-V measurements of MnSi initiated samples could be related to a modification of Schottky barrier height by a change in Fermi-level pinning position at the interface, or solely due to a modification of Schottky barrier width due to compensation of n-type carriers from Mn diffusion into the GaAs. The HAADF-STEM imaging, however, as well as XPS spectra during nucleation, show that the interfacial structure remains constant for both initiation sequences, suggesting a similar interfacial state density and energy level for both initiation sequences, and a similar Fermi-level pinning position. Therefore, we propose that Mn diffusion into the GaAs provides acceptor levels that compensate Si-doping and increase the width of the space-charge region,

resulting in a wider Schottky barrier and tunneling contact.

From these results, we believe that Co_2MnSi films are promising choices as spin injectors into GaAs and we have demonstrated that large signals can be obtained in lateral spin valve devices. While it seems like the choice of nucleation sequence does not significantly affect the spin signal, we do note that MnSi initiated films have a higher “turn on” voltage of the spin signal due to increased rectification. We also observe slightly higher noise on the MnSi initiated samples, likely due to the increased rectification from extra Mn diffusion and compensation of the Schottky contact. We therefore propose that the Co initiation results in a better device performance and should be used for future devices.

4.6 Outlook for Heusler compound spin injectors into III-V materials

The results presented in this thesis suggest that Heusler compounds are quite promising for use as spin injectors into III-V materials. When compared to typical spin injectors like Fe, the observed spin signals are increased by as much as 20x, suggesting both a larger spin injection efficiency as well as a better spin detection efficiency. For GaAs based devices, Co_2MnSi and Co_2FeSi were the most logical choices of Heusler spin injector due to their near lattice-match,

but unfortunately, in the case of Co_2MnSi , Mn diffusion into the GaAs was detrimental to the Schottky tunneling contact, and for Co_2FeSi , the ferromagnet is not 100% spin polarized. The ideal choice for a spin injector would be one that does not contain elements that may p-dope the GaAs (like Mn), but would display 100% spin polarization in the bulk.

This work demonstrated the ability to grow the quaternary Heusler $\text{Co}_2\text{Fe}_x\text{Mn}_{1-x}\text{Si}$. By increasing the Fe composition x , the valence electron count per formula unit was increased leading to a tuning of the Fermi level within the minority spin gap. Therefore, while the compound Co_2FeSi may have a minority spin polarization of less than 100%, it may be possible to reduce the valence electron count by the growth of the alloy $\text{Co}_2\text{FeAl}_x\text{Si}_{1-x}$ which could tune the Fermi level back into a minority gap without the presence of a reactive dopant like Mn. This will remain a prospect for future studies.

For other III-V semiconductors, like InAs or $\text{In}_x\text{Ga}_{1-x}\text{As}$, as proposed in the Datta-Das spin-FET, there are many other Heusler compounds that could be grown either lattice-matched or lattice-mismatched. For example, Co_2TiSn , with a lattice constant of 6.07\AA and a predicted half-metallic electronic structure, would be ideal for use as a spin injector into either GaSb or InAs [101, 102]. There has been little research in the field of growing Heusler compounds on III-V semiconductors, but due to their ideal lattice match and similar structures, the Heusler/III-V heterostructure is promising for spintronic devices.

Chapter 5

Outlook of Heusler compounds for future research

This work has hopefully demonstrated some of the really interesting properties of Heusler compounds, including the tunability that is inherent in their electronic structure. The tunability not only allows for structural/lattice-matching, but also allows for a continuous variation of the electronic structure.

We demonstrated the growth of Heusler compounds, including Co_2MnSi , Co_2FeSi , PtLuSb , and PtLuBi on III-V semiconductors. Their ideal lattice constant match as well as similar crystal structures to the III-V semiconductor family should allow for Heusler/III-V integration. For spin injection into III-V's Heusler compounds boast high spin polarizations as well as high Curie temperatures. Because of this, Heusler-injector based semiconductor spintronics may be able to operate at room temperature, where effects of spin dephasing can be

overcome by the brute force method of increasing the overall polarization. In fact, some preliminary work that is not included in this thesis has demonstrated room temperature spin signal in $\text{Co}_2\text{FeSi}/\text{GaAs}$ (001) lateral spin valve devices, so further improvements in fabrication techniques as well as in spin polarization should be researched to improve the room temperature operation of these devices.

We should also not only think of Heusler devices that integrate with existing semiconductors, but we should also look at the possibility of growing pure-Heusler heterostructures and making all-Heusler devices. Analogous to the strongly electron correlated perovskite oxides, the Heusler compound class exhibits many interesting electronic properties over one similar crystal structure, with very similar lattice parameters. We should be able to grow heterostructures with layers that have different electronic properties, while still retaining similar crystal structures. These devices may rely on current transport from one Heusler into another, or other interesting interfacial phenomena may be studied.

It is likely that the PtLuSb (001) films that we have grown are indeed topologically non-trivial, as we have observed linearly dispersing surface states with strong spin texture. To make these films useful, we must continue to try to engineer ways to open a bulk bandgap to access the topological surface states without bulk conduction. To do this, we can build on $\text{Co}_2\text{Fe}_x\text{Mn}_{1-x}\text{Si}$ experiments, where we can try to shift the Fermi level position upwards by alloying

with an element that contains one more valence electron. In the case of PtLuSb, and ideal choice is Au, where creating a $\text{Pt}_{1-x}\text{Au}_x\text{LuSb}$ alloy could increase the Fermi level position while maintaining a similar electronic structure. If the Fermi level could be placed at the valence band maximum, then the application of biaxial tensile strain through growth on a higher lattice parameter substrate may be able to open a bulk bandgap around the Dirac point of the surface state. This sort of research will be the focus of future work on this project, in hopes of truly engineering a topological insulator, as well as gaining a better understanding the Heusler electronic structure.

Regardless of what type of Heusler devices may be used, there should be an emphasis on trying to grow the highest quality, thin film, Heusler compound heterostructures. Thin films will be necessary for the fabrication of novel devices, and high quality single crystals will be needed to study the intrinsic properties of Heusler compounds. So far most work in Heusler compounds has centered around bulk synthesis or, in the case of magnetic tunnel junctions, sputtering. While bulk crystal growth may synthesize high quality crystals, these materials cannot be integrated into thin film devices. Sputtering of thin films can be used, but the resulting films contain a large number of crystal defects due to the relatively high energy sputtering process. This work has demonstrated the use of molecular beam epitaxy as a premier tool for the growth of high quality Heusler crystals, and further research on the growth of Heusler compounds using

MBE will lead to higher quality films and more reproducible growth techniques.

When high quality heterostructures can be grown, as in the world of III-V semiconductors, the number of devices that can be dreamed of in Heusler compounds is infinite. Interfacing topological insulators with superconductors, or magnetic Heuslers with semiconducting ones, or even doping to create dilute magnetic semiconductors all seem to be interesting avenues of research. Hopefully the interest in these materials will grow leading to more research and greater understanding of their true potential.

Appendix A

In-situ Point-contact Andreev reflection spectroscopy (PCAR)

A.1 Measurements of spin-polarization in ferromagnets: PCAR

The goal of the work completed over the course of this dissertation was to develop new materials that could be used as potential pure spin sources for spintronic devices. Although the non-local spin valve measurements give an idea of the spin polarization of the ferromagnet through measurements of spin accumulation in the semiconductor, they do not truly measure the bulk spin polarization of the ferromagnet. As discussed previously, the spin injection process is quite complicated with spin polarization of the current being dominated by both interfacial band structure as well as semiconductor band structure. Measurement

of the true bulk spin polarization would allow for studies of the actual bulk band structure and the highest attainable spin polarization from a material. Most of the techniques used to measure spin polarization involve the measurement of an interfacial spin polarization. The simplest of these measurements is the use of Jullière’s model for the conversion of tunneling magnetoresistance ratio (TMR) into the spin polarization of the density of states on either side of the tunnel barrier [103]. However, this method really probes the insulator/ferromagnet interfacial density of states, and can be incorrect if effects like spin filtering are present [104]. Another method is the use of the superconductor-insulator-ferromagnet junction in Meservey-Tedrow tunneling experiments, where spectroscopy of tunneling into the superconducting gap at high fields causes a Zeeman splitting of the quasiparticle density of states allowing for a spin polarized probe the ferromagnetic density of states [105]. However, this technique also probes the interfacial density of states at the ferromagnet-insulator interface, so it is not an accurate probe of the bulk density of states.

To probe the bulk spin polarization, point contact Andreev reflection spectroscopy (PCAR) has been proposed [26]. This technique involves the formation of a point contact between a superconductor and a metal, and measuring the conductance through the junction. A simple explanation of the physics is as follows and is schematically depicted in figure A.1. Two types of junctions can be created: superconductor-normal metal, or superconductor-ferromagnet. For

both junctions, when tunneling at biases greater than the superconducting gap, electrons of either spin are allowed to tunnel into and out of the superconductor without pairing, so the conductance spectra is determined almost purely by the relatively flat superconducting density of states. At biases within the gap, the superconductor requires electrons to be paired with another of opposite spin, to be conducted as a Cooper pair at the Fermi energy. In a superconductor-normal metal junction, this means that any electron that travels across the junction “pulls” another electron of opposite spin with it, reflecting an extra hole, and leading to a doubling of the conductance. For a superconductor ferromagnet junction (taking the extreme case of a half-metallic ferromagnet, where there are no minority spin states at the Fermi level), if a spin up electron is incident on the junction, there are no available spin down electrons to pair with it as a cooper pair, which results in the electron being reflected off of the junction rather than being transmitted. The net effect is that within the superconducting gap, the conductance drops to zero.

Assuming that the measurement is not done at 0K (which is always the case), thermal broadening comes into effect, and broadens the superconducting band edge, which results in non-zero conductance within the gap for a superconducting-half metal junction. However, models have been developed which account for thermal broadening and claim to be able to extract a spin polarization of the ferromagnet by fitting the conductance spectra in and around

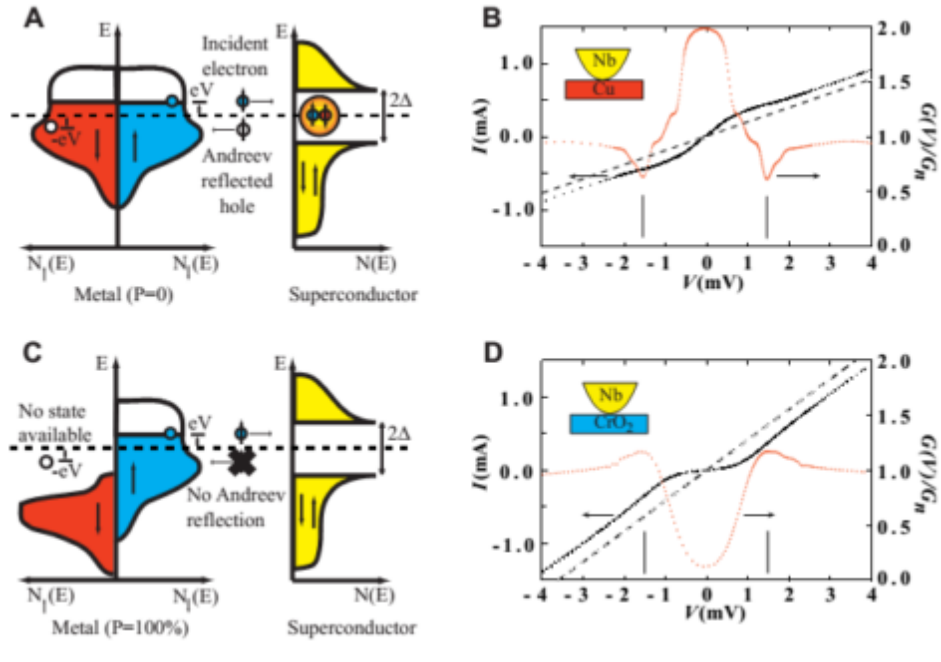


Figure A.1. (A) Schematic drawing of Andreev reflection process for a normal-superconductor junction with a polarization of 0. (B) IV and dI/dV spectra of a Nb-Cu point contact showing double conductance at 0 bias. (C) Schematic drawing of Andreev reflection process for a ferromagnet-superconductor junction with a polarization of 1. (D) IV and dI/dV spectra of a Nb-CrO₂ point contact showing near zero conductance at 0 bias [26].

the superconducting gap [106–108].

A.2 Traditional PCAR measurements and the advantages of *in-situ* growth and measurement

PCAR measurements have traditionally been performed with fairly crude experimental setups, where superconducting wire is sharpened into a tip with sandpaper and driven into a ferromagnet using a set-screw, as depicted in figure A.2 until IV spectra representing a superconducting point contact are observed [26, 106, 107, 109]. However, these techniques can induce quite a large amount of contamination at the superconductor-ferromagnet interface that may affect the spin transport at the interface. To control the formation of the point contact, the use of piezo-electric stacks have been employed to slowly bring a wire in contact with the sample [110]. While this approach gives more control over the formation of the point contact, sample surfaces are still exposed to air and contaminants could affect the junction.

To reduce the effects of surface contamination, either through surface oxidation or other contaminants, we set out to perform PCAR measurements *in-situ* in a 4.2K LHe cooled Omicron Low Temperature Scanning Probe Microscope. The samples could be grown and transferred in ultra-high vacuum to keep their surfaces clean, and the STM tip, which has x, y, and z control over position could allow for the positioning of a Nb tip and controlled formation of a point

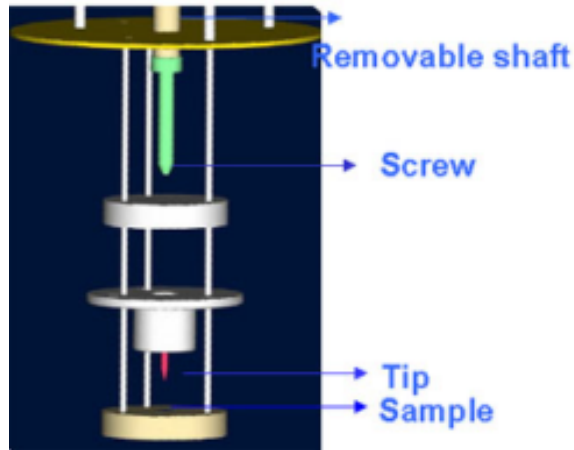


Figure A.2. A schematic diagram of a PCAR setup in a helium bath dewar. The tip is typically driven into the ferromagnetic sample using a set screw [111].

contact. In addition, the Nb tip could be cleaned by *in-situ* electron bombardment to remove its native oxide. This setup could potentially provide some of the cleanest point contacts for analysis.

A.3 PCAR measurements: Measurement design and results

The work presented in this appendix has not been completed, but describes steps towards PCAR measurements of Heusler compounds. Although the setup described in the previous section sounds relatively simple and straightforward, the process of making 4-point measurements *in-situ*, proves quite difficult. The Omicron LTSPM is fitted with 4 internal spring clip contacts which contact a special STM block with 4 contact pads that are isolated from the ground plane of the sample. This sample holder is ideal for device measurements, but cannot

be used as a growth block, as the growth of metal would short out the electrical contact pads on the isolated contact strip. Therefore, an adapter to grow the sample on, then transfer it into the contact block, was required.

The first iteration of the sample holder design was ineffective. Shown in figure A.3b is the first block design, where Ta spring clips were installed on the LTSTM 4 contact sample block. The idea for this design was the the sample was grown on the small block, then transferred into the larger one where the Ta clips would (1) provide electrical contact to the sample surface and (2) provide structural support to hold the sample block in place. In reality, it was impossible to transfer these blocks using a grabbing-action wobblestick in UHV, so the design was scrapped. The second iteration, shown in figure A.3c is the current working iteration. These blocks utilize a slotted rail to hold the sample block, and Ta spring clips to make contact to the sample surface.

The tip for these measurements was made out of Nb, which was created by electrochemical etching in concentrated HCl with and AC voltage. The tip etching setup was based on techniques developed by Uehara, *et al.* [112]. To perform adequate 4-point measurements, voltage probe at the Nb tip was required which was separate from the path of the current through the standard tip holder. To interface well with the LTSTM, we used the shield of the coaxial tunneling current lead as a voltage probe. To access this, an indium wire was bonded from the coaxial shield plane of the tip holder directly to the Nb tip, removing the

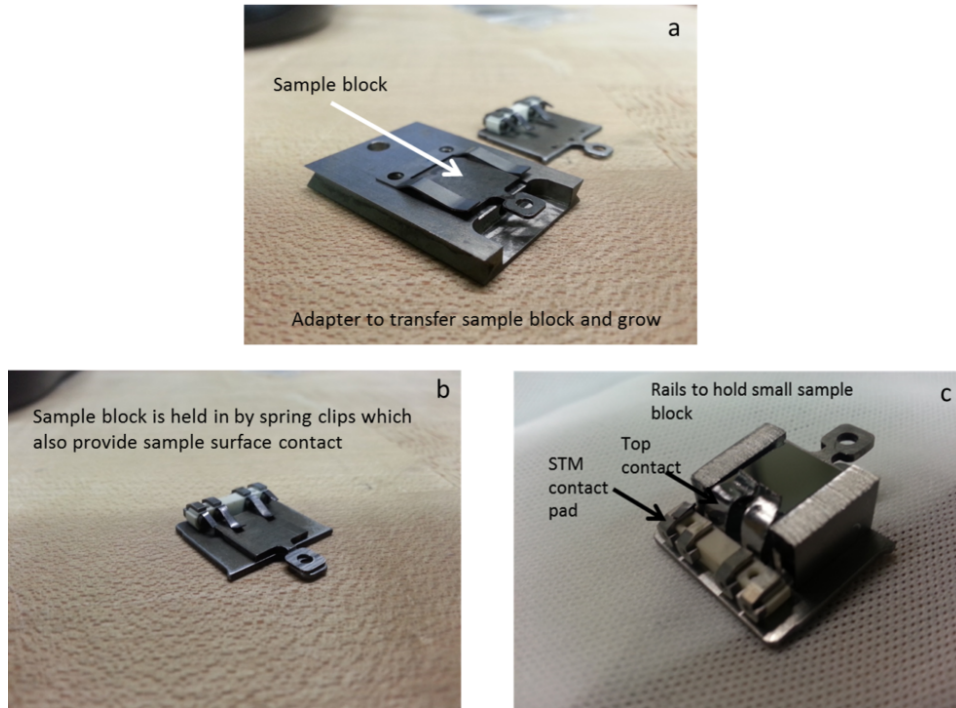


Figure A.3. An image of (a) The sample block adapted, which allowed for growth on the small sample block in the MBE system before transferring to the STM, (b) the first iteration of block design for PCAR sample holders to obtain two points of electrical contact to the sample and (c) the second and current iteration of the design, utilizing slotted rails to hold the sample block in place.

measurement of the superconductor-normal (S-N) junction of the tip holder to the Nb wire. An image of the tip with the bonded gold wire near the sample surface in the STM is shown in figure A.4.

Measurements were performed with I+ and V+ contacts on the tip and I- and V- contacts on the sample using the spring clips discussed previously. dI/dV spectra were recorded using standard AC lock-in techniques. To test the measurement setup, point contacts were made to the Ta spring clips. Figure A.5a shows spectra recorded at 4.2K on the resulting Nb-Ta junction. The near double conductance observed is predicted in the normal-superconductor junction and

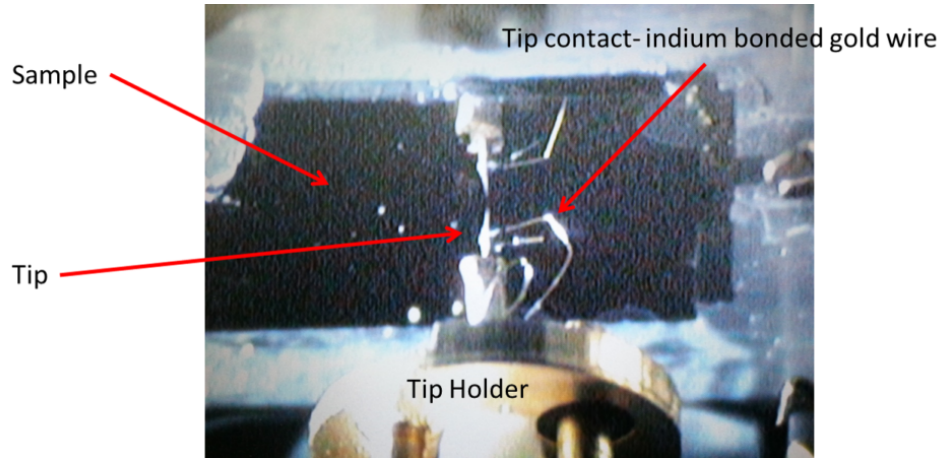


Figure A.4. An image of the Nb tip and its voltage sense wire bonded with In directly to the superconducting Nb tip. Also seen is the sample surface (facing downwards).

verifies the measurement setup working correctly. Unfortunately, measurements of both normal metal (Au) and ferromagnet (Co_2MnSi) thin films ($<20\text{nm}$) on these blocks did not result in PCAR spectra where the superconducting gap was visible. The likely cause of this effect was the additional sheet resistance due to the thin film geometry resulting in voltage drop across the film, washing out effects of the S-F junction in the spectra. Also shown are spectra taken at 2.6K on the Ta clip (obtained by pumping on the helium dewar to lower the LHe boiling point), shown in figure A.5b. At this temperature, Ta superconducts, leading to the observation of additional gap features. The widening of the gap observed is due to additional measurement of line resistances.

So far, we have not been able to successfully measure PCAR spectra on thin films. This is likely due to the additional sheet resistance presented by the film, and the inability to measure the voltage drop from tip to thin film accurately. To

help reduce the effects of sheet resistance, the next step to take is to grow thicker films, so that the voltage measurement probe can be located farther away from the tip-sample junction and still accurately measure the voltage drop from tip to sample. These experiments will be left for future work, but the observation of near double conductance on the Ta clip, suggests that the measurement setup works for thick films or bulk crystals, but needs further fine tuning for the measurement of thin films.

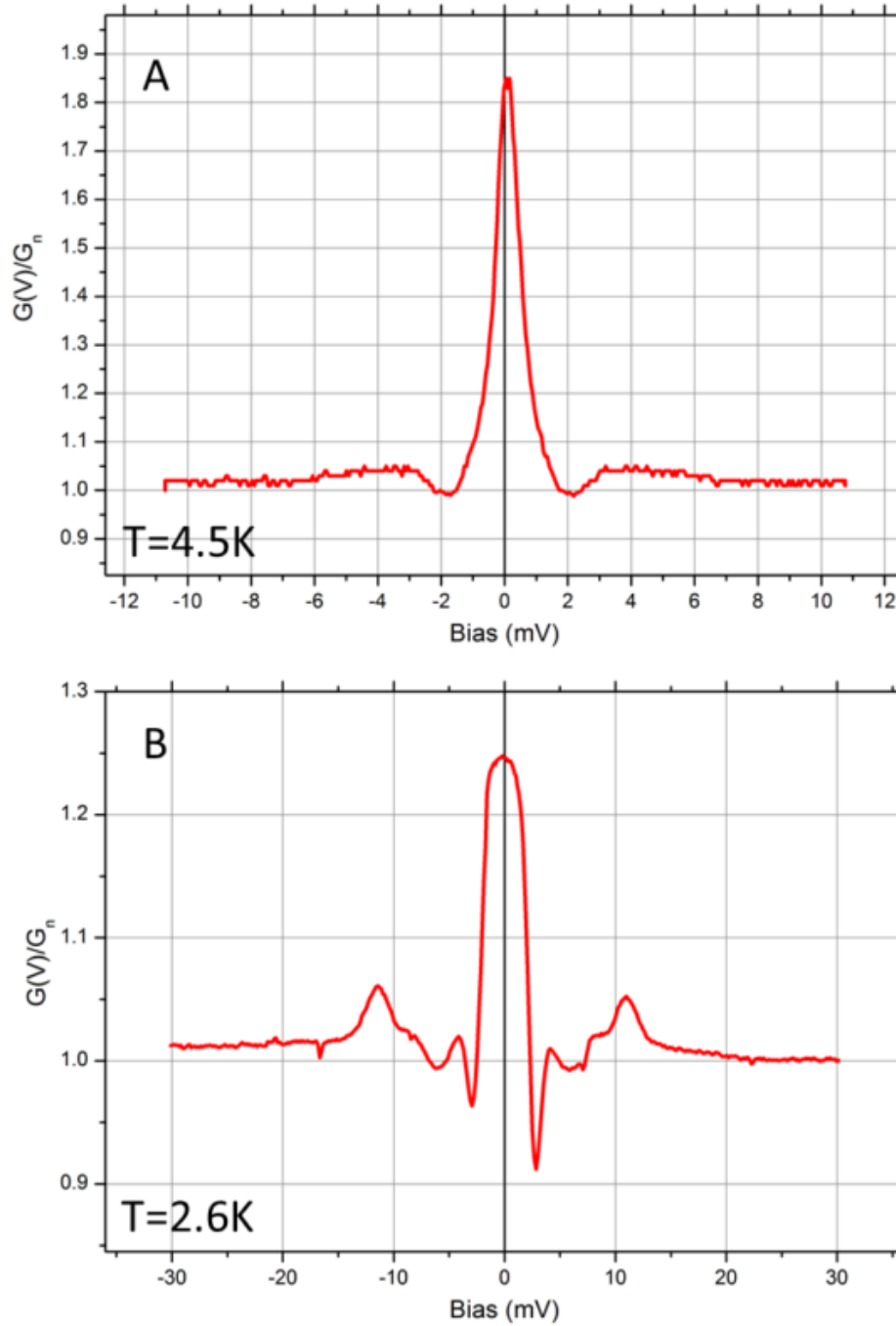


Figure A.5. PCAR spectra taken on Ta clips on sample holder at (A) when the sample temperature was 4.5K, with Ta in its normal metal state, and the tip and voltage probes were on the same contact and (B) when the sample temperature was 2.6K making the Ta clip superconduct and the tip and voltage probes were on two different contacts. Near double conductance is observed in the superconductor normal contact in (A).

Bibliography

- [1] J. K. Kawasaki. Epitaxial growth, surface, and electronic properties of unconventional semiconductors: RE-V/III-V nanocomposites and semi-conducting Half Heusler alloys. *Dissertation*, 2014.
- [2] T. Graf, C. Felser, and S. S. Parkin. Simple rules for the understanding of Heusler compounds. *Progress in Solid State Chemistry*, 39(1):1–50, May 2011. doi:[10.1016/j.progsolidstchem.2011.02.001](https://doi.org/10.1016/j.progsolidstchem.2011.02.001).
- [3] F. Heusler, W. Starck, and E. Haupt. Über magnetische manganlegierungen. *Verhandlungen der Deutschen Physikalischen Gesellschaft*, 5:219, 1903.
- [4] P. Webster. Magnetic and chemical order in Heusler alloys containing cobalt and manganese. *Journal of Physics and Chemistry of Solids*, 32, 1971. doi:[10.1016/S0022-3697\(71\)80180-4](https://doi.org/10.1016/S0022-3697(71)80180-4).
- [5] S. Sakurada and N. Shutoh. Effect of Ti substitution on the thermoelec-

- tric properties of (Zr,Hf)NiSn half-Heusler compounds. *Applied Physics Letters*, 86(8):082105, 2005. doi:[10.1063/1.1868063](https://doi.org/10.1063/1.1868063).
- [6] H. Lin, L. A. Wray, Y. Xia, S. Xu, S. Jia, R. J. Cava, A. Bansil, and M. Z. Hasan. Half-Heusler ternary compounds as new multifunctional experimental platforms for topological quantum phenomena. *Nature Materials*, 9(7):546–9, July 2010. doi:[10.1038/nmat2771](https://doi.org/10.1038/nmat2771).
- [7] S. Chadov, X. Qi, J. Kübler, G. H. Fecher, C. Felser, and S. C. Zhang. Tunable multifunctional topological insulators in ternary Heusler compounds. *Nature Materials*, 9(7):541–5, July 2010. doi:[10.1038/nmat2770](https://doi.org/10.1038/nmat2770).
- [8] W. Al-Sawai, H. Lin, R. S. Markiewicz, L. A. Wray, Y. Xia, S.-Y. Xu, M. Z. Hasan, and A. Bansil. Topological electronic structure in half-Heusler topological insulators. *Physical Review B*, 82(12):125208, Sept. 2010. doi:[10.1103/PhysRevB.82.125208](https://doi.org/10.1103/PhysRevB.82.125208).
- [9] F. F. Tafti, T. Fujii, A. Juneau-Fecteau, S. René de Cotret, N. Doiron-Leyraud, A. Asamitsu, and L. Taillefer. Superconductivity in the non-centrosymmetric half-Heusler compound LuPtBi: A candidate for topological superconductivity. *Physical Review B*, 87(18):184504, May 2013. doi:[10.1103/PhysRevB.87.184504](https://doi.org/10.1103/PhysRevB.87.184504).
- [10] N. P. Butch, P. Syers, K. Kirshenbaum, A. P. Hope, and J. Paglione.

- Superconductivity in the topological semimetal YPtBi. *Physical Review B*, 84(22):220504, Dec. 2011. doi:[10.1103/PhysRevB.84.220504](https://doi.org/10.1103/PhysRevB.84.220504).
- [11] G. Goll, M. Marz, A. Hamann, T. Tomanic, K. Grube, T. Yoshino, and T. Takabatake. Thermodynamic and transport properties of the non-centrosymmetric superconductor LaBiPt. *Physica B: Condensed Matter*, 403(5-9):1065–1067, Apr. 2008. doi:[10.1016/j.physb.2007.10.089](https://doi.org/10.1016/j.physb.2007.10.089).
- [12] M. Søndergaard, M. Christensen, L. Bjerg, K. A. Borup, P. Sun, F. Steglich, and B. B. Iversen. Investigation of the correlation between stoichiometry and thermoelectric properties in a PtSb₂ single crystal. *Dalton transactions (Cambridge, England : 2003)*, 41(4):1278–83, Jan. 2012. doi:[10.1039/c1dt11523e](https://doi.org/10.1039/c1dt11523e).
- [13] W. Xie, A. Weidenkaff, X. Tang, Q. Zhang, J. Poon, and T. Tritt. Recent Advances in Nanostructured Thermoelectric Half-Heusler Compounds. *Nanomaterials*, 2(4):379–412, Nov. 2012. doi:[10.3390/nano2040379](https://doi.org/10.3390/nano2040379).
- [14] J. R. Sootsman, D. Y. Chung, and M. G. Kanatzidis. New and old concepts in thermoelectric materials. *Angewandte Chemie (International ed. in English)*, 48(46):8616–39, Jan. 2009. doi:[10.1002/anie.200900598](https://doi.org/10.1002/anie.200900598).
- [15] F. Casper, T. Graf, S. Chadov, B. Balke, and C. Felser. Half-Heusler compounds: novel materials for energy and spintronic applica-

- tions. *Semiconductor Science and Technology*, 27(6):063001, June 2012. doi:[10.1088/0268-1242/27/6/063001](https://doi.org/10.1088/0268-1242/27/6/063001).
- [16] M. Z. Hasan and J. E. Moore. Three-Dimensional Topological Insulators. *Annual Review of Condensed Matter Physics*, 2:55–78, 2010. doi:[10.1146/annurev-conmatphys-062910-140432](https://doi.org/10.1146/annurev-conmatphys-062910-140432).
- [17] Y. Xia, D. Qian, D. Hsieh, L. Wray, A. Pal, H. Lin, A. Bansil, D. Grauer, Y. S. Hor, R. J. Cava, and M. Z. Hasan. Observation of a large-gap topological-insulator class with a single Dirac cone on the surface. *Nature Physics*, 5(6):398–402, May 2009. doi:[10.1038/nphys1274](https://doi.org/10.1038/nphys1274).
- [18] D. Hsieh, D. Qian, L. Wray, Y. Xia, Y. S. Hor, R. J. Cava, and M. Z. Hasan. A topological Dirac insulator in a quantum spin Hall phase. *Nature*, 452(7190):970–4, Apr. 2008. doi:[10.1038/nature06843](https://doi.org/10.1038/nature06843).
- [19] M. N. Baibich, J. M. Broto, A. Fert, F. N. Van Dau, F. Petroff, P. Eitenne, G. Creuzet, A. Friederich, and J. Chazelas. Giant magnetoresistance of (001)Fe/(001)Cr magnetic superlattices. *Physical Review Letters*, 61(21):2472–2475, 1988. doi:[10.1103/PhysRevLett.61.2472](https://doi.org/10.1103/PhysRevLett.61.2472).
- [20] J. Barnas, A. Fuss, R. E. Camley, P. Grnberg, and W. Zinn. Novel magnetoresistance effect in layered magnetic structures: Theory and experiment. *Physical Review B*, 42(13):8110–8120, 1990. doi:[10.1103/PhysRevB.42.8110](https://doi.org/10.1103/PhysRevB.42.8110).

- [21] A. Bratkovsky. Tunneling of electrons in conventional and half-metallic systems: Towards very large magnetoresistance. *Physical Review B*, 56(5):2344–2347, 1997. doi:[10.1103/PhysRevB.56.2344](https://doi.org/10.1103/PhysRevB.56.2344).
- [22] S. Yuasa, T. Nagahama, A. Fukushima, Y. Suzuki, and K. Ando. Giant room-temperature magnetoresistance in single-crystal Fe/MgO/Fe magnetic tunnel junctions. *Nature Materials*, 3(12):868–871, 2004. doi:[10.1038/nmat1257](https://doi.org/10.1038/nmat1257).
- [23] S. Datta and B. Das. Electronic analog of the electro-optic modulator. *Applied Physics Letters*, 56(7):665, 1990. doi:[10.1063/1.102730](https://doi.org/10.1063/1.102730).
- [24] Y. Ohno, D. K. Young, B. Beschoten, F. Matsukura, H. Ohno, and D. D. Awschalom. Electrical spin injection in a ferromagnetic semiconductor heterostructure. *Nature*, 402(6763):790–792, Dec. 1999. doi:[10.1038/45509](https://doi.org/10.1038/45509).
- [25] R. Fiederling, M. Keim, G. Reuscher, W. Ossau, G. Schmidt, A. Waag, and L. W. Molenkamp. Injection and detection of a spin-polarized current in a light-emitting diode. *Nature*, 402:787–790, 1999. doi:[10.1038/45502](https://doi.org/10.1038/45502).
- [26] R. J. Soulen Jr. Measuring the Spin Polarization of a Metal with a Superconducting Point Contact. *Science*, 282(5386):85–88, Oct. 1998. doi:[10.1126/science.282.5386.85](https://doi.org/10.1126/science.282.5386.85).
- [27] B. Hülsen, M. Scheffler, and P. Kratzer. Structural Stability and Magnetic and Electronic Properties of $\text{Co}_2\text{MnSi}(001)/\text{MgO}$ Heterostructures:

- A Density-Functional Theory Study. *Physical Review Letters*, 103(4):046802, July 2009. doi:[10.1103/PhysRevLett.103.046802](https://doi.org/10.1103/PhysRevLett.103.046802).
- [28] T. Ishikawa, H.-X. Liu, T. Taira, K. Matsuda, T. Uemura, and M. Yamamoto. Influence of film composition in Co_2MnSi electrodes on tunnel magnetoresistance characteristics of $\text{Co}_2\text{MnSi}/\text{MgO}/\text{Co}_2\text{MnSi}$ magnetic tunnel junctions. *Applied Physics Letters*, 95(2009):232512, 2009. doi:[10.1063/1.3272926](https://doi.org/10.1063/1.3272926).
- [29] F. Shi, H. Liu, M. Yamamoto, and P. M. Voyles. MnMn/O Interface Termination at the $\text{Co}_2\text{Mn}_\alpha\text{Si}/\text{MgO}$ Interface in Magnetic Tunnel Junctions Investigated by Scanning Transmission Electron Microscopy. *Microscopy and Microanalysis*, 19(Suppl 2):336–337, 2013. doi:[10.1017/S143192761300367X](https://doi.org/10.1017/S143192761300367X).
- [30] G. Schmidt, L. W. Molenkamp, A. T. Filip, and B. J. van Wees. Basic obstacle for electrical spin-injection from a ferromagnetic metal into a diffusive semiconductor. *Physical Review B*, 62(8):R4790, 2000. doi:[10.1103/PhysRevB.62.R4790](https://doi.org/10.1103/PhysRevB.62.R4790).
- [31] E. I. Rashba. Theory of electrical spin injection: Tunnel contacts as a solution of the conductivity mismatch problem. *Physical Review B*, 62(24):267–270, 2000. doi:[10.1103/PhysRevB.62.R16267](https://doi.org/10.1103/PhysRevB.62.R16267).

- [32] X. Lou. Electrical detection of spin transport in ferromagnet-semiconductor heterostructures. *Dissertation*, 2007.
- [33] U. K. Mishra and J. Singh. *Semiconductor Device Physics and Design*. Springer, Dordrecht, 3rd edition, 2008. ISBN 978-1-4020-6480-7.
- [34] S. M. Sze and K. K. Ng. Physics of Semiconductor Devices, 3rd Edition - Simon M. Sze, Kwok K. Ng. In *Physics of Semiconductor Devices*. John Wiley and Sons, Inc., Hoboken, 3rd edition, 2007. ISBN 978-0-471-14323-9.
- [35] H. J. Zhu, M. Ramsteiner, H. Kostial, M. Wassermeier, H. P. Schönherr, and K. H. Ploog. Room-temperature spin injection from Fe into GaAs. *Physical Review Letters*, 87(1):016601, 2001. doi:[10.1103/PhysRevLett.87.016601](https://doi.org/10.1103/PhysRevLett.87.016601).
- [36] X. Lou, C. Adelman, M. Furis, S. A. Crooker, C. J. Palmstrøm, and P. a. Crowell. Electrical detection of Spin accumulation at a ferromagnet-semiconductor interface. *Physical Review Letters*, 96(17):176603, May 2006. doi:[10.1103/PhysRevLett.96.176603](https://doi.org/10.1103/PhysRevLett.96.176603).
- [37] X. Lou, C. Adelman, S. A. Crooker, E. S. Garlid, J. Zhang, S. M. Reddy, S. D. Flexner, C. J. Palmstrøm, and P. A. Crowell. Electrical Detection of Spin Transport in Lateral Ferromagnet-Semiconductor Devices. *Nature Physics*, 3(3):197–202, Feb. 2007. doi:[10.1038/nphys543](https://doi.org/10.1038/nphys543).

- [38] T. Kubota, S. Tsunegi, M. Oogane, S. Mizukami, T. Miyazaki, H. Naganuma, and Y. Ando. Half-metallicity and Gilbert damping constant in $\text{Co}_2\text{Fe}_x\text{Mn}_{1-x}\text{Si}$ Heusler alloys depending on the film composition. *Applied Physics Letters*, 94(12):122504, 2009. doi:[10.1063/1.3105982](https://doi.org/10.1063/1.3105982).
- [39] M. Jourdan, J. Minár, J. Braun, A. Kronenberg, S. Chadov, B. Balke, A. Gloskovskii, M. Kolbe, H. J. Elmers, G. Schönhense, H. Ebert, C. Felser, and M. Kläui. Direct observation of half-metallicity in the Heusler compound Co_2MnSi . *Nature Communications*, 5(May):3974, Jan. 2014. doi:[10.1038/ncomms4974](https://doi.org/10.1038/ncomms4974).
- [40] J. C. Tung and G. Y. Guo. High spin polarization of the anomalous hall current in Co-based Heusler compounds. *New Journal of Physics*, 15(3):033014, Mar. 2013. doi:[10.1088/1367-2630/15/3/033014](https://doi.org/10.1088/1367-2630/15/3/033014).
- [41] W. Wang, Y. Du, E. Liu, Z. Liu, and G. H. Wu. Fabrication and characterization of the gapless half-Heusler YPtSb thin films. *Journal of Applied Physics*, 112(10):103910, 2012. doi:[10.1063/1.4766902](https://doi.org/10.1063/1.4766902).
- [42] J. K. Kawasaki, L. I. M. Johansson, B. D. Schultz, and C. J. Palmstrøm. Growth and transport properties of epitaxial lattice matched half Heusler $\text{CoTiSb/InAlAs/InP(001)}$ heterostructures. *Applied Physics Letters*, 104(2):022109, Jan. 2014. doi:[10.1063/1.4862191](https://doi.org/10.1063/1.4862191).
- [43] J. K. Kawasaki, T. Neulinger, R. Timm, M. Hjort, A. A. Za-

- kharov, A. Mikkelsen, B. D. Schultz, and C. J. Palmstrøm. Epitaxial growth and surface studies of the Half Heusler compound NiTiSn (001). *Journal of Vacuum Science and Technology B*, 31(4):04D106, 2013. doi:[10.1116/1.4807715](https://doi.org/10.1116/1.4807715).
- [44] S. J. Patel, J. K. Kawasaki, J. Logan, B. D. Schultz, J. Adell, B. Thiagarajan, A. Mikkelsen, and C. J. Palmstrøm. Surface and electronic structure of epitaxial PtLuSb (001) thin films. *Applied Physics Letters*, 104(20):201603, May 2014. doi:[10.1063/1.4879475](https://doi.org/10.1063/1.4879475).
- [45] P. Bach, C. Rüster, C. Gould, C. R. Becker, G. Schmidt, and L. W. Molenkamp. Growth of the half-Heusler alloy NiMnSb on (In,Ga)As/InP by molecular beam epitaxy. *Journal of Crystal Growth*, 251(3):323–326, 2003. doi:[10.1016/S0022-0248\(02\)02151-6](https://doi.org/10.1016/S0022-0248(02)02151-6).
- [46] R. Farrow, editor. *Molecular Beam Epitaxy*. Noyes Publications, Park Ridge, 1995. ISBN 0815513712.
- [47] Scanning tunneling microscope. URL http://en.wikipedia.org/wiki/Scanning_tunneling_microscope.
- [48] J. A. Stroscio and W. J. Kaiser, editors. *Scanning Tunneling Spectroscopy*. Academic Press, Inc., San Diego, volume 27 edition, 1993.
- [49] D. Kitchen, A. Richardella, J.-M. Tang, M. E. Flatté, and A. Yazdani. Atom-by-atom substitution of Mn in GaAs and visualization

- of their hole-mediated interactions. *Nature*, 442(July):436–439, 2006. doi:[10.1038/nature04971](https://doi.org/10.1038/nature04971).
- [50] Saiht. ARPESgeneral. URL http://en.wikipedia.org/wiki/Angle-resolved_photoemission_spectroscopy.
- [51] C. N. Berglund and W. E. Spicer. Photoemission Studies of Copper and Silver: Theory. *Physical Review*, 136(4):A1030–A1044, 1964. doi:[10.1103/PhysRev.136.A1030](https://doi.org/10.1103/PhysRev.136.A1030).
- [52] S. Hufner. *Photoelectron Spectroscopy*. Springer, New York, 3rd edition, 2003. ISBN 9783642075209.
- [53] F. J. Himpsel. Experimental determination of bulk energy band dispersions. *Applied optics*, 19(23):3964–3970, 1980. doi:[10.1364/AO.19.003964](https://doi.org/10.1364/AO.19.003964).
- [54] Q. Hu. Electrical Spin Injection and Detection in Ferromagnet-Semiconductor Heterostructures. *Dissertation*, 2011.
- [55] M. Johnson and R. H. Silsbee. Interfacial charge-spin coupling: Injection and detection of spin magnetization in metals. *Physical Review Letters*, 55(17):1790–1793, 1985. doi:[10.1103/PhysRevLett.55.1790](https://doi.org/10.1103/PhysRevLett.55.1790).
- [56] F. J. Jedema, H. B. Heersche, A. T. Filip, J. J. A. Baselmans, and B. J. van Wees. Electrical detection of spin precession in a metallic mesoscopic spin valve. *Nature*, 416(April):713–716, 2002. doi:[10.1038/416713a](https://doi.org/10.1038/416713a).

- [57] S. A. Crooker, E. S. Garlid, A. N. Chantis, D. L. Smith, K. S. M. Reddy, Q. O. Hu, T. Kondo, C. J. Palmström, and P. A. Crowell. Bias-controlled sensitivity of ferromagnet/semiconductor electrical spin detectors. *Physical Review B - Condensed Matter and Materials Physics*, 80(4):2–5, 2009. doi:[10.1103/PhysRevB.80.041305](https://doi.org/10.1103/PhysRevB.80.041305).
- [58] K. Christie. *Non-equilibrium spin accumulation in $\text{Co}_2\text{Fe}_x\text{Mn}_{1-x}\text{Si}/n\text{-GaAs}$ heterostructures*. PhD thesis, 2014.
- [59] T. Akiho, J. Shan, H.-x. Liu, K.-i. Matsuda, M. Yamamoto, and T. Uemura. Electrical injection of spin-polarized electrons and electrical detection of dynamic nuclear polarization using a heusler alloy spin source. *Phys. Rev. B*, 87:235205, Jun 2013. doi:[10.1103/PhysRevB.87.235205](https://doi.org/10.1103/PhysRevB.87.235205).
- [60] D. Paget, G. Lampel, B. Sapoval, and V. I. Safarov. Low field electron-nuclear spin coupling in gallium arsenide under optical pumping conditions. *Phys. Rev. B*, 15(12):5780–5796, Jun 1977. doi:[10.1103/PhysRevB.15.5780](https://doi.org/10.1103/PhysRevB.15.5780).
- [61] F. Meier and B. Zakharchenya, editors. *Optical Orientation*, volume 8 of *Modern Problems in Condensed Matter Sciences*. North Holland, New York, 1984.
- [62] M. Chan. *Hyperfine Effects in Ferromagnet-Semiconductor Heterostructures*. PhD thesis, 2010.

- [63] A. Ohtake. Surface reconstructions on GaAs(001). *Surface Science Reports*, 63(7):295–327, July 2008. doi:[10.1016/j.surfrep.2008.03.001](https://doi.org/10.1016/j.surfrep.2008.03.001).
- [64] J. L. Davis, P. E. Thompson, and R. J. Wagner. Growth and characterisation of InSb/GaAs grown using molecular beam epitaxy, 1999. URL <http://iopscience.iop.org/0268-1242/5/3S/050>.
- [65] T. Zhang, S. K. Clowes, M. Debnath, A. Bennett, C. Roberts, J. J. Harris, R. A. Stradling, L. F. Cohen, T. Lyford, and P. F. Fewster. High-mobility thin InSb films grown by molecular beam epitaxy. *Applied Physics Letters*, 84(22):4463, 2004. doi:[10.1063/1.1748850](https://doi.org/10.1063/1.1748850).
- [66] C. Shekhar, S. Ouardi, G. H. Fecher, A. Kumar Nayak, C. Felser, and E. Ikenaga. Electronic structure and linear magnetoresistance of the gapless topological insulator PtLuSb. *Applied Physics Letters*, 100(25):252109, 2012. doi:[10.1063/1.4730387](https://doi.org/10.1063/1.4730387).
- [67] Z. Hou, Y. Wang, G. Xu, X. Zhang, E. Liu, W. Wang, Z. Liu, X. Xi, W. Wang, and G. Wu. Transition from semiconducting to metallic-like conducting and weak antilocalization effect in single crystals of LuPtSb. *Applied Physics Letters*, 106:102102, 2015. doi:[10.1063/1.4914545](https://doi.org/10.1063/1.4914545).
- [68] C. Goletti, U. Resch-Esser, J. Foeller, N. Esser, W. Richter, B. Brar, and H. Kroemer. A reflectance anisotropy spectroscopy study of

- GaSb(100)c(2x6) surfaces prepared by Sb decapping. *Surface Science*, 352-354:771–775, 1996. doi:[10.1016/0039-6028\(95\)01226-5](https://doi.org/10.1016/0039-6028(95)01226-5).
- [69] U. Resch-Esser, N. Esser, B. Brar, and H. Kroemer. Microscopic structure of GaSb(001) c(26) surfaces prepared by Sb decapping of MBE-grown samples. *Physical Review B*, 55(23):15401–15404, 1997. doi:[10.1103/PhysRevB.55.15401](https://doi.org/10.1103/PhysRevB.55.15401).
- [70] B. D. Schultz, H. H. Farrell, M. M. R. Evans, K. Ludge, and C. J. Palmstrøm. ErAs interlayers for limiting interfacial reactions in Fe/GaAs(100) heterostructures. *Journal of Vacuum Science & Technology B*, 20(4):1600, 2002. doi:[10.1116/1.1491994](https://doi.org/10.1116/1.1491994).
- [71] C. G. Duan, R. F. Sabiryanov, W. N. Mei, P. A. Dowben, S. S. Jaswal, and E. Y. Tsymbal. Magnetic ordering in Gd monopnictides: Indirect exchange versus superexchange interaction. *Applied Physics Letters*, 88, 2006. doi:[10.1063/1.2200767](https://doi.org/10.1063/1.2200767).
- [72] I. Vitomirov, A. Raisanen, and A. Finnefrock. Geometric ordering, surface chemistry, band bending, and work function at decapped GaAs (100) surfaces. *Physical Review B*, 46(20):13293, 1992. doi:<http://dx.doi.org/10.1103/PhysRevB.46.13293>.
- [73] M. Sieger, T. Miller, and T. Chiang. Reflection high-energy electron

- diffraction and photoemission study of GaSb(100) reconstructions. *Physical Review B*, 52(11):8256–8265, 1995. doi:[10.1103/PhysRevB.52.8256](https://doi.org/10.1103/PhysRevB.52.8256).
- [74] R. Shan, S. Ouardi, G. H. Fecher, L. Gao, A. Kellock, K. P. Roche, M. G. Samant, C. E. ViolBarbosa, E. Ikenaga, C. Felser, and S. S. P. Parkin. Electronic and crystalline structures of zero band-gap LuPdBi thin films grown epitaxially on MgO(100). *Applied Physics Letters*, 102(17):172401, 2013. doi:[10.1063/1.4802795](https://doi.org/10.1063/1.4802795).
- [75] X. Weng, R. S. Goldman, D. L. Partin, and J. P. Heremans. Evolution of structural and electronic properties of highly mismatched InSb films. *Journal of Applied Physics*, 88(11):6276, 2000. doi:[10.1063/1.1324702](https://doi.org/10.1063/1.1324702).
- [76] P. C. Canfield, J. D. Thompson, W. P. Beyermann, A. Lacerda, M. F. Hundley, E. Peterson, Z. Fisk, and H. R. Ott. Magnetism and heavy fermion-like behavior in the RBiPt series. *Journal of Applied Physics*, 70(1991):5800–5802, 1991. doi:[10.1063/1.350141](https://doi.org/10.1063/1.350141).
- [77] R. Feenstra. Tunneling spectroscopy of the (110) surface of direct-gap III-V semiconductors. *Physical Review B*, 50(7):4561–4570, 1994. doi:<http://dx.doi.org/10.1103/PhysRevB.50.4561>.
- [78] R. Feenstra, J. Lee, M. Kang, G. Meyer, and K. Rieder. Band gap of the Ge(111)c(28) surface by scanning tunneling spectroscopy. *Physical Review B*, 73(3):035310, Jan. 2006. doi:[10.1103/PhysRevB.73.035310](https://doi.org/10.1103/PhysRevB.73.035310).

- [79] S. Wang, Y. Song, and I. S. Roy. Bismuth incorporation and lattice contraction in GaSbBi and InSbBi. *Transparent Optical Networks (ICTON), 2011 13th International Conference on*, pages 1–3, 2011. doi:[10.1109/ICTON.2011.5970830](https://doi.org/10.1109/ICTON.2011.5970830).
- [80] C. Liu, Y. Lee, T. Kondo, E. D. Mun, M. Caudle, B. N. Harmon, S. L. Bud'Ko, P. C. Canfield, and A. Kaminski. Metallic surface electronic state in half-Heusler compounds RPtBi (R= Lu, Dy, Gd). *Physical Review B*, 83(20):205133, May 2011. doi:[10.1103/PhysRevB.83.205133](https://doi.org/10.1103/PhysRevB.83.205133).
- [81] B. Balke, G. Fecher, and H. Kandpal. Properties of the quaternary half-metal-type Heusler alloy $\text{Co}_2\text{Mn}_{1-x}\text{Fe}_x\text{Si}$. *Physical Review B*, 74(10):104405, 2006. doi:[10.1103/PhysRevB.74.104405](https://doi.org/10.1103/PhysRevB.74.104405).
- [82] S. Picozzi, A. Continenza, and A. Freeman. Co_2MnX (X=Si, Ge, Sn) Heusler compounds: An ab initio study of their structural, electronic, and magnetic properties at zero and elevated pressure. *Physical Review B*, 66(9):094421, Sept. 2002. doi:[10.1103/PhysRevB.66.094421](https://doi.org/10.1103/PhysRevB.66.094421).
- [83] S. Wurmehl, G. H. Fecher, H. C. Kandpal, V. Ksenofontov, C. Felser, H.-J. Lin, and J. Morais. Geometric, electronic, and magnetic structure of Co_2FeSi : Curie temperature and magnetic moment measurements and calculations. *Physical Review B*, 72(18):184434, 2005. doi:[10.1103/PhysRevB.72.184434](https://doi.org/10.1103/PhysRevB.72.184434).

- [84] K. Lüdge, B. D. Schultz, P. Vogt, M. M. R. Evans, W. Braun, C. J. Palmstrøm, W. Richter, and N. Esser. Structure and interface composition of Co layers grown on As-rich GaAs(001) c(44) surfaces. *Journal of Vacuum Science and Technology B*, 20(4):1591, 2002. doi:[10.1116/1.1491993](https://doi.org/10.1116/1.1491993).
- [85] C. J. Palmstrøm. Epitaxial Heusler Alloys: New Materials for Semiconductor Spintronics. *MRS Bulletin*, 28(10):725–728, 2003. doi:[10.1557/mrs2003.213](https://doi.org/10.1557/mrs2003.213).
- [86] J. L. Hilton, B. D. Schultz, S. McKernan, and C. J. Palmstrøm. Interfacial reactions of Mn/GaAs thin films. *Applied Physics Letters*, 84(2004):3145–3147, 2004. doi:[10.1063/1.1703831](https://doi.org/10.1063/1.1703831).
- [87] J. L. Hilton, B. D. Schultz, and C. J. Palmstrøm. Growth temperature dependence of Mn/GaAs surfaces and interfaces. *Journal of Applied Physics*, 102(2007):063513, 2007. doi:[10.1063/1.2783768](https://doi.org/10.1063/1.2783768).
- [88] B. D. Schultz, C. Adelman, X. Y. Dong, S. McKernan, and C. J. Palmstrøm. Phase formation in the thin film Fe/GaAs system. *Applied Physics Letters*, 92(2008):53–56, 2008. doi:[10.1063/1.2888748](https://doi.org/10.1063/1.2888748).
- [89] L. C. Chen, J. W. Dong, B. D. Schultz, C. J. Palmstrøm, J. Berzovsky, A. Isakovic, P. A. Crowell, and N. Tabat. Epitaxial ferromagnetic metal/GaAs(100) heterostructures. *Journal of Vacuum Science & Technology B*, 18(4):2057, 2000. doi:[10.1116/1.1306297](https://doi.org/10.1116/1.1306297).

- [90] H. C. Kandpal, G. H. Fecher, C. Felser, and G. Schönhense. Correlation in the transition-metal-based Heusler compounds Co_2MnSi and Co_2FeSi . *Physical Review B*, 73(9):1–11, 2006. doi:[10.1103/PhysRevB.73.094422](https://doi.org/10.1103/PhysRevB.73.094422).
- [91] I. Galanakis, P. H. Dederichs, and N. Papanikolaou. Slater-Pauling Behavior of the Half-Ferromagnetic Full-Heusler Alloys. *Physical Review B*, 66(17):10, Nov. 2002. doi:[10.1103/PhysRevB.66.174429](https://doi.org/10.1103/PhysRevB.66.174429).
- [92] F. J. Yang, Y. Sakuraba, S. Kokado, Y. Kota, A. Sakuma, and K. Takanashi. Anisotropic magnetoresistance in $\text{Co}_2(\text{Fe},\text{Mn})\text{Si}$ Heusler epitaxial films: A fingerprint of half-metallicity. *Physical Review B*, 86(2):2–5, 2012. doi:[10.1103/PhysRevB.86.020409](https://doi.org/10.1103/PhysRevB.86.020409).
- [93] J. P. Wüstenberg, R. Fetzner, M. Aeschlimann, M. Cinchetti, J. Minár, J. Braun, H. Ebert, T. Ishikawa, T. Uemura, and M. Yamamoto. Surface spin polarization of the nonstoichiometric Heusler alloy Co_2MnSi . *Physical Review B*, 85:1–10, 2012. doi:[10.1103/PhysRevB.85.064407](https://doi.org/10.1103/PhysRevB.85.064407).
- [94] B. Hülsen, M. Scheffler, and P. Kratzer. Thermodynamics of the Heusler alloy $\text{Co}_{2-x}\text{Mn}_{1+x}\text{Si}$: A combined density functional theory and cluster expansion study. *Physical Review B*, 79(9):094407, Mar. 2009. doi:[10.1103/PhysRevB.79.094407](https://doi.org/10.1103/PhysRevB.79.094407).
- [95] K. Nagao, Y. Miura, and M. Shirai. Half-metallicity at the (110) interface

- between a full Heusler alloy and GaAs. *Physical Review B*, 73(10):1–7, 2006. doi:[10.1103/PhysRevB.73.104447](https://doi.org/10.1103/PhysRevB.73.104447).
- [96] S. Hashemifar, P. Kratzer, and M. Scheffler. Preserving the Half-Metallicity at the Heusler Alloy $\text{Co}_2\text{MnSi}(001)$ Surface: A Density Functional Theory Study. *Physical Review Letters*, 94(9):1–4, 2005. doi:[10.1103/PhysRevLett.94.096402](https://doi.org/10.1103/PhysRevLett.94.096402).
- [97] A. Avery, J. Sudijono, T. Jones, and B. Joyce. The location of silicon atoms and the initial stages of formation of the interface studied by STM. *Surface Science*, 340:57–70, 1995. doi:[10.1016/0039-6028\(95\)00685-0](https://doi.org/10.1016/0039-6028(95)00685-0).
- [98] B. D. Schultz. *In – situ* surface, chemical, and electrical characterization of the interfaces between ferromagnetic metals and compound semiconductors grown by molecular beam epitaxy. *Dissertation*, 2004.
- [99] Q. O. Hu, E. S. Garlid, P. A. Crowell, and C. J. Palmstrøm. Spin accumulation near Fe/GaAs (001) interfaces: The role of semiconductor band structure. *Physical Review B*, 84(8):085306, Aug. 2011. doi:[10.1103/PhysRevB.84.085306](https://doi.org/10.1103/PhysRevB.84.085306).
- [100] C. Crowell and S. Sze. Current transport in metal-semiconductor barriers. *Solid-State Electronics*, 9(11-12):1035–1048, Nov. 1966. doi:[10.1016/0038-1101\(66\)90127-4](https://doi.org/10.1016/0038-1101(66)90127-4).
- [101] H. C. Kandpal, V. Ksenofontov, B. Balke, M. Wojcik, R. Seshadri,

- and C. Felser. Electronic structure, magnetism, and disorder in the Heusler compound Co_2TiSn . *Journal of Physics D*, 40:1587–1592, 2007. doi:[10.1088/0022-3727/40/6/S13](https://doi.org/10.1088/0022-3727/40/6/S13).
- [102] H. C. Kandpal, G. H. Fecher, and C. Felser. Calculated electronic and magnetic properties of the half-metallic, transition metal based Heusler compounds. *Journal of Physics D*, (40):1507–1523, 2007. doi:[10.1088/0022-3727/40/6/S01](https://doi.org/10.1088/0022-3727/40/6/S01).
- [103] M. Julliere. Tunneling between ferromagnetic films. *Physics Letters A*, 54(3):225–226, 1975. doi:[10.1016/0375-9601\(75\)90174-7](https://doi.org/10.1016/0375-9601(75)90174-7).
- [104] W. Butler, X. G. Zhang, T. Schulthess, and J. MacLaren. Spin-dependent tunneling conductance of Fe—MgO—Fe sandwiches. *Physical Review B*, 63(5):1–12, 2001. doi:[10.1103/PhysRevB.63.054416](https://doi.org/10.1103/PhysRevB.63.054416).
- [105] R. Meservey and P. Tedrow. Spin-polarized electron tunneling. *Physics Reports*, 238(4):173–243, Mar. 1994. doi:[10.1016/0370-1573\(94\)90105-8](https://doi.org/10.1016/0370-1573(94)90105-8).
- [106] G. Strijkers, Y. Ji, F. Yang, C. Chien, and J. Byers. Andreev reflections at metal/superconductor point contacts: Measurement and analysis. *Physical Review B*, 63(10):104510, Feb. 2001. doi:[10.1103/PhysRevB.63.104510](https://doi.org/10.1103/PhysRevB.63.104510).
- [107] G. Woods, R. Soulen, I. Mazin, B. Nadgorny, M. Osofsky, J. Sanders, H. Srikanth, W. Egelhoff, and R. Datla. Analysis of point-contact Andreev

- reflection spectra in spin polarization measurements. *Physical Review B*, 70(5):054416, Aug. 2004. doi:[10.1103/PhysRevB.70.054416](https://doi.org/10.1103/PhysRevB.70.054416).
- [108] Y. F. Hsu, T. W. Chiang, G. Y. Guo, S. F. Lee, and J. J. Liang. Effect of transport-induced charge inhomogeneity on point-contact andreev reflection spectra at ferromagnet-superconductor interfaces. *Journal of the Physical Society of Japan*, 81(8):1–8, 2012. doi:[10.1143/JPSJ.81.084704](https://doi.org/10.1143/JPSJ.81.084704).
- [109] S. Bouvron, M. Stokmaier, M. Marz, and G. Goll. Andreev experiments on superconductor/ferromagnet point contacts. *Low Temperature Physics*, 39(3):274, 2013. doi:[10.1063/1.4795198](https://doi.org/10.1063/1.4795198).
- [110] W. K. Park and L. H. Greene. Construction of a Cantilever-Andreev-Tunneling rig and its applications to superconductors. *Review of Scientific Instruments*, 77(2):1–6, 2006. doi:[10.1063/1.2168670](https://doi.org/10.1063/1.2168670).
- [111] PCAR Schematic. URL <http://www.physics.wayne.edu/~simonadgorny/techn1.html>.
- [112] Y. Uehara, T. Fujita, M. Iwami, and S. Ushioda. Superconducting niobium tip for scanning tunneling microscope light emission spectroscopy. *Review of Scientific Instruments*, 72(4):2097–2099, 2001. doi:[10.1063/1.1350644](https://doi.org/10.1063/1.1350644).